Investigation of Image Potential States with the Green Function Embedding Technique

von

Alexander Hanuschkin

Diplomarbeit in Physik

vorgelegt der

Fakultät für Mathematik, Informatik und Naturwissenschaften
der Rheinisch-Westfälischen Technischen Hochschule Aachen

im
Juli 2007

angefertigt am

Institut für Festkörperforschung (IFF)
Forschungszentrum Jülich

Abstract

Recently image potential states were investigated using spin-polarized scanning tunneling microscopy (STM) [62]. A potential well between metal surfaces with a band gap at the vacuum energy and the image potential creates hydrogen-like states above the surface. Additionally these states exhibit a small spin splitting if the surface is ferromagnetic. DFT calculations with the Green function embedding technique allow to treat surfaces with a semi-infinite substrate. To capture the image potential states the DFT potential has to be modified to include the correct $1/z$ like asymptotic behavior towards the vacuum. In our scheme this is efficiently done by calculating and adding the corresponding embedding potential for the vacuum. Furthermore a bias can be applied to the surface giving rise to field induced states commonly observed by STM.
This work presents details of the computational scheme as well as results for image potential states of transition-metal surfaces with and without applied electric field.

Contents

1 Introduction

The study of surfaces and thin films is a large and interesting topic within the field of solid state physics. The physical properties of surfaces and thin films are changing enormous compared to the bulk properties because of the broken symmetry. This on the one hand gives rise to new applications such as more sensitive hard disc heads employing the GMR effect or magneto optical data storage devices using thin film sandwiches with designed magnetic properties and on the other hand to completely new technologies like spintronics. While modern techniques like molecular beam epitaxy (MBE) and sputtering allow to perform layer by layer growth of surfaces, experimental methods of surfaces observation like photoemission and diffraction of electrons (low energy electron diffraction (LEED), reflection high-energy electron diffraction (REED)) can resolve the electronic structure of the system (even in situ). But still the theoretical description of the electronic structure is a difficult task.

Beside the ordinary surface states image potential induced states have been discussed deeply in the 1980th. They recently attracted renewed interest due to new experimental approaches like spin-resolved scanning tunneling microscopy (STM) measurements [62]. As known from basic electrodynamics, a charge distribution in front of a metallic surface will induce a screening charge. This gives rise to a $1/z$ like image potential in the vacuum region. The potential well between metal surfaces with a band gap at the vacuum energy and the image potential creates hydrogen-like states above the surface. Additionally, these states exhibit a small spin splitting if the surface is ferromagnetic and can be investigated using spin-polarized STM. In this work these image potential induced states will be investigated by a computational quantum mechanical approach.

Nowadays, computational physics is becoming a third way of approaching physical phenomena beside theory and experiment. Simulations are able to scope with a large variety of lengthscales, starting from *ab initio* calculations of matter to simulations of planet movements. While new theoretical approaches and new algorithms were developed which enables the computation of more complex systems also the computational power increases exponentially. One of the most interesting example for the former was the development of the density functional theory (DFT) by Kohn [59] which allows us to treat many-body electron systems in a single particle picture and which is in principle still an exact theory. The increase in computational power can be predicted by Moore's law [69], which states that the complexity of systems available for minimal cost will double each year. Even though it is more likely a self-fulfilling prophecy than a law of nature the statement suites well for the last centuries.

In the following the electronic structure of transition metal surfaces will be calculated by an ab-initio program, based on DFT. In order to treat the surface region in a semi-infinite way the Green function embedding technique introduced by Inglesfield [50] will be used. The Green function embedding method allows to tread a perturbed region like a surface or a finite region between two infinite leads by concentrating on this

embedded perturbated region alone. Embedding potentials from the bulk system and the analytically derived embedding potential from the vacuum region are employed for the boundaries of the perturbed system. In order to model the image potential states the embedding potential of the vacuum region has to be calculated numerically with a $1/z$ like potential which cannot be obtained from pure DFT calculation. Additionally a constant electric field will be applied to the system. In this way a STM tip can be modeled and changes of the Image Potential states can be studied.

In chapter 2 the necessary theory will be introduced. The Green function embedding technique employs the DFT (section 2.1) and uses the FLAPW (section 2.2) basis set. Therefore this two subjects will be covered at the start. Then the Green function embedding technique by Inglesfield [50] will be introduced in section 2.4 after summarizing the main properties of Green functions in general (section 2.3). The concept of the complex bandstructure is needed for the computational implementation [117] of the embedding technique and will therefore be explained in section 2.5. The following section 2.6 shows how the computational implementation is done. The chapter ends with a summary of the computational approach (section 2.7).

In the second part of this thesis (chapter 3) the localized states at surfaces will be addressed. In special states introduced by the image potential in front of metallic surfaces. They are called image potential states. They will be explained in section 3.2. The experimental setups measuring these states are given in section 3.2.1 and it will be shown how these states can be calculated within the Green function embedding approach (section 3.2.2). At the end the influence of a constant electrical field is investigated in section 3.3. The image potential states become field states. In section 3.3.1 it will be shown how an electric field will be included in our computational method.

The last chapter 4 of the thesis is summarizing our results of the surface state of Ag(111) (section 4.1) and the image potential states of Ag(100) and Fe(110). We calculate the image plane by evaluating the center of screening charge in section 4.2 and the image state energies of the silver and iron in 4.3.1 and 4.3.2 respectively. In the last part the image potential induced field states are investigated. In section 4.4.1 this is done for the Ag(100) surface. The field states of the magnetic Fe(110) will be shown in 4.4.2.

2 Theory

2.1 Density Functional Theory

It is said that shortly after Schrödinger's equation for the electronic wavefunction had been spectacularly validated for small systems like He and H_2, "Dirac declared that chemistry had come to an end - its content was entirely contained in that powerful equation. Too bad, he is said to have added, that in almost all cases, this equation was far too complex to allow solutions." [59] And still it is. Even with the most advanced computers an exact solution of even tiny systems will not be possible. All the physics is condensed in the many-body wavefunction of the system under consideration. If for purposes of studying electron dynamics the Born-Oppenheimer approximation is used, considering the much heavier nuclei as fixed in space the Schrödinger equation can be written as:

$$\left(-\frac{\hbar^2}{2m}\sum_j \nabla_j^2 - \sum_{j,l}\frac{Z_l e^2}{|\mathbf{r}_j - \mathbf{R}_l|} + \frac{1}{2}\sum_{j\neq j'}\frac{e^2}{|\mathbf{r}_j - \mathbf{r}_{j'}|} + V_{\text{ext}}\right)\Psi(\mathbf{r}_1, \mathbf{r}_2, ..) \quad = \quad E\Psi(\mathbf{r}_1, \mathbf{r}_2, ..) \tag{2.1}$$

Upper case letters giving the positions $\mathbf{R}_l$ and atomic numbers Z_l of the nuclei and lower case letters are used for the positions $\mathbf{r}_j$ of the electrons. The energy is denoted by E and the many-electron wavefunction depending on the position and spins of the N electrons is represented by Ψ. Now it becomes obvious that without further appropriate approximations we cannot handle the equation. Consider only the electronic wavefunction of an iron atom which depends on 26 (N_e) times 3 (space) coordinates. Storing the wavefunction on a coarse grid with only 10 points per variable would yield 10^{78} numbers to store and process [27]. Thus we can see that with many-electrons we are encountering an exponential wall. It should be noted that all the physical properties of the electrons, especially the density $n(\mathbf{r})$ and the total energy E, depend on the position of the nuclei. This two quantities play key roles in the Density Functional Theory (DFT).

The trick of the DFT is to work with the electron density instead of using the many-electron wavefunction itself. By minimizing a functional of the electron density the many-body problem can be tackled in a single body way. The mapping is exact in principle but the density functional is not known. At this point approximations have to be made. The commonly used approximations are the Local Density Approximation (LDA) and the Generalized Gradient Approximation (GGA), explained in section 2.1.3. Even simple approaches like LDA result in accurate results for a number of systems.

At the moment DFT calculations are used in an uncounted number of applications to physical or chemical systems, reaching from fundamental research to applications in industry. If standard[1] DFT is not suitable new methods based on DFT grew. If DFT

[1] nondegenerate, nonmagnetic

fails it provides clues for new theoretical approaches.
DFT can easily be extended to include (non-)collinear spins in order to calculate magnetic systems. Also it can be generalized to treat degenerated groundstates or a bunch of degenerated ground states (ensemble DFT), to relativistic electrons, to bosonic instead of fermionic systems or to investigate superconductors with electronic pairing mechanisms. The theory of DFT can be extended also to include the movement of the nuclei. Well known is the theory of Car and Parrinello [22] combining DFT with molecular dynamics in one step. If an extension to the treatment of impurity problems or transport is needed the embedded Green function approach can be applied based on DFT calculations (see section 2.4). Multicomponent systems can be investigated and if time dependency is the property of interest time dependent DFT [20] is available. For a more detailed picture of the different DFT branches have a look at [56]. DFT fails for systems where the electron-electron interaction is the dominating effect. At this point new methods like GW can be applied or new theoretical techniques like exact exchange have to be taken into consideration.

It is worth to be mentioned that "for his development of the density-functional theory" Walter Kohn was awarded the Nobel Prize in chemistry in 1998 together with John A. Pople for the "development of computational methods in quantum chemistry" [86].

2.1.1 Hohenberg-Kohn Theorem

Two statements are at the foundation of the Density Functional Theory (DFT) and were published in 1964 by Hohenberg and Kohn [47]. For a system of N particles moving in an external potential $V_{\text{ext}}(\mathbf{r})$:

1. Theorem:

$$n_0(\mathbf{r}) \quad \Rightarrow \quad V_{\text{ext}}(\mathbf{r}), \Psi_0(\mathbf{r}_1, \mathbf{r}_2, ..) \tag{2.2}$$

   The electron density distribution $n(\mathbf{r})$ determines uniquely the external potential $V_{\text{ext}}(\mathbf{r})$ and thus the many-body wavefunction $\Psi(\mathbf{r}_1, \mathbf{r}_2, ..)$. All ground-state properties and in particular the ground state wavefunction $\Psi_0(\mathbf{r}_1, \mathbf{r}_2, ..)$ are functionals of the ground-state density $n_0(\mathbf{r})$.

2. Theorem:

$$E_0 \quad = \quad \min_n E[n(\mathbf{r})] \tag{2.3}$$

   There exists an energy functional of the density, $E[n(\mathbf{r})]$, which is stationary with respect to the variation of the ground state density. This minimization principle can be used to determine the ground state density E_0.

In order to proof the first theorem we will restrict ourself to non-degenerated ground states. The theorem can be extended to degenerated ground states but the proof will be left to Kohn [58]. Let us assume two ground state wavefunctions $\Psi_0 \neq \Psi_0'$ with different external potential $V_{\text{ext}} \neq V_{\text{ext}}'$ leading to the same ground state density n_0. We know that

$E_0 = \langle\Psi_0|H_V|\Psi_0\rangle$ and $E_0' = \langle\Psi_0'|H_{V'}|\Psi_0'\rangle$, whereby $H_V = T+U+V_{\text{ext}}$ is the Hamiltonian with kinetic energy T, interaction energy U (including classical electrostatic interaction and correlation effects) and external potential V_{ext}. We get

$$E_0 < \langle\Psi_0'|H_V|\Psi_0'\rangle = \langle\Psi_0'|H_{V'} + V_{\text{ext}} - V_{\text{ext}}'|\Psi_0'\rangle = E_0' + \int n_0(\mathbf{r})[V_{\text{ext}} - V_{\text{ext}}']d\mathbf{r}. \quad (2.4)$$

The strict less is due to the non-degenerated ground state.
Analogous we get $E_0' < E_0 + \int n_0(\mathbf{r})[V_{\text{ext}}' - V_{\text{ext}}]d\mathbf{r}$. The combination of both equations results in a contradiction.

$$E_0 + E_0' \quad < \quad E_0 + E_0' \quad \text{Contradiction!} \quad (2.5)$$

The ground state density cannot be the same. Two different potentials will not give the same ground state density and therefore the ground state density determines the external potential uniquely. It follows as a corollary that since $n(\mathbf{r})$ determines $V_{\text{ext}}(\mathbf{r})$, it also determines the wavefunction Ψ. Thus all ground-state properties are functionals of the ground-state density $n_0(\mathbf{r})$.

A simpler derivation of the second theorem than in the original paper was given by Levy [65]. The unique energy functional $E[n(\mathbf{r})]$ can be defined as the minimum over all wavefunction, which deliver the density $n(\mathbf{r})$.

$$E[n(\mathbf{r})] = \min_{\Psi\to n} \langle\Psi|T + U + V_{\text{ext}}|\Psi\rangle \quad (2.6)$$

$$= F[n(\mathbf{r})] + \int n(\mathbf{r})V_{\text{ext}}(\mathbf{r})d\mathbf{r} \quad (2.7)$$

The simple functional dependence of $E[n(\mathbf{r})]$ on V_{ext} can be observed in the equation. The universal functional $F[n(\mathbf{r})] = \min_{\Psi\to n}\langle\Psi|T+U|\Psi\rangle$ is the same for all systems described by the same Schrödinger equation. The interaction term U includes the electron-electron and the electron-nuclei interaction. Thus the term introduces the many-body effects.

$$U = -\sum_{i,l}\frac{Z_l e^2}{|\mathbf{r}_j - \mathbf{R}_l|} + \frac{1}{2}\sum_{i=1}^{N}\sum_{j\neq i}^{N}\frac{e^2}{|\mathbf{r}_j - \mathbf{r}_i|} \quad (2.8)$$

From (2.6) follows directly

$$E[n(\mathbf{r})] = \left\langle\Psi_n^{\min}|T + U + V_{\text{ext}}|\Psi_n^{\min}\right\rangle \geq E_0, \quad (2.9)$$

because of the Rayleigh-Ritz principle $E_0 = \langle\Psi_0|H|\Psi_0\rangle$. On the other hand if we insert the ground-state wavefunction Ψ_0 into (2.6) we get

$$E[n_0(\mathbf{r})] \leq \langle\Psi_0|T + U + V_{\text{ext}}|\Psi_0\rangle = E_0. \quad (2.10)$$

We used that the ground-state energy is given by the ground state wavefunction. The inequality follows from (2.6) because the energy functional is defined as the minimum over all wavefunction which give the ground state energy. One of this wavefunction is Ψ_0. Since (2.9) is valid for any density we get $E[n_0(\mathbf{r})] \geq E_0$. Together with (2.9) follows $E_0 = E[n_0(\mathbf{r})]$. Thus

$$E_0 = \min_n E[n(\mathbf{r})]. \quad (2.11)$$

This variational principle can be used to determine the ground-state density and the ground state energy, if the functional $F[n(\mathbf{r})]$ is known.

2.1.2 Kohn-Sham Equation

The theorems of Hohenberg and Kohn transformed the problem of finding the solution of $\langle\Psi|H|\Psi\rangle$ with the 3N-dimensional trial function Ψ to the problem of minimizing $E[n(\mathbf{r})]$ with respect to the 3-dimensional function $n(\mathbf{r})$. This seems to be a huge step forward but the functional $F[n(\mathbf{r})]$ is unknown. In 1965 Kohn and Sham [60] proposed to approach the kinetic energy of the interacting electrons with that of an equivalent non interacting system. The crucial point is that the kinetic energy of a non interacting system can easily be calculated. The density of the interacting ground state is the sum of the spin-up and spin-down density, but let us concentrate on the case without spin for simplicity. The inclusion of spin can easily be done [56]. The density can be given by

$$n(\mathbf{r},\mathbf{r}') = \sum_{i=1}^{\infty} N_i \psi_i^*(\mathbf{r})\psi_i(\mathbf{r}'), \tag{2.12}$$

where N_i denotes the occupation number of the orbitals ψ_i. Also the kinetic energy can be formulated in the usual way.

$$T = \sum_{i=1}^{\infty} N_i \langle\psi_i| -\frac{\hbar^2}{2m}\nabla^2|\psi_i\rangle \tag{2.13}$$

Now a non-interacting reference system with the same ground state density $n(\mathbf{r})$ and energy than the interacting one will be assumed. The potential[2] V_{R} of the reference system in the Hamiltonian is chosen such that the equivalence of the mentioned quantities is reached.

$$H_{\mathrm{R}} = \sum_{i=1}^{N}\left(-\frac{\hbar^2}{2m}\nabla^2 + V_{\mathrm{R}}(\mathbf{r_i})\right) \tag{2.14}$$

Since there is no electron-electron interaction the eigenstates of the Hamiltonian can be expressed in the form of Slater determinants and the density and the kinetic energy can be written as

$$n(\mathbf{r}) = \sum_{i=1}^{N} |\psi_i(\mathbf{r})|^2, \tag{2.15}$$

$$T_{\mathrm{R}}[n] = \sum_{i=1}^{N} \langle\psi_i| -\frac{\hbar^2}{2m}\nabla^2|\psi_i\rangle. \tag{2.16}$$

The single-particle wavefunctions ψ_i are the N lowest eigenstates of the reference Hamiltonian

$$\left(-\frac{\hbar^2}{2m}\nabla^2 + V_{\mathrm{R}}(\mathbf{r})\right)\psi_i(\mathbf{r}) = \epsilon_i\psi_i(\mathbf{r}). \tag{2.17}$$

[2]sometimes named effective potential V_{eff} instead of potential of the reference system V_{R}

Still the potential of the reference system is unknown but will be derived later. The universal density functional F can be written as

$$F[n] = T_{\mathrm{R}}[n] + \frac{1}{2}\iint \frac{n(\mathbf{r})n(\mathbf{r}')}{|\mathbf{r}-\mathbf{r}'|}d\mathbf{r}d\mathbf{r}' + E_{\mathrm{xc}}[n]. \tag{2.18}$$

The expression for F can be substitute into the total energy functional (2.6) resulting in the Kohn-Sham (KS) functional:

$$E_{\mathrm{KS}}[n(\mathbf{r})] = T_{\mathrm{R}}[n(\mathbf{r})] + \int n(\mathbf{r})V_{\mathrm{ext}}(\mathbf{r})d\mathbf{r} + \frac{1}{2}\iint \frac{n(\mathbf{r})n(\mathbf{r}')}{|\mathbf{r}-\mathbf{r}'|}d\mathbf{r}d\mathbf{r}' + E_{\mathrm{xc}}[n] \tag{2.19}$$

The density functional is expressed in terms of N (KS) orbitals ψ_i, minimizing the kinetic energy under the fixed density constrain and satisfying equation (2.17). But let us come back to the problem of determining the reference potential V_{R}, which is used to calculate the KS wavefunctions. This can be done by minimizing the KS functional (2.19) over all densities that integrate to N particles.

$$\mu_{\mathrm{R}} = \frac{\delta T_{\mathrm{R}}[n(\mathbf{r})]}{\delta n} + V_{\mathrm{ext}} + \int \frac{n(\mathbf{r}')}{|\mathbf{r}-\mathbf{r}'|}d\mathbf{r}' + \frac{\delta E_{\mathrm{xc}}[n(\mathbf{r})]}{\delta n} \tag{2.20}$$

Here the functional derivative from the non-interacting kinetic energy is given by

$$\frac{\delta T_{\mathrm{R}}[n(\mathbf{r})]}{\delta n} + V_{\mathrm{R}}(\mathbf{r}) = \mu_{\mathrm{R}}, \tag{2.21}$$

because $E_{\mathrm{R}}[n] = T_{\mathrm{R}} + \int nV_{\mathrm{R}}d\mathbf{r} = E_0$. The chemical potential for the non interacting system is given by μ_{R}. With (2.17) this leads directly to the famous self-consistent Kohn-Sham equations:

$$\left[-\frac{\hbar^2}{2m}\nabla^2 + V_{\mathrm{ext}}(\mathbf{r}) + \int \frac{n(\mathbf{r}')}{|\mathbf{r}-\mathbf{r}'|}d\mathbf{r}' + \frac{\delta E_{\mathrm{xc}}}{\delta n(\mathbf{r})}\right]\psi_i(\mathbf{r}) = \epsilon_i\psi_i(\mathbf{r}) \tag{2.22}$$

$$\text{with} \quad n(\mathbf{r}) = \sum_{i=1}^{N} |\psi_i(\mathbf{r})|^2 \tag{2.23}$$

The functional derivative of the exchange-correlation energy $\frac{\delta E_{\mathrm{xc}}}{\delta n(\mathbf{r})}$ is called exchange-correlation potential. The exchange-correlation potential includes all correlation effects and has to be approximated. It should be noted that an exact expression can be written down as described in [16].

$$E_{\mathrm{xc}}[n] = \frac{e^2}{2}\int n(\mathbf{r})d\mathbf{r}\int \frac{n_{\mathrm{xc}}(\mathbf{r},\mathbf{r}-\mathbf{r}')}{|\mathbf{r}'-\mathbf{r}|}d\mathbf{r}' \tag{2.24}$$

Thereby the 'exchange correlation hole'

$$n_{\mathrm{xc}}(\mathbf{r},\mathbf{r}-\mathbf{r}') = n(\mathbf{r}')\int_0^1 (g(\mathbf{r},\mathbf{r}',\lambda)-1)d\lambda \tag{2.25}$$

is introduced. Thus $E_{\mathrm{xc}}[n]$ can be viewed as the Coulomb interaction of the density $n[\mathbf{r}]$ with the corresponding holes. The pair-correlation function $g(\mathbf{r},\mathbf{r}',\lambda)$ couples the density with the interaction. The integral connects the electron correlation of the interacting to the correlations in the non-interacting system.

2.1.3 Approximation of $E_{\mathrm{xc}}[n(\mathbf{r})]$

The exchange-correlation energy can be written as

$$E_{\mathrm{xc}}[n(\mathbf{r})] = \int e_{\mathrm{xc}}(\mathbf{r}, [n(\mathbf{r}')])n(\mathbf{r})d\mathbf{r}' \tag{2.26}$$

in a quasi local form. $e_{\mathrm{xc}}(\mathbf{r}, [n(\mathbf{r}')])$ gives the exchange-correlation energy per particle at point $\mathbf{r}$. It is functional depending on the density at point $\mathbf{r}'$. The energy primarily depends on the density at points $\mathbf{r}'$ near $\mathbf{r}$, such that $|\mathbf{r} - \mathbf{r}'| \approx \lambda_{\mathrm{F}}$. Hence Kohn called $e_{\mathrm{xc}}(\mathbf{r}, [n(\mathbf{r}')])$ a nearsighted functional of $n(\mathbf{r}')$ [59]. The simplest and most widely used approximation is the **Local Density Approximation (LDA)**.

$$E_{\mathrm{xc}}^{\mathrm{LDA}}[n(\mathbf{r})] = \int e_{\mathrm{xc}}(n(\mathbf{r}))n(\mathbf{r})d\mathbf{r} \tag{2.27}$$

The remarkable point is that in LDA the exchange-correlation energy per particle is a function of the density $n(\mathbf{r})$. In case of an uniform electron gas of density n LDA is exact, the exchange part is elementary and the correlation part can be given with high precision using Monte Carlo methods. It was expected that LDA fails for densities varying fast on the scale of the Fermi wavelength λ_{F}. But nevertheless it is observed that LDA provides useful results for most applications. For example ionization energies of atoms, dissociation energies of molecules and of course for materials with quite uniform electronic density such as bulk metals. In practice $e_{\mathrm{xc}}(n(\mathbf{r}))$ is given by using an explicit parameterization. These parameterizations are obtained by fitting to quantum-mechanical many-body calculations. The parametrization mainly used in this work is the one by Barth and Hedin (BH) [9]. The accuracy of the exchange energy is of the order of 10%, while the usually smaller correlation energy is most of the times overestimated up to a factor of two. Both errors cancel partially in most cases [59]. Beyond LDA the so called **Generalized Gradient Approximation (GGA)** is extensively used. A derivation can be found e.g. at [56]. It introduces the dependence on the gradient of the density into the exchange-correlation energy.

$$E_{\mathrm{xc}}^{\mathrm{GGA}}[n(\mathbf{r})] = \int e_{\mathrm{xc}}\left(n(\mathbf{r})\right) n(\mathbf{r})d\mathbf{r} + \int F_{\mathrm{xc}}\left(n(\mathbf{r}), |\nabla n(\mathbf{r})|\right) n(\mathbf{r})d\mathbf{r} \tag{2.28}$$

The parametrization for F_{xc} mainly used in this work is the one developed by Perdew-Burke-Ernzerhof (PBE) [80]. LDA (or if spin dependent LSDA) and GGA fail to describe systems which are dominated by electron-electron interaction effects.

2.1.4 DFT in a Nutshell

Instead of solving the exact Schrödinger equation of the many-particle problem an energy functional with respect to the charge density can be minimized. The Hohenberg-Kohn theorems state that such a functional exists, its minimum determines the ground state energy and the corresponding density gives all the ground state properties. Still the energy functional is unknown and hence the theorems are of little use. This problem can be tackled by looking at a non interacting (reference) system in an effective potential V_{R} with the same ground state density and energy than the interacting system under

consideration. The eigenstates of the reference system can easily by found if the effective potential is known. Kohn and Sham derived the well known self-consistent equation

$$\left[-\frac{\hbar^2}{2m}\nabla^2 + V_{\text{ext}}(\mathbf{r}) + \int \frac{n(\mathbf{r}')}{|\mathbf{r}-\mathbf{r}'|}d\mathbf{r}' + V_{\text{xc}}[n]\right]\psi_i(\mathbf{r}) \quad = \quad \epsilon_i\psi_i(\mathbf{r}) \tag{2.29}$$

where the effective potential can be replaced by the external potential, the Coulomb interaction and an exchange-correlation potential. All the correlation effects are hidden in the exchange-correlation potential, which is the functional derivative of the exchange energy with respect to the density.

$$V_{\text{xc}}(\mathbf{r}) \quad = \quad \frac{\delta E_{\text{xc}}}{\delta n(\mathbf{r})} \tag{2.30}$$

In practice the exchange correlation potential is approximated (e.g. by LDA or GGA). From the eigenstates of the Kohn-Sham equation a new density is obtained that can be used to recalculate the eigenstates. In this way the Kohn-Sham equation have to be solved until self-consistency is reached.

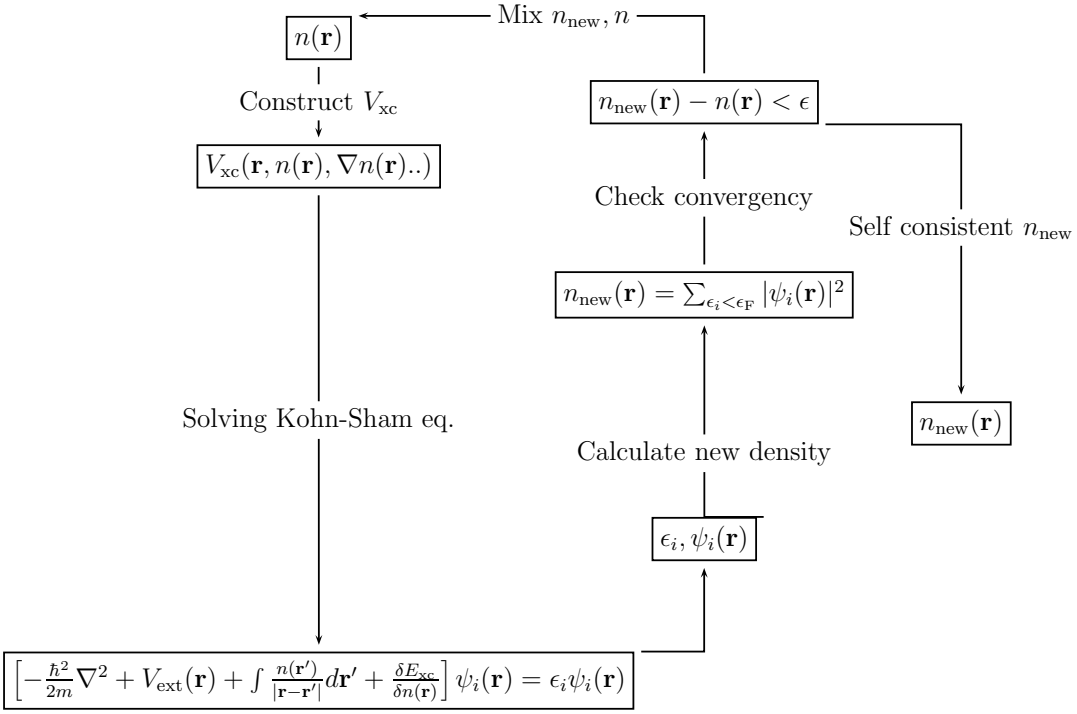

Figure 2.1: Cycle used to solve the Kohn-Sham equation self-consistently.

2.2 FLAPW

There are many ways how the DFT can be used in a real numerical code to calculate the electron densities and the eigenenergies of many-body systems. The different methods can be separated by the representation of the KS orbitals they apply. They all have to solve the KS equation (2.23) in a self-consistency loop in order to determine the KS orbitals $\psi_i(\mathbf{r})$ and hence the density $n(\mathbf{r})$. The first intuitive approach might be to solve the differential equation numerically on a grid. But that is not the way most methods for solids tackle the equation, because in general planewaves are the tool of choice to describe the physics of bulk materials. They can be introduced by an appropriate basis set of functions $\phi_\beta(\mathbf{r})$ transforming the differential equation into a matrix eigenvalue problem. The KS orbitals can be expressed in the basis set by

$$\psi_i(\mathbf{r}) = \sum_\beta c_{i,\beta}\phi_\beta(\mathbf{r}) \tag{2.31}$$

with expansion coefficients $c_{i,\beta}$ and therefore the KS equation can be written as:

$$(H_{\mathrm{KS}}(\mathbf{r}) - \epsilon_i)\sum_\beta c_{i,\beta}\phi_\beta(\mathbf{r}) = 0 \tag{2.32}$$

The matrix equation is not yet complete. We have to multiply with a basis function $\phi^*_\alpha(\mathbf{r})$ from the left side and to integrate over $\mathbf{r}$ to finally get

$$\int \phi^*_\alpha(\mathbf{r}) \left((H_{\mathrm{KS}}(\mathbf{r}) - \epsilon_i)\sum_\beta c_{i,\beta}\phi_\beta(\mathbf{r}) \right) d\mathbf{r} = 0 \tag{2.33}$$

$$\Leftrightarrow \int \left(\sum_\beta \phi^*_\alpha(\mathbf{r}) H_{\mathrm{KS}}(\mathbf{r})\phi_\beta(\mathbf{r}) - \epsilon_i \sum_\beta \phi^*_\alpha(\mathbf{r})\phi_\beta(\mathbf{r}) \right) c_{i,\beta} d\mathbf{r} = 0 \tag{2.34}$$

$$\Rightarrow (\hat{\mathbf{H}}_{\mathrm{KS}} - \epsilon_i \hat{\mathbf{S}})\mathbf{c}_i = 0. \tag{2.35}$$

The overlap matrix is denoted by $\hat{\mathbf{S}}$. This matrix equation can now be solved for the eigenvectors $\mathbf{c}_i$ representing the KS orbitals ψ_i and the eigenvalues ϵ_i equal to the KS eigenenergies. Still the basis set has to be defined. Two different basis sets based on a planewave basis will be explained in the following. In general a basis set with plane wavefunctions

$$\phi_{\mathbf{k},\mathbf{g}}(\mathbf{r}) = \frac{1}{\sqrt{V}} e^{\mathrm{i}(\mathbf{k}+\mathbf{g})\mathbf{r}} \tag{2.36}$$

expands the wavefunction into

$$\psi_{\nu,\mathbf{k}}(\mathbf{r}) = \sum_\beta^N c_{\beta,\nu,\mathbf{k}}\phi_{\mathbf{k},\beta}(\mathbf{r}). \tag{2.37}$$

Compared to (2.31) the index i of the single particle KS orbitals $\psi_i(\mathbf{r})$ is substituted by the Bloch wave vector $\mathbf{k}$ and in case of crystals additionally by the band index ν. To meet the definition of the planewave the index β labeling the basis functions corresponds

to the wave vector $\mathbf{g}$ of the planewave. It is chosen from the reciprocal lattice to ensure translation symmetry. Plane waves are orthonormal and hence the overlap matrix in (2.35) melts down to the unit matrix and the KS matrix equation is given by

$$\Rightarrow (\hat{\mathbf{H}}_{\mathrm{KS}} - \epsilon_{\nu,\mathbf{k}})\mathbf{c}_{\nu,\mathbf{k}} = 0. \tag{2.38}$$

The matrix of the KS Hamiltonian $\hat{\mathbf{H}}_{\mathrm{KS}}$ and the eigenvetor $\mathbf{c}_{\nu,\mathbf{k}}$ are

$$\hat{\mathbf{H}}_{\mathrm{KS}} = \begin{pmatrix} \int \phi^*_{\mathbf{k},\mathbf{g}_1}(\mathbf{r}) H_{\mathrm{KS}}(\mathbf{r}) \phi_{\mathbf{k},\mathbf{g}'_1}(\mathbf{r}) d\mathbf{r} & \dots & \int \phi^*_{\mathbf{k},\mathbf{g}_1}(\mathbf{r}) H_{\mathrm{KS}}(\mathbf{r}) \phi_{\mathbf{k},\mathbf{g}'_N}(\mathbf{r}) d\mathbf{r} \\ \vdots & \ddots & \vdots \\ \int \phi^*_{\mathbf{k},\mathbf{g}_N}(\mathbf{r}) H_{\mathrm{KS}}(\mathbf{r}) \phi_{\mathbf{k},\mathbf{g}'_1}(\mathbf{r}) d\mathbf{r} & \dots & \int \phi^*_{\mathbf{k},\mathbf{g}_N}(\mathbf{r}) H_{\mathrm{KS}}(\mathbf{r}) \phi_{\mathbf{k},\mathbf{g}'_N}(\mathbf{r}) d\mathbf{r} \end{pmatrix} \tag{2.39}$$

and

$$\mathbf{c}_{\nu,\mathbf{k}} = \begin{pmatrix} c_{\mathbf{g}'_1,\nu,\mathbf{k}} \\ \vdots \\ c_{\mathbf{g}'_N,\nu,\mathbf{k}} \end{pmatrix}. \tag{2.40}$$

Note that the kinetic energy part $\hat{\mathbf{T}}$ of the Hamiltonian $\hat{\mathbf{H}}_{\mathrm{KS}}$ is diagonal in the planewave basis. This is obvious because the matrix elements are $\phi_{\mathbf{k},\mathbf{g}}(\mathbf{r})(-\frac{\hbar^2}{2m}\nabla^2)\phi_{\mathbf{k},\mathbf{g}'}(\mathbf{r}) = \frac{\hbar^2}{2m}(\mathbf{k}-\mathbf{g}')^2\delta_{\mathbf{g},\mathbf{g}'}$. Furthermore $\hat{\mathbf{H}}_{\mathrm{KS}}$ is real symmetric rather than complex hermitian in case of inversion symmetric systems as will be derived at the end of the next chapter. Plane waves, while certainly a good choice for describing Bloch waves, are not useful for direct solutions of Schrödinger's equation in a crystal. Near the nuclei the potential is changing rapidly, thus also the wavefunctions vary vastly. Due to the highly oscillating wavefunctions an unmanageable number of planewave basis functions would have to be used. This is the reason why we either have to approximate the potential near the cores or why we have to extend the basis to treat the rapidly changing potentials in an appropriate way. If we want to use a pure planewave basis, pseudopotentials have to be introduced to overcome the problems near the core. Thereby the region near the atom cores is replaced by a sweet-tempered pseudopotential in such a way that the valence energy spectrum is reproduced. On the other hand complex but efficient basis sets, such as a set of linearized augmented-planewave (LAPW) or linearized muffin-tin orbitals (LMTO) can be used. Regions of slow varying potential are described by planewaves whereas regions of rapidly changing potential are expressed in a different basis making the description in this region more economical.
The full-potential linearized augmented-planewave (FLAPW) method is a DFT method employing a basis set of spherical harmonics plus radial functions to treat the potential and wavefunctions in spheres close to the atom cores and planewaves in the interstitial region between them. Due to the form of the spheres augmenting the planewave covered interstitial region, we get a muffin tin like sampling of the space which is sketched in figure 2.2. The radius of the spheres will therefore be called muffin-tin radius in the following. The advantage of using the full potential (see chapter 2.2.3) in contrast to the pseudo-potential mostly used in pure planewave (PW) codes introduces more complexity. Transition metals, their compounds and materials containing rare-earth elements seem to be best treated applying the LAPW method [96].

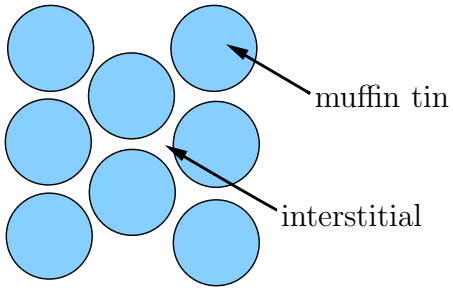

Figure 2.2: Sampling of the space by muffin-tin spheres and interstitial regions in the APW method. Blue circles represent the muffin-tin spheres.

The foundations for the FLAPW methods were laid in the 30th of the last century, when Slater [99] developed the augmented-planewave (APW) method in 1937. A draw back of the APW method is that the energies inside the muffin tins have to be the band energies as explained in the following section. In 1975 Andersen [5] improved APW by making a Taylor expansion around the band energies and thereby in a way linearized the APWs. In the 1980th [114] any shape approximation of the potential used in LAPW was dropped in favor of the full potential. For a closer review of the development of FLAPW have a look at the book of Singh [96] or the PhD thesis of P. Kurz [63].

2.2.1 FLAPW Basis Set - Bulk

From a didactically point of view it is reasonable to introduce the augmented planewave (APW) basis first. The basis functions are labeled by $\mathbf{g}$ and consists of single planewaves in the interstitial region matched to radial functions in the muffin-tin region around the cores. The single functions $\phi^{\mathrm{APW}}_{\mathbf{k},\mathbf{g}}(\mathbf{r})$ are named APWs.

$$\phi^{\mathrm{APW}}_{\mathbf{k},\mathbf{g}}(\mathbf{r}) = \frac{1}{\sqrt{V}} \begin{cases} e^{\mathrm{i}(\mathbf{k}+\mathbf{g})\mathbf{r}} & \text{interstitial region} \\ \sum_{lm} \left[A^{\alpha\mathbf{g}}_{lm}(\mathbf{k}) u^{\alpha}_{l}(r_\alpha)\right] Y_{lm}(\hat{r}_\alpha) & \alpha^{th} \text{ muffin tin} \end{cases} \tag{2.41}$$

The coefficients $A^{\alpha\mathbf{g}}_{lm}$ are determined by the condition that each basis function is continuous across the muffin-tin boundary. Any planewave can be expanded into spherical harmonics via the Rayleigh expansion, simplifying the determination of the coefficient at the boundary. The basis functions are normalized by the volume V of the unit cell. The index α labels the different muffin tins and r_α indicates that the coordinates are relative to the center of the αth muffin tin. Y_{lm} are spherical harmonics and u_l the solution of the radial Schrödinger equation

$$\left\{ -\frac{\hbar^2}{2m}\frac{\partial^2}{\partial r^2} + \frac{\hbar^2}{2m}\frac{l(l+1)}{r^2} + V(r) - E_l \right\} r u_l(r) \;=\; 0. \tag{2.42}$$

Here $V(r)$ denotes the potential inside the sphere explained in chapter 2.2.3 and E_l are energy parameters. If the energy parameters are kept fixed instead of being variational coefficients they define the basis set and thus wavefunctions and band energies could be calculated. Unfortunately for arbitrary energy parameters E_l this proceeding fails. The APWs are solutions of the Schrödinger equation inside the sphere only for the energies

E_l. If the band energies differ from the chosen energy parameters E_l the basis functions have too little variational freedom to allow changes in the wavefunctions. Thus the energy parameters have to be equal to the band energies and therefore they can not be obtained directly[3] from the diagonalization of the Hamiltonian matrix.
In 1975 Andersen [5] proposed an extension to the APW method solving the problem by an expansion of $u_l(r)$ in a Taylor series around the energy parameter E_l.

$$u_l(r,E) \quad = \quad u_l(r,E_l) + \dot{u}_l(r,E_l)(E-E_l) + ... \tag{2.43}$$

Only the constant and linear part is taken into account, hence in a way linearizes the APW basis. The energy derivative of $u_l(r)$ can be obtained from the energy derivative of equation (2.42).

$$\left\{ -\frac{\hbar^2}{2m}\frac{\partial^2}{\partial r^2} + \frac{\hbar^2}{2m}\frac{l(l+1)}{r^2} + V(r) - E_l \right\} r\dot{u}_l(r) \quad = \quad r u_l(r) \tag{2.44}$$

The new basis functions $\phi_{\mathbf{k},\mathbf{g}}(\mathbf{r})$ are called LAPWs and consist of a couple of radial functions and derivatives of radial functions in the muffin tins matched to a single planewave in the interstitial region between them.

$$\phi_{\mathbf{k},\mathbf{g}}(\mathbf{r}) = \frac{1}{\sqrt{V}} \begin{cases} e^{\mathrm{i}(\mathbf{k}+\mathbf{g})\mathbf{r}} & \text{interstitial region} \\ \sum_{lm} \left[A_{lm}^{\alpha\mathbf{g}}(\mathbf{k}) u_l^{\alpha}(r_\alpha) + B_{lm}^{\alpha\mathbf{g}}(\mathbf{k}) \dot{u}_l^{\alpha}(r_\alpha) \right] Y_{lm}(\hat{r}_\alpha) & \alpha^{th} \text{ muffin tin} \end{cases} \tag{2.45}$$

The coefficients $A_{lm}^{\alpha\mathbf{g}}, B_{lm}^{\alpha\mathbf{g}}$ are determined by the conditions that each basis function and its first radial derivative are continuous across the muffin-tin boundary. Since the basis inside the muffin tins is expended into a Taylor series around E_l, extra variational freedom to the basis inside the muffin tin is introduced. As a consequence the energy E_l in (2.42) do not have to be the exact band energy but some parameter close to the band energy. Thus it is possible to calculate the band energy by calculating the eigenvalues of the Hamiltonian matrix.
Instead of the above mentioned classical formulas a scalar relativistic approximation to the Dirac equation is applied and relativistic analogons to u_l and $\dot{u}_l$ equations are used within the `Fleur` program described in chapter 2.2.4. The size of the basis set is chosen by a cut off parameter for $\mathbf{g}$.
The defined basis function are not orthogonal, leading to a non diagonal overlap matrix:

$$\hat{\mathbf{S}} \quad = \quad \begin{pmatrix} \int \phi^*_{\mathbf{k},\mathbf{g}_1}(\mathbf{r}) \phi_{\mathbf{k},\mathbf{g}'_1}(\mathbf{r}) d\mathbf{r} & \dots & \int \phi^*_{\mathbf{k},\mathbf{g}_1}(\mathbf{r}) \phi_{\mathbf{k},\mathbf{g}'_N}(\mathbf{r}) d\mathbf{r} \\ \vdots & \ddots & \vdots \\ \int \phi^*_{\mathbf{k},\mathbf{g}_N}(\mathbf{r}) \phi_{\mathbf{k},\mathbf{g}'_1}(\mathbf{r}) d\mathbf{r} & \dots & \int \phi^*_{\mathbf{k},\mathbf{g}_N}(\mathbf{r}) \phi_{\mathbf{k},\mathbf{g}'_N}(\mathbf{r}) d\mathbf{r} \end{pmatrix} \tag{2.46}$$

It is feasible to exploit the properties of the basis set and the symmetry of the system under consideration in order to save some computational effort. All symmetry equivalent atoms belong to one atom type. Atoms are symmetry equivalent if there exists a space group operation mapping them onto each other. The quantities inside the muffin-tin sphere (e.g. radial function $u_l(r)$) are equal for all atoms of one atom type in the local coordinates. Thus they have to be calculated only once and can be translated to the other

[3] but with some further effort. See e.g. [96].

atoms of the same type. The computational afford can be significantly reduced if the system under consideration exhibits inversion symmetry because planewaves transform nicely under inversion symmetry. The inverted planewave is the complex conjugated.

$$I\left(e^{\mathrm{i}\mathbf{k}\cdot\mathbf{r}}\right) = e^{-\mathrm{i}\mathbf{k}\cdot\mathbf{r}} \quad = \quad \left(e^{\mathrm{i}\mathbf{k}\cdot\mathbf{r}}\right)^* \tag{2.47}$$

The interstitial part of the potential and wavefunction transforms this way and even the muffin-tin part does. By using the Rayleigh expansion and the properties of the spherical harmonics this can be proved [63]. Therefore if the system possesses inversion symmetry the LAPW basis functions transform according to

$$\phi_{\mathbf{k},\mathbf{g}}(-\mathbf{r}) \quad = \quad \phi^*_{\mathbf{k},\mathbf{g}}(\mathbf{r}). \tag{2.48}$$

This property of the basis functions simplifies the calculation to a large extent. The matrix elements of the KS Hamiltonian (2.39) can be transformed.

$$H_{\mathbf{k}}^{\mathbf{g},\mathbf{g}'} \quad = \quad \int \phi^*_{\mathbf{k},\mathbf{g}}(\mathbf{r}) H_{\mathrm{KS}}(\mathbf{r}) \phi_{\mathbf{k},\mathbf{g}'}(\mathbf{r}) d\mathbf{r} \tag{2.49}$$

$$= \int \phi_{\mathbf{k},\mathbf{g}}(-\mathbf{r}) H_{\mathrm{KS}}(\mathbf{r}) \phi^*_{\mathbf{k},\mathbf{g}'}(-\mathbf{r}) d\mathbf{r} \tag{2.50}$$

$$= \int \phi_{\mathbf{k},\mathbf{g}}(\mathbf{r}') H_{\mathrm{KS}}(\mathbf{r}') \phi^*_{\mathbf{k},\mathbf{g}'}(\mathbf{r}') d\mathbf{r}' = H_{\mathbf{k}}^{\mathbf{g}',\mathbf{g}} \tag{2.51}$$

In the last step $\mathbf{r} = -\mathbf{r}'$ was substituted and the inversion symmetry of the Hamiltonian $H_{\mathrm{KS}}(\mathbf{r}) = H_{\mathrm{KS}}(-\mathbf{r})$ was utilized. Since $H_{\mathbf{k}}^{\mathbf{g},\mathbf{g}'} = H_{\mathbf{k}}^{\mathbf{g}',\mathbf{g}}$ holds the Hamiltonian matrix $\hat{\mathbf{H}}_{\mathrm{KS}}$ is symmetric. Furthermore all operators are hermitian and $H_{\mathbf{k}}^{\mathbf{g},\mathbf{g}'} = \left(H_{\mathbf{k}}^{\mathbf{g}',\mathbf{g}}\right)^*$ is valid. This leads to

$$H_{\mathbf{k}}^{\mathbf{g},\mathbf{g}'} \quad = \quad \left(H_{\mathbf{k}}^{\mathbf{g}',\mathbf{g}}\right)^* = H_{\mathbf{k}}^{\mathbf{g}',\mathbf{g}}, \tag{2.52}$$

therefore the elements of the Hamiltonian matrix are real. The same holds for the overlap matrix and thus both the Hamilton matrix and the overlap matrix are real symmetric rather than complex hermitian.

2.2.2 FLAPW Basis Set - Film

A surface breaks the three dimensional translation symmetry of a bulk system down to a system with two dimensional translation symmetry parallel to the interface. Perpendicular to the surface we have a semi-infinite system. We will define the z direction to be perpendicular to the surface throughout this work.
An interface could be treated with a supercell setup, whereby the unit cell consists of slabs separated by a vacuum region and which is repeated in z direction. The vacuum region and the slabs have to be large enough to avoid interface-interface interactions. Problems arising from these interactions are called finite-size effects because they would not accrue in an infinite supercell. These kinds of setups are commonly used. They have the advantage that the bulk basis set can be employed and therefore films can be

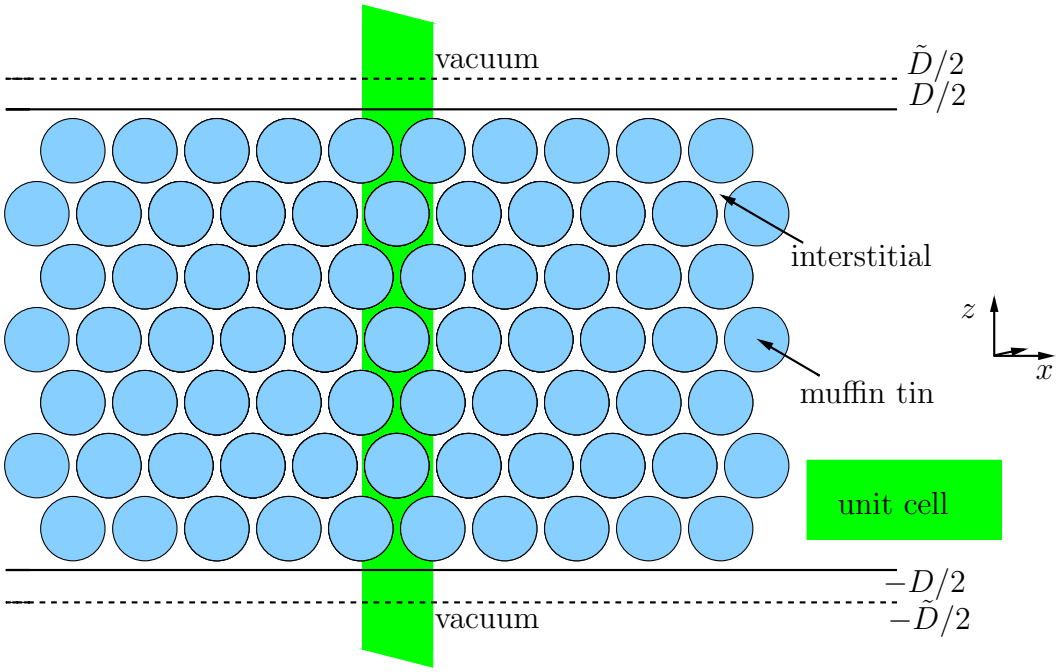

Figure 2.3: Film setup: Inside the slab the space is sampled with muffin-tin spheres (blue circles) and interstitial regions between them. The infinite vacuum region is treated with different basis functions.

calculated without developing a different code. But the other side of the picture is that the size of the unit cell increases drastically compared to a bulk unit cell resulting in a computational demanding task.
A different possible approach is to define a new basis set that can handle the vacuum region. The unit cell is a small slab, translation symmetric parallel to the surface and bordered by infinite vacuum regions in z direction. The cell is small compared to the one used in supercell calculations and the calculation times decrease. Still the slab should be thick enough to avoid the finite size effect. This method is called film calculation. Both methods have in common that the semi-infinite system is approximated by a finite system. To model real semi-infinite systems new methods have to be used like the Green function embedding technique which will be explained in chapter 2.4.
If we want to use a new basis set for the film calculation we have to divide the space into three regions. The muffin tins near the cores, the interstitial region between them and a vacuum region. The interstitial region stretches from $-D/2$ to $D/2$ in z direction defining the film thickness D (figure 2.3). The basis inside the muffin tins is the same as in the bulk case but the interstitial has to be treated differently. Since the periodicity in z direction is lost we have to decompose the planewaves in the interstitial region into a two dimensional periodical part parallel to the surface and an perpendicular part.

$$\phi^{\mathrm{PW}}_{\mathbf{k}_\parallel,\mathbf{g}_\parallel,g_\perp}(\mathbf{r}_\parallel,z) \;=\; e^{\mathrm{i}\mathbf{g}_\perp z}e^{\mathrm{i}(\mathbf{k}_\parallel+\mathbf{g}_\parallel)\mathbf{r}_\parallel} \tag{2.53}$$

with

$$\mathbf{g}_\perp \;=\; \frac{2\pi n}{\tilde{D}}. \tag{2.54}$$

$\tilde{D}$ is chosen larger than the film thickness D to gain greater variational freedom. In order to get the basis functions ϕ^{vac} for the vacuum region, we use a product of 2 dimensional planewaves parallel to the surface and an assumed z dependent function u with

$$\phi^{\text{vac}}_{\mathbf{k}_\parallel,\mathbf{g}_\parallel}(\mathbf{r}_\parallel, z) \;=\; u_{\mathbf{k}_\parallel,\mathbf{g}_\parallel}(z) e^{\mathrm{i}(\mathbf{k}_\parallel+\mathbf{g}_\parallel)\mathbf{r}_\parallel} \tag{2.55}$$

which has to satisfy the corresponding 1-dimensional Schrödinger equation

$$\left\{ -\frac{\hbar^2}{2m}\frac{\partial^2}{\partial z^2} + V_0(z) - E_{\text{vac}} + \frac{\hbar^2}{2m}(\mathbf{k}_\parallel + \mathbf{g}_\parallel)^2 \right\} u_{\mathbf{k}_\parallel,\mathbf{g}_\parallel}(z) \;=\; 0. \tag{2.56}$$

E_{vac} is the vacuum energy parameter. Again the basis function is linearized by the energy derivative $\dot{u}_{\mathbf{k}_\parallel,\mathbf{g}_\parallel}(z)$. The vacuum basis functions offer less variational freedom than the basis set of the interstitial region does. (e.g. there are only two vacuum functions with $\dot{u}_{\mathbf{k}_\parallel,\mathbf{g}_\parallel}(z)$ and $u_{\mathbf{k}_\parallel,\mathbf{g}_\parallel}(z)$ at $\mathbf{g}_\parallel$ to fit to all possible planewaves at $\mathbf{g}_\parallel$ in the interstitial region.)
The basis functions are now given by:

$$\phi_{\mathbf{k}_\parallel,\mathbf{g}_\parallel,g_\perp}(\mathbf{r}_\parallel, z) = \frac{1}{\sqrt{V}} \begin{cases} e^{\mathrm{i}g_\perp z} e^{\mathrm{i}(\mathbf{k}_\parallel+\mathbf{g}_\parallel)\mathbf{r}_\parallel} & \text{interstitial region} \\ \sum_{lm}\{A^{\alpha\mathbf{g}}_{lm}(\mathbf{k}) u^\alpha_l(r_\alpha) & \\ \quad + B^{\alpha\mathbf{g}}_{lm}(\mathbf{k}) \dot{u}^\alpha_l(r_\alpha)\} Y_{lm}(\hat{r}_\alpha) & \alpha^{th} \text{ muffin tin} \\ \{A_{\mathbf{g}_\parallel,g_\perp}(\mathbf{k}_\parallel) u_{\mathbf{k}_\parallel,\mathbf{g}_\parallel}(z) & \\ \quad + B_{\mathbf{g}_\parallel,g_\perp}(\mathbf{k}_\parallel) \dot{u}_{\mathbf{k}_\parallel,\mathbf{g}_\parallel}(z)\} e^{\mathrm{i}(\mathbf{k}_\parallel+\mathbf{g}_\parallel)\mathbf{r}_\parallel} & \text{vacuum} \end{cases} \tag{2.57}$$

The coefficients $A_{\mathbf{g}_\parallel,g_\perp}$ and $B_{\mathbf{g}_\parallel,g_\perp}$ are determined by the condition that each basis function is continuous across the interstitial-vacuum boundary.

2.2.3 Potential and Charge Density Representation

As mentioned before the FLAPW method employs the full potential. In order to describe the potential exactly instead of a constant interstitial potential a warped interstitial potential $\sum_{\mathbf{g}} V_{\mathbf{g}} e^{\mathrm{i}\mathbf{g}\cdot\mathbf{r}}$ is included. Also non spherical terms inside the muffin tin are introduced. The expansion of potential and charge density is done similar to the expansion of the wavefunction. This leads to the potential representation:

$$V(\mathbf{r}) \;=\; \begin{cases} \sum_{\mathbf{g}} V_{\mathbf{g}} e^{\mathrm{i}\mathbf{g}\cdot\mathbf{r}} & \text{interstitial region} \\ \sum_{lm} V^\alpha_{lm}(r) Y_{lm}(\hat{\mathbf{r}}_\alpha) & \text{muffin tin} \end{cases} \tag{2.58}$$

In the `Fleur` code the symmetry of the system is exploited to reduce the amount of coefficients to store. Obviously the charge density and the potential possess the symmetry of the lattice. In the interstitial region the planewaves can be replaced by symmetric planewaves called stars.

$$\Phi^{\text{3D}}_S(\mathbf{r}) \;=\; \frac{1}{N_{op}} \sum_{op} e^{\mathrm{i}\mathbf{R}\mathbf{g}(\mathbf{r}-\tau)} \tag{2.59}$$

All planewaves that can be transformed into each other by the symmetry operation $\mathbf{R}$ can be represented by one star. $\{\mathbf{R}|\tau\}$ are the symmetry operations of the lattice space

group [63]. In the vacuum region two dimensional stars Φ_S^{2D} are used. Inside the muffin tins the point group of the atom gives the relevant symmetry group. Thus we can also reduce the spherical harmonics inside the muffin tins. The symmetric functions are called lattice harmonics:

$$K_\nu(\hat{\mathbf{r}}) = \sum_m c^\alpha_{\nu,m} Y_{l,m}(\hat{\mathbf{r}}) \tag{2.60}$$

leading to the final representation of the potential

$$V(\mathbf{r}) = \left\{ \begin{array}{l|l} \sum_S V_S \Phi_S^{\mathrm{3D}}(\mathbf{r}) & \text{interstitial region} \\ \sum_S V_S(z) \Phi_S^{\mathrm{2D}}(\mathbf{r}) & \text{vacuum region} \\ \sum_\nu V_\nu^\alpha(r) K_\nu(\hat{\mathbf{r}}_\alpha) & \text{muffin tin} \end{array} \right. . \tag{2.61}$$

The electron density can be derived from the eigenfunctions as done before:

$$n(\mathbf{r}) = \frac{1}{V_{\mathrm{BZ}}} \int_{\mathrm{BZ}} \sum_\nu \sum_{E_{\nu,\mathbf{k}} < E_{\mathrm{F}}} |\psi_{\nu,\mathbf{k}}(\mathbf{r})|^2 d\mathbf{k} \tag{2.62}$$

Here ν denotes the band index, E_{F} the Fermi energy and the integration boundary of $\mathbf{k}$ is the Brillouin zone (BZ). In `Fleur` the integration over $\mathbf{k}$ is transformed into a weighted sum over the $\mathbf{k}$-point mesh. The $\mathbf{k}$-points are chosen from the irreducible part of the Brillouin zone. The weights depend on the integration method used. In order to cut off the energies above the Fermi level a step function could be applied. But to avoid charge oscillations during the self-consistency cycles a Fermi function instead of a step function is used in the code. If the wavefunction in the interstitial region is expressed by the planewave basis functions (2.41) we can rewrite equation (2.62) as

$$n(\mathbf{r}) = \frac{1}{V_{\mathrm{BZ}}} \int_{\mathrm{BZ}} \sum_\nu \sum_{E_{\nu,\mathbf{k}} < E_{\mathrm{F}}} \sum_{\mathbf{g}'} \sum_{\mathbf{g}''} (c_{\mathbf{g}',\nu,\mathbf{k}})^* c_{\mathbf{g}'',\nu,\mathbf{k}} e^{\mathrm{i}(\mathbf{g}''-\mathbf{g}')\mathbf{r}} d\mathbf{k}. \tag{2.63}$$

Since we can expand the electron density in the interstitial region into planewaves $n(\mathbf{r}) = \sum_{\mathbf{g}} n_{\mathbf{g}} e^{\mathrm{i}(\mathbf{gr})}$ the planewave coefficients can be given by

$$n_{\mathbf{g}} = \frac{1}{V_{\mathrm{BZ}}} \int_{\mathrm{BZ}} \sum_\nu \sum_{E_{\nu,\mathbf{k}} < E_{\mathrm{F}}} \sum_{(\mathbf{g}',\mathbf{g}'',\mathbf{g}''-\mathbf{g}'=\mathbf{g})} (c_{\mathbf{g}',\nu,\mathbf{k}})^* c_{\mathbf{g}'',\nu,\mathbf{k}} d\mathbf{k}. \tag{2.64}$$

Hence for a consistent representation the $\mathbf{g}$ cut-off should be twice as large as the one of the wavefunction basis. This increases the memory needed to store the coefficients. The representation of the electron density can be chosen equivalent to the one of the potential:

$$n(\mathbf{r}) = \left\{ \begin{array}{l|l} \sum_S n_S \Phi_S^{\mathrm{3D}}(\mathbf{r}) & \text{interstitial region} \\ \sum_S n_S(z) \Phi_S^{\mathrm{2D}}(\mathbf{r}) & \text{vacuum region} \\ \sum_\nu n_\nu^\alpha(r) K_\nu(\hat{\mathbf{r}}_\alpha) & \text{muffin tin} \end{array} \right. . \tag{2.65}$$

2.2.4 The `Fleur` code

`Fleur` is a Fortran code developed in the 'Institute für Festkörperforschung' (IFF) at the research center Jülich for (spindependent) DFT calculations employing a FLAPW basis set. Both bulk and film calculations can be done. Furthermore extensions to non collinear magnetism are implemented. It is (**k**-point) parallelized and can be used on a cluster of 41 IBM p690 nodes named Jump located at the research center Jülich. Jump has a total number of 1312 CPUs and an aggregate peak performance of 8.9 TFLOPS. It is possible to run calculations on 1 to 32 CPUs parallel or parallel on multiples of nodes (n times 32 CPUs). Throughout the program atomic units are used. The electron charge e, mass of the electron m and $\hbar$ all set equal to unity, lengths are given in Bohr radii (r_0=r_B=0.529177 Å) and energies are given in Hartree (1htr = 2Ry = 27.211 eV). Additional information about the program can be found at [119].

2.3 Green Function

Since 1828, when the Green function was first used by Green in the theory of electromagnetism the application of the Green function has become a well established tool in solid state physics. Compared to the wavefunctions the Green function contain all necessary information with less additional and most of the time unused information [91]. The Green function can be defined as the solution of an inhomogeneous differential equations[4]

$$[H(\mathbf{r}) - \xi]\, G(\mathbf{r}, \mathbf{r}'; \xi) \;=\; -\delta(\mathbf{r} - \mathbf{r}'), \tag{2.66}$$

where ξ is a variable for an (in general complex) energy and $H(\mathbf{r})$ represents the Hamiltonian

$$H(\mathbf{r}) \;=\; -\frac{1}{2}\nabla^2 + V_{\text{eff}}(\mathbf{r}) \tag{2.67}$$

$$H(\mathbf{r})\psi_i(\mathbf{r}) \;=\; \epsilon_i \psi_i(\mathbf{r}), \tag{2.68}$$

with a complete set of eigenfunctions ψ_i satisfying the time independent single-particle Schrödinger equation. Both Green function $G(\mathbf{r}, \mathbf{r}'; \xi)$ and the set of eigenfunctions ψ_i are subject to the same boundary conditions for $\mathbf{r}$ and $\mathbf{r}'$ on the surfaces S of the domain Ω. We can rewrite (2.66) and use that the eigenfunctions are, without loss of generality, orthonormal $\sum_i \psi_i(\mathbf{r})\psi_i^*(\mathbf{r}') = \delta(\mathbf{r} - \mathbf{r}')$.

$$G(\mathbf{r}, \mathbf{r}'; \xi) \;=\; \frac{\delta(\mathbf{r} - \mathbf{r}')}{[\xi - H(\mathbf{r})]} \tag{2.69}$$

$$\;=\; \frac{\sum_i \psi_i(\mathbf{r})\psi_i^*(\mathbf{r}')}{[\xi - H(\mathbf{r})]} \tag{2.70}$$

In general a function of an operator acts on a set of eigenfunction as the same function of eigenvalues does ($F(H)\psi_i = F(\epsilon_i)\psi_i$) and thus we gain

$$G(\mathbf{r}, \mathbf{r}'; \xi) \;=\; \sum_i \frac{\psi_i(\mathbf{r})\psi_i^*(\mathbf{r}')}{\xi - \epsilon_i}. \tag{2.71}$$

[4] sometimes defined with different sign and/or an additional factor of 4π.

This expansion of G in terms of the eigenfunctions ψ_i is called the spectral representation of G. In general the eigenspectrum of H can be discrete and continuous and therefore the sum in (2.71) is a sum over discrete energies plus an integration over the continuous part. Furthermore it is useful to transform from the $\mathbf{r}$-representation to a more general representation. The notation of choice is the one of Dirac with $\psi_i(\mathbf{r}) = \langle \mathbf{r}|\psi_i\rangle$, $G(\mathbf{r},\mathbf{r}';\xi) = \langle \mathbf{r}|G(\xi)|\mathbf{r}'\rangle$, $\delta(\mathbf{r}-\mathbf{r}')H(\mathbf{r}) = \langle \mathbf{r}|H|\mathbf{r}'\rangle$ and $1 = \int |\mathbf{r}\rangle\langle\mathbf{r}'|d\mathbf{r}$. Thus equation (2.71) can be rewritten in Dirac notation as

$$G(\xi) = \sum_i \frac{|\psi_i\rangle\langle\psi_i|}{\xi - \epsilon_i} + \int di \frac{|\psi_i\rangle\langle\psi_i|}{\xi - \epsilon_i}. \tag{2.72}$$

The Green function is an analytic function of ξ everywhere in the complex plane apart from the poles at the discrete eigenvalues of the Hamiltonian and branch cuts along parts of the real axis which correspond to the continuous spectrum of H. From equation (2.71) this can be seen directly. The Green function can be distinguish by

$$G^+(\mathbf{r},\mathbf{r}';\xi) = \lim_{\delta\to 0}\sum_i \frac{\psi_i(\mathbf{r})\psi_i^*(\mathbf{r}')}{(E+\mathrm{i}\delta)-\epsilon_i}, \text{ (retarded Green function)} \tag{2.73}$$

$$G^-(\mathbf{r},\mathbf{r}';\xi) = \lim_{\delta\to 0}\sum_i \frac{\psi_i(\mathbf{r})\psi_i^*(\mathbf{r}')}{(E-\mathrm{i}\delta)-\epsilon_i}. \text{ (advanced Green function)} \tag{2.74}$$

The retarded Green function G^+ is defined for real $\xi = E + \mathrm{i}\delta$ and is obtained from the general G by taking the limit $\delta \to 0$ with E real and δ positive and infinitesimal. The advanced Green function G^- is defined in the same way but approaches the limes from the other direction and therefore δ is negative and infinitesimal. For E belonging to the continuous spectrum of the Hamiltonian, the retarded Green Function consists only of outgoing the advanced Green Function only of incoming waves. For the other energies both Green functions are the same [70]. The density of states (DOS) can be derived [31] from the Green function by using the Dirac identity

$$\lim_{y\to 0}\frac{1}{x \pm \mathrm{i}y} = P\frac{1}{x} \mp \mathrm{i}\pi\delta(x), \tag{2.75}$$

where P is the principle value but is of little importance because we will concentrate on the imaginary part only. From the diagonal matrix element of the Green function we get:

$$G^\pm(\mathbf{r},\mathbf{r};\xi) = P\sum_i \frac{\psi_i(\mathbf{r})\psi_i^*(\mathbf{r})}{E-\epsilon_i} \mp \mathrm{i}\pi\sum_i \delta(E-\epsilon_i)\psi_i(\mathbf{r})\psi_i^*(\mathbf{r}) \tag{2.76}$$

$$\Rightarrow \Im(G^\pm(\mathbf{r},\mathbf{r};E)) = \mp\pi\sum_i \delta(E-\epsilon_i)|\psi_i(\mathbf{r})|^2 = \mp\pi n(\mathbf{r};E) \tag{2.77}$$

$n(\mathbf{r};E)$ is the local density of states (LDOS). We can derive the DOS $N(E) = \int n(\mathbf{r};E)$ by integration over $\mathbf{r}$

$$Tr\left(\Im\left(G^\pm(E)\right)\right) = \mp\pi\sum_i \delta(E-\epsilon_i) = \mp\pi N(E). \tag{2.78}$$

An important quantity which can be calculated directly from the local density of states (2.77) is the charge density.

$$n(\mathbf{r}) = \mp\frac{1}{\pi}\Im\int^{E_\mathrm{F}} G^{\pm}(\mathbf{r},\mathbf{r};E)dE \tag{2.79}$$

This equation is the basis for the self-consistent embedding scheme described in 2.4.4. In the following we will only work with the retarded Green function G^+. As G is analytic in the upper half plane integrations can be done along a path through the complex plane and thereby the singularities of G on the real axis can be avoided.

2.4 Green Function Embedding

Perturbation regions which reduce or even destroy the symmetry of the system under consideration are difficult to handle but they are crucial to understand the physical properties of the system. For example impurities in crystals, while breaking the crystal symmetry completely, influence the crystal behavior in an electric field or under mechanical stress. Interfaces or surfaces reduce the 3-dimensional symmetry of the bulk system to a 2-dimensional system parallel to the interface and give rise to new electronic structures like surface states. A new technique is needed to treat such localized impurities surrounded by an infinite unperturbated system. An effective method named 'Green function embedding' was introduced by Inglesfield in 1981 [50] and is used in this work.

In general to completely solve the time-independent Schrödinger equation, which is a second order partial differential equation in a given volume we need a set of boundary conditions. These conditions might be a set of values and derivatives of the wavefunction at the boundary of the perturbed region. While this straightforward approach looks reasonable, solving this task numerically is difficult. For each energy an initial value exists for which the solving wavefunction grows or decays exponentially. This leads to an exponentially growth of the error of any numerical inaccuracy of the initial value. Inglesfield's embedding technique circumvents this numerical problem. In the following part a short derivation of this technique will be given. Imagine an embedded region Ω with Green function G and wavefunction ϕ inside an outer region V_0 with G_0 and ψ_0. We have to find the minimized energy expectation value of a wavefunction Ψ, which is given by ϕ inside and ψ_0 outside the embedding region, by varying Ψ. The amplitudes

$$\text{embedded region}: \quad \Omega, G, \phi \tag{2.80}$$
$$\text{outer region}: \quad V_0, G_0, \psi_0 \tag{2.81}$$

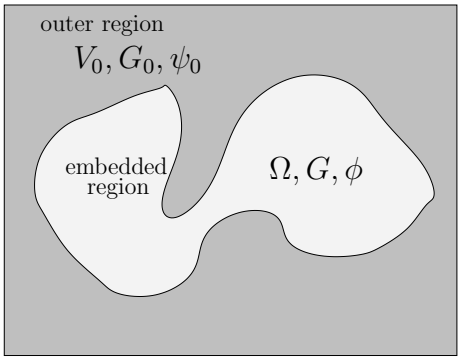

of ϕ and ψ_0 have to match at the boundary S.

$$\begin{aligned} \Psi &= \begin{cases} \phi & \text{in } \Omega \\ \psi_0 & \text{in } V_0 \end{cases} \\ \phi(\mathbf{r}_S) &= \psi_0(\mathbf{r}_S) \end{aligned} \tag{2.82}$$

The outer wavefunction ψ_0 can be chosen in a way that the boundary conditions at the outer surface of V_0 are fulfilled and the amplitude can be adjusted such that the total wavefunction Ψ is continuous across the boundary. But for a general trial function ϕ it is not possible to have a continuous derivative of Ψ all over the boundary S. This leads to an additional surface term in the expectation value of the energy.
To understand this keep in mind that the Hamiltonian is hermitian in the complete volume:

$$\int \Psi^*(\mathbf{r}) H \Psi'(\mathbf{r}) d^3r = \int \Psi'^*(\mathbf{r}) H \Psi(\mathbf{r}) d^3r \tag{2.83}$$

and therefore

$$\int_{V_0+\Omega} \Psi^*(\mathbf{r}) \nabla^2 \Psi(\mathbf{r}) d^3r = -\int_{V_0+\Omega} \nabla\Psi^*(\mathbf{r}) \nabla\Psi(\mathbf{r}) d^3r. \tag{2.84}$$

Obviously no surface term exists, which is reasonable because the complete volume is infinite. If we now evaluate the integral by taking into account the different regions and denoting the derivative normal to the interface by ∂_n we gain:

$$\int_{V_0+\Omega} \Psi^*(\mathbf{r}) \nabla^2 \Psi(\mathbf{r}) d^3r = -\int_{V_0+\Omega} \nabla\Psi^*(\mathbf{r}) \nabla\Psi(\mathbf{r}) d^3r \tag{2.85}$$

$$= -\int_{V_0} \nabla\psi^*(\mathbf{r}) \nabla\psi(\mathbf{r}) d^3r - \int_{\Omega} \nabla\phi^*(\mathbf{r}) \nabla\phi(\mathbf{r}) d^3r \tag{2.86}$$

$$\underbrace{=}_{2^{\text{nd}}\text{ Green}} \int_{V_0} \psi^*(\mathbf{r}) \nabla^2 \psi(\mathbf{r}) d^3r - \int_{\partial(V_0+\Omega)} \psi^* \partial_n \psi d^2r + \int_{\Omega} \phi^*(\mathbf{r}) \nabla^2 \phi(\mathbf{r}) d^3r - \int_{\partial(V_0+\Omega)} \phi^* (-\partial_n \phi) d^2r \tag{2.87}$$

Thus the energy expectation value is:

$$E = \frac{\int \Psi^*(\mathbf{r}) H \Psi(\mathbf{r}) d^3r}{\int \Psi^*(\mathbf{r}) \Psi(\mathbf{r}) d^3r} \tag{2.88}$$

$$= \frac{\int_{V_0} \psi^*(\mathbf{r}) H \psi(\mathbf{r}) d^3r + \int_{\Omega} \phi^*(\mathbf{r}) H \phi(\mathbf{r}) d^3r + \frac{1}{2} \int_{\partial(V_0+\Omega)} (\phi^* \partial_n \phi - \psi^* \partial_n \psi) d^2r}{\int_{V_0+\Omega} \Psi^*(\mathbf{r}) \Psi(\mathbf{r}) d^2r} \tag{2.89}$$

$$= \frac{\epsilon \int_{V_0} \psi^*(\mathbf{r}) \psi(\mathbf{r}) d^3r + \int_{\Omega} \phi^*(\mathbf{r}) H \phi(\mathbf{r}) d^3r + \frac{1}{2} \int_{\partial(V_0+\Omega)} \phi^* (\partial_n \phi - \partial_n \psi) d^2r}{\int_{V_0+\Omega} \Psi^*(\mathbf{r}) \Psi(\mathbf{r}) d^3r}, \tag{2.90}$$

because $H\psi = \epsilon\psi$ holds in the outer region. If the embedding region is small compared to the outer region we can assume $\epsilon = E$ and the equation for the expectation value simplifies to

$$E = \frac{\int_{\Omega} \phi^*(\mathbf{r}) H \phi(\mathbf{r}) d^3r + \frac{1}{2} \int_{\partial(V_0+\Omega)} \phi^* (\partial_n \phi(\mathbf{r}_S) - \partial_n \psi(\mathbf{r}_S)) d^2r}{\int_{\Omega} \phi^*(\mathbf{r}) \phi(\mathbf{r}) d^3r}. \tag{2.91}$$

By assuming the continuity (2.82) on the surface one can vary the energy expectation value for ϕ^* and obtain:

$$(H(\mathbf{r}) - E)\,\phi(\mathbf{r}) + \frac{1}{2}\delta(n - n_S)\,[\partial_n\phi(\mathbf{r}) - \partial_n\psi(\mathbf{r})] \;=\; 0 \tag{2.92}$$

The second term acts on the surface only and n is the normal component of the vector $\mathbf{r}$. The problem in this equation is $\psi(\mathbf{r})$ because its value is not known in advanced. Note also that the normal derivative $\partial_n\psi$ is energy dependent and therefore equation (2.92) does not define an eigenvalue problem for E anymore. The equation can be seen as a Schrödinger equation for the embedded region Ω which is matched to the energy E and the solution ψ in the outer region V_0.

2.4.1 Introducing the Embedding Potential

By introducing an embedding potential we can solve equation (2.92) without knowing the normal derivative $\partial_n\psi(\mathbf{r})$. In the outer volume V_0 the Schrödinger equation and the defining equation for the Green function G_0 are

$$(H(\mathbf{r}) - E)\,\psi(\mathbf{r}) \;=\; 0 \tag{2.93}$$

$$\text{and}\quad (H(\mathbf{r}) - E)\,G_0(\mathbf{r}, \mathbf{r}', E) \;=\; -\delta(\mathbf{r} - \mathbf{r}'). \tag{2.94}$$

After multiplying (2.93) with $G_0(\mathbf{r}, \mathbf{r}', E)$ and (2.94) with $\psi(\mathbf{r})$ we can combine both and build the integral over V_0. This leads to

$$\int_{V_0} G_0(\mathbf{r}, \mathbf{r}', E)\,(H - E)\,\psi(\mathbf{r}) - \psi(\mathbf{r})\,(H - E)\,G_0(\mathbf{r}, \mathbf{r}', E)dV \tag{2.95}$$

$$= \int_{V_0} \delta(\mathbf{r} - \mathbf{r}')\psi(\mathbf{r})dV = \psi(\mathbf{r}'). \tag{2.96}$$

The Hamiltonian can be expressed by $H(\mathbf{r}) = -\frac{1}{2}\nabla^2 + V(\mathbf{r})$. If the potential $V(\mathbf{r})$ is local the equation reduces to

$$\psi(\mathbf{r}') \;=\; -\frac{1}{2}\int_{V_0} G_0(\mathbf{r}, \mathbf{r}', E)\nabla^2\psi(\mathbf{r}) - \psi(\mathbf{r})\nabla^2 G_0(\mathbf{r}, \mathbf{r}', E)dV \tag{2.97}$$

$$\underbrace{=}_{2^{\text{nd}}\ \text{Green's law}} -\frac{1}{2}\int_{\partial V_0} G_0(\mathbf{r}, \mathbf{r}', E)\partial_n\psi(\mathbf{r}) - \psi(\mathbf{r})\partial_n G_0(\mathbf{r}, \mathbf{r}', E)dS. \tag{2.98}$$

We can choose a Green function G_0 which holds von-Neumann conditions on S and thus the formula simplifies to

$$\psi(\mathbf{r}') \;=\; -\frac{1}{2}\int_{\partial V_0} G_0(\mathbf{r}, \mathbf{r}', E)\partial_n\psi(\mathbf{r})dS. \tag{2.99}$$

In the following $\mathbf{r}'$ at the surface S will be expressed by $\mathbf{r}'_S$. Using the notation G_S for the surface projection of the Green function G_0 and inverting the equation for $\partial\psi$:

$$\partial_n\psi(\mathbf{r}_S) \;=\; 2\int_{\partial V_0} G_S^{-1}(\mathbf{r}_S, \mathbf{r}'_S, E)\psi(\mathbf{r}'_S)dS' \tag{2.100}$$

G_S^{-1} is called 'embedding potential' and can also be denoted by Σ.

$$\partial_n \psi(\mathbf{r}_S) \;=\; 2\int_{\partial V_0} \Sigma(\mathbf{r}_S, \mathbf{r}'_S, E)\psi(\mathbf{r}'_S)dS' \tag{2.101}$$

It is important that the embedding potential can be seen as a generalized logarithmic derivative. The solution of the Schrödinger equation is determined uniquely by the generalized logarithmic derivative together with the normalization of the wavefunction. Σ is a linear operator acting on the wavefunction at the boundary returning the normal derivative.
Equation (2.92) can now be written as

$$(H(\mathbf{r})-E)\phi(\mathbf{r}) + \frac{1}{2}\delta(n-n_S)\left[\partial_n\phi(\mathbf{r}) - 2\int_{\partial V_0}\Sigma^{-1}(\mathbf{r}_S,\mathbf{r}'_S,E)\phi(\mathbf{r}'_S)dS'\right] = 0 \tag{2.102}$$

or in short and symbolic notation like

$$\left(H_{\mathrm{emb}}(E) - E\right)\phi(\mathbf{r}) \;=\; 0. \tag{2.103}$$

The identity (2.82) was used once more. By introducing the embedding potential we can now treat the embedded region without knowing the normal derivative on the surface of the outer region wavefunction.

2.4.2 Embedded Green Function

A direct solution of (2.103) for the wavefunction ϕ inside the embedded region Ω is in general not possible because H_{emb} is energy dependent and therefore the equation is non-linear. The quantity to look at is the embedded Green function G.

$$(H_{\mathrm{emb}}(E) - E)G(\mathbf{r},\mathbf{r}',E) \;=\; -\delta(\mathbf{r}-\mathbf{r}') \tag{2.104}$$

In a direct transfer the embedding potential can be used to obtain the surface normal derivative of the Green function

$$\partial_n G(\mathbf{r}_S,\mathbf{r}'_S,E) \;=\; 2\int \Sigma(\mathbf{r}_S,\mathbf{r}''_S,E)G(\mathbf{r}''_S,\mathbf{r}'_S,E)dS'' \tag{2.105}$$

Note that G is the embedded Green function in region Ω whereas the embedding potential Σ is the surface projected Green function of G determined by the outer volume V_0 with different boundary conditions.

2.4.3 Summary of the Embedding Technique

Whenever we have to treat an embedded region within an outer region we can use the explained method of embedding to find the Green function of the embedded region. Equation (2.92) holds for the embedded region

$$\left(H(\mathbf{r}) - E\right)\phi(\mathbf{r}) + \frac{1}{2}\delta(n-n_S)\left[\partial_n\phi(\mathbf{r}) - \partial_n\psi(\mathbf{r})\right] \;=\; 0 \tag{2.106}$$

but the surface normal derivative of the outer region wavefunction is not known.[5] Therefore the embedding potential Σ has to be introduced (2.101):

$$\partial_n \psi(\mathbf{r}_S) = 2 \int_{\partial V_0} \Sigma(\mathbf{r}_S, \mathbf{r}'_S, E) \psi(\mathbf{r}'_S) dS' \tag{2.107}$$

Leading to an equation (2.103) for the embedded wavefunction ϕ which can in general not be solved directly. Thus the embedded Green function (2.104) is the property to investigate.

$$(H_{\text{emb}}(E) - E)\, G(\mathbf{r}, \mathbf{r}', E) = -\delta(\mathbf{r} - \mathbf{r}') \tag{2.108}$$

2.4.4 Self-consistent Embedding

It was already derived in section 2.3 that the charge density (2.79) can be calculated from the Green function directly.

$$n(\mathbf{r}) = -\frac{1}{\pi} \Im \int^{E_{\text{F}}} G(\mathbf{r}, \mathbf{r}; E) dE \tag{2.109}$$

This enables us to use the Green function embedding method within a self-consistency cycle. After calculating the embedded Green function the charge density is calculated and maybe mixed with previous ones. From the charge density the Hartree potential can be derived which is then used in the calculation of a new Green function. This cycle can be run until the charge density in each step does not differ from the previous one and thus a self-consistent charge density is achieved. Most easily the principle of self-consistent embedding [48] can be shown in the following flowchart. In a Green function embedding

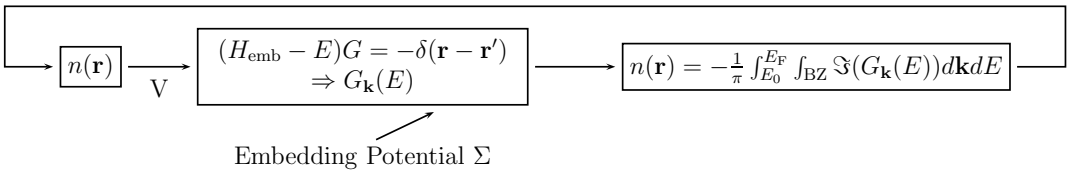

calculation the self-consistency cycle is important in order to get good, stable and reliable results. Furthermore the introduction of an external electric field to the system or the alignment of the vacuum potential towards the image potential like behavior will need the self-consistency cycle in order to reproduce the correct physical properties like screened charges in the former and smooth potentials in the latter case.

[5] Since the embedding method will be used together with the DFT the Hamiltonian $H(\mathbf{r})$ is substituted by the introduced Kohn-Sham Hamiltonian $H_{\text{KS}}(\mathbf{r})$.

2.5 Complex Band Structure

In general bulk states have to fulfill the Schrödinger equation $H\psi = E\psi$ and the Bloch theorem $T_{\mathbf{R}}\psi = e^{\mathrm{i}k\mathbf{R}}\psi$. The translation operator $T_{\mathbf{R}}$ commutates with the Hamiltonian and thus both have the same eigenfunctions. We can concentrate on real energies E because they have physical meaning. The solution of the Schrödinger equation for an infinite bulk should be normalized and therefore the Bloch waves (2.110) fulfilling the Bloch theorem have to have real **k**-vectors.
If the bulk is facing a surface or a perturbation region, the pure bulk Bloch states are insufficient to match with the solution in the surface or perturbation region. The solution space in the bulk has to be increased. This can be done by adding the infinite set of evanescent or Tamm waves (2.111) with complex **k** to the finite set of possible Bloch states with real **k**-vector. The surface or perturbation region breaks the three dimensional symmetry of the system and therefore complex **k**-vectors become possible.

Bloch wave

$$\psi_k(z+a) \;=\; e^{\mathrm{i}ka}\psi_k(z) \qquad (2.110)$$

evanescent wave

$$\psi_\pm(z+a) \;=\; -e^{\pm\kappa a}\psi_\pm(z) \qquad (2.111)$$

The complex vectors **k** are giving possible solutions which decay exponentially (2.111) towards the vacuum. Note that even though they only appear at surfaces or impurities the evanescent states are actually bulk properties and can be calculated in the bulk system if one formally allows complex **k**-vectors to characterize the solution of the Schrödinger equation.

The Bloch bandstructure $E(\mathbf{k})$ with real energy and real Bloch vector is becoming a generalized bandstructure $\epsilon(\mathbf{k})$ with $\epsilon, \mathbf{k} \in \mathbb{C}$. The subset of complex **k**-vectors with real energies E are called real lines and all real lines built the complex bandstructure [57]. In the following a short summary of the main features of this complex band structure (CBS) is given. In order to investigate the properties of the CBS an one dimensional section $E(k_z)$ of the complex $E(\mathbf{k})$ is made. That means $\mathbf{k}_\parallel$ is set to a real value. Thus $E(\mathbf{k})$ is a complex function of the complex variable k_z. First of all $E(\mathbf{k})$ is real if k_z is real. These are the lines in the Bloch bandstructure. But $E(\mathbf{k})$ stays real for a defined range of imaginary values of k_z at the Brillouin zone boundary. This can be easily seen because for $k_z = \pi/a \pm \mathrm{i}\kappa$ in (2.111) we get the usual form of Bloch theorem (2.110). All pairs of bands are joined by loops of real lines with complex **k**. Not only at the zone boundary the bands are connected by loops but also close to minima and maxima in the bandstructure. At an extremum $E_0(k_0)$ the derivative is $dE/dk_z = 0$ and E behaves like

$$E(k_z) \;=\; E_0 + c_r(k_z - k_0)^2 \qquad (2.112)$$

where c_r is a real constant. We get real energies for either real or imaginary values of $k_z - k_0$. Thus the energy will be real on a line which crosses the real plane at the point k_0 at right angles and on the real axis itself. Therefore the real energy has a saddle point at k_0 in the complex plane. For a more sophisticated proof take a look at [42]. Beside the loops there also exist real lines running to infinity, where they cannot create loops. They

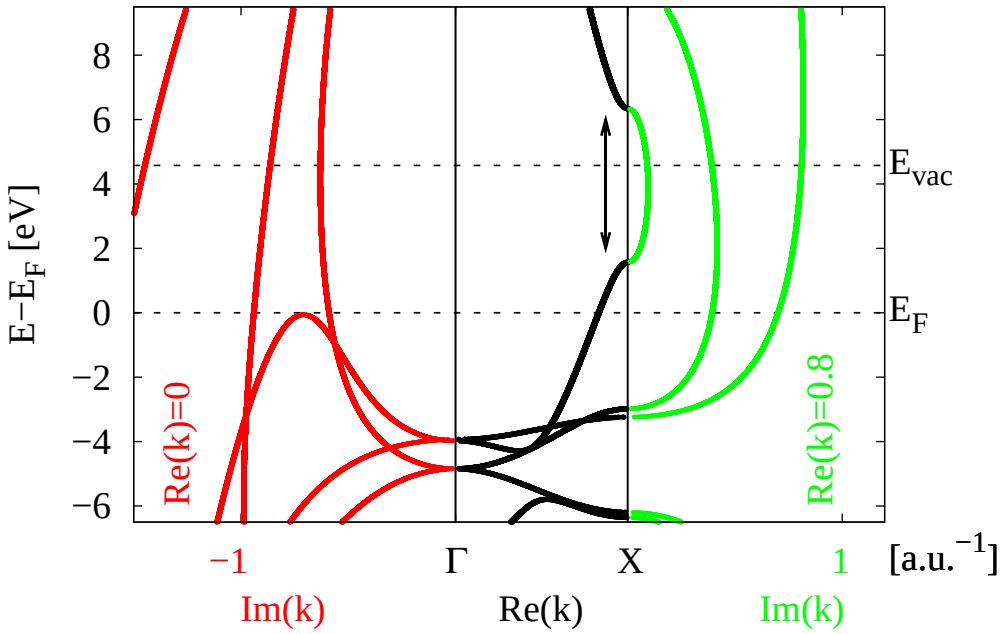

Figure 2.4: Complex band structure of Ag. Black lines represent the Bloch band between the Bloch vectors $\mathbf{k} = \Gamma$ and $\mathbf{k} = X$. Red lines belong to complex bands with $Re(\mathbf{k}) = \Gamma$ and green lines to complex bands with $Re(\mathbf{k}) = X$. (The theoretical lattice constant of a=4.147 Å is used.)

run of to $\Im(k_z) = \pm\infty$ with $k_z = -\mathrm{i}\sqrt{[(k_x + m\pi/a)^2 + (k_y + m\pi/a)^2 - E]}$ as derived in [42]. In figure 2.4 the complex band structure of silver is plotted. Since only real lines are building the CBS the energy is real. The parallel components of $\mathbf{k}$ are chosen to be at the $\overline{\Gamma}$ point of the two-dimensional Brillouin zone. The black lines are building the band structure of Bloch states with real $\mathbf{k}$-vectors along a line in the bulk Brillouin zone which is projected onto the same $\mathbf{k}_\parallel$ point of the two dimensional Brillouin zone. The red lines are representing states with $k_z = q_z + \mathrm{i}\kappa$ where q_z is equal to 0. The green lines belong to $q_z = \frac{\pi}{a}$. It can be seen that the zone boundary of the band in the CBS are not connected by loops but that the real lines run to infinity. More exciting CBS of Cu(001), Fe(001) and Si(111) can be found in the publication of Wortmann *et al.* [117]. It is instructive to compare the complex bandstructure to the corresponding Bloch band structure in figure 2.5. In this figure the region $\Gamma - X$ is emphasized to pronounce the analogy to the middle region of the CBS shown in figure 2.4. The bandstructure is calculated employing `Fleur` the complex bandstructure using the `GFleur` code. A more detailed investigation of the CBS can be found in the publications of Heine from 1963 [42] and 1964 [43].

2.6 The `GFleur` Code

The `GFleur` code [116] uses the Green function embedding technique in the framework of the FLAPW `Fleur` code. The FLAPW basis set is chosen in the embedded region and the startup potential and charge density is given by a `Fleur` supercell or bulk

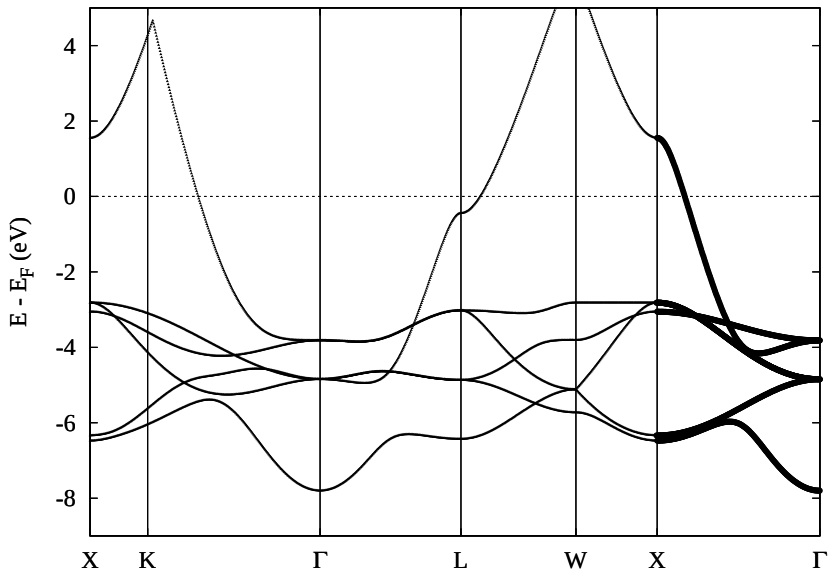

Figure 2.5: Bloch band structure of Ag. Region between Γ and X highlighted. (Calculated with the experimental lattice constant of 4.09 Å)

calculation. From the bulk system the embedding potential can be calculated and add to an interface region cut out of the supercell setup. Since the embedding potential of a vacuum region can be analytically calculated and add to one side of the system, surfaces can be investigated. By this we can treat real semi-infinite surfaces, in contrast to `Fleur` surface calculations. Instead of the embedding potential of a vacuum region an embedding potential from another material can be added and thus a stack system can be modeled. In both cases the Green function inside the embedded region is determined by an extended Kohn-Sham equation considering the interface of the embedded region [51, 52, 117, 118]. The embedded Green function can be used to calculate the electronic structure or the transport through the system under investigation. As the charge density can be derived from the Green function and the Green function depends itself on the charge density of the system a self-consistent scheme can be used to calculate a self-consistent charge density of the embedded region.

2.6.1 The `GFleur` Basis Set

Since the embedded region is periodic only in two dimensions perpendicular to the boundary surface we have to introduce another basis than the `Fleur` bulk basis (2.45). In principle, it is the same problem faced already in the FLAPW film calculations. The bulk symmetry is broken in one direction and the basis set has to be modified. The solution is analogous to the basis set of the `Fleur` film calculation (2.57). The basis functions for the interstitial are separated into an in-plane component and a component perpendicular to the boundary surface. Inside the muffin tins the basis functions are not modified because the muffin tins are never cut at any interface. Thus the basis functions

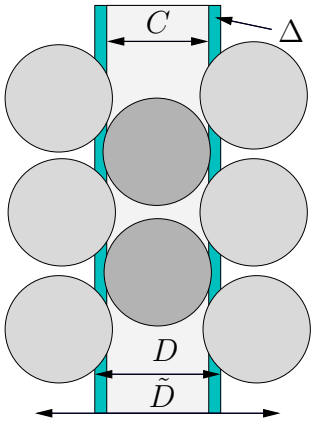

Figure 2.6: Cutting a slab out of a supercell. Region C is one principle layer.

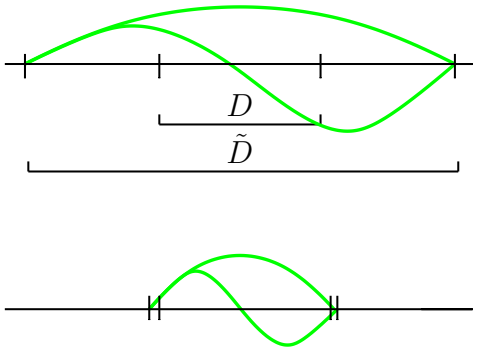

Figure 2.7: Choice of an appropriate $\tilde{D}$. Basis functions should offer enough variational freedom in region D.

are:

$$\phi^{\mathrm{3D}}_{\mathbf{k}_\parallel,\mathbf{g}_\parallel,g_\perp}(\mathbf{r}_\parallel,z) = \frac{1}{\sqrt{V}} \begin{cases} e^{\mathrm{i}(\mathbf{k}_\parallel+\mathbf{g}_\parallel)\mathbf{r}_\parallel} e^{\mathrm{i}g_\perp z} & \text{interstitial region} \\ \sum_{lm}[A^{\alpha\mathbf{g}}_{lm}(\mathbf{k})u^\alpha_l(r_\alpha) & \\ +B^{\alpha\mathbf{g}}_{lm}(\mathbf{k})\dot{u}^\alpha_l(r_\alpha)]Y_{lm}(\hat{r}) & \alpha^{th} \text{ muffin tin} \end{cases} \tag{2.113}$$

Due to the lacking periodicity perpendicular to the surface $g_\perp$ is set to

$$g_\perp = \frac{2\pi n}{\tilde{D}}. \tag{2.114}$$

Again the similarity with the FLAPW film calculation becomes obviously. The value of $\tilde{D}$ has to be larger than D but not too large. If $\tilde{D}$ and D are nearly the same it is hard to get the correct value at the D boundaries, if $\tilde{D}$ is chosen too large the basis functions are similar inside the D region and the basis becomes linear dependent. Draft 2.7 visualize this. The number of basis functions is given by the number of chosen $\mathbf{g}_\parallel$ and $g_\perp$. This is done either by taking them from a spherical shaped subset in the reciprocal space of radius $rk_{\max}$ or by a cylinder like shaped subset of radius $rk_{\max}$.[6] The hight of the cylinder is determined by a parameter called 'napw' by the condition that the number of $g_\perp$ is two times 'napw' plus an additional one. But we have to treat two different regions in an embedding code. On the one hand the three dimensional space inside the embedding region (2.113). This space is subdivided into muffin tins and interstitial. On the other hand it is appropriate to introduce a different basis for a second region. The region covers the boundary surface and is two dimensional (2.115). At the surface the basis is defined by

$$\phi^{\mathrm{2D}}_{\mathbf{k}_\parallel,\mathbf{g}_\parallel}(\mathbf{r}_\parallel) = \frac{1}{\sqrt{V}} e^{\mathrm{i}(\mathbf{k}_\parallel+\mathbf{g}_\parallel)\mathbf{r}_\parallel}. \tag{2.115}$$

Additionally the charge density and the potential inside the interstitial region are expended by a basis set at least twice as large as the wavefunction basis set.

[6] it is $k_{\max}$ with an additional r indicating a real variable in Fortran and has a historical reason

The `GFprep` tool can cut regions out of `Fleur` supercells and extract the corresponding potentials. A plain interface is much easier to handle than a curved interface. But because of the FLAPW basis set a cut through the muffin tins at the boundary is forbidden. One solution to avoid the interface curving around the muffin tins is to introduce a new region including the muffin tins and some additional space. This is sketched in figure 2.6. The embedding region with width C is cut out of a FLAPW setup. The plain boundary would cut through the muffin-tin spheres. Thus, instead of region C the region D is cut ignoring the muffin tins cutting from outwards into the region. The region between C and D is called delta region Δ and the potential inside this region is set to a constant value.

2.6.2 Construction of the Coulomb Potential

The Hartree potential V_{H} can be derived from the charge density via the Poisson equation.

$$\Delta V_{\mathrm{H}}(\mathbf{r}) \;=\; 4\pi\rho(\mathbf{r}) \tag{2.116}$$

While for the muffin tins the potential can be calculated in a straightforward manner for the interstitial region some more steps have to be taken. The Poisson equation can be easily solved in reciprocal space.

$$V_{\mathrm{H}}(\mathbf{g}) \;=\; 4\pi\frac{\rho(\mathbf{g})}{\mathbf{g}^2} \text{ for } \mathbf{g}\neq 0 \tag{2.117}$$

Pseudocharge density As the charge density varies rapidly close to the cores solving equation (2.117) directly is impractical. By applying the pseudocharge method developed by Weinert [112] this problem can be circumvented. While the charge density is given by

$$\rho(\mathbf{r}) \;=\; \left\{ \begin{array}{c|l} \sum_s \rho_S \Phi_S^{\mathrm{3D}}(\mathbf{r}) & \text{interstitial region} \\ \sum_\nu \rho_\nu^\alpha(r) K_\nu(\hat{\mathbf{r}}) & \text{muffin tin} \end{array} \right. \tag{2.118}$$

the pseudocharge density is defined by

$$\tilde{\rho}(\mathbf{r}) \;=\; \left\{ \begin{array}{c|l} \rho(\mathbf{r}) & \text{interstitial region} \\ \text{function with same multipol}- & \text{muffin tin} \\ \text{moments as } \rho(\mathbf{r}) & \end{array} \right. . \tag{2.119}$$

Φ_S^{3D} are the symmetric planewaves called stars and $K_\nu(\hat{\mathbf{r}})$ are the lattice harmonics introduced in the chapter concerning the `Fleur` code. The pseudocharge trick smoothens the charge density inside the embedding region without missing the essential behavior inside the muffin-tin region which is determined by the multipol moment. Thus we can apply formula (2.117) after a Fourier transformation of $\tilde{\rho}$ in order to get the interstitial potential $V_{\mathrm{int}}(\mathbf{g})$.

$$\tilde{\rho}(\mathbf{r}) \overset{\mathrm{FT}}{\Rightarrow} \tilde{\rho}(\mathbf{g}) \overset{V_{\mathrm{int}}(\mathbf{g})=\tilde{\rho}(\mathbf{g})/\mathbf{g}^2}{\Rightarrow} V_{\mathrm{int}}(\mathbf{g}) \tag{2.120}$$

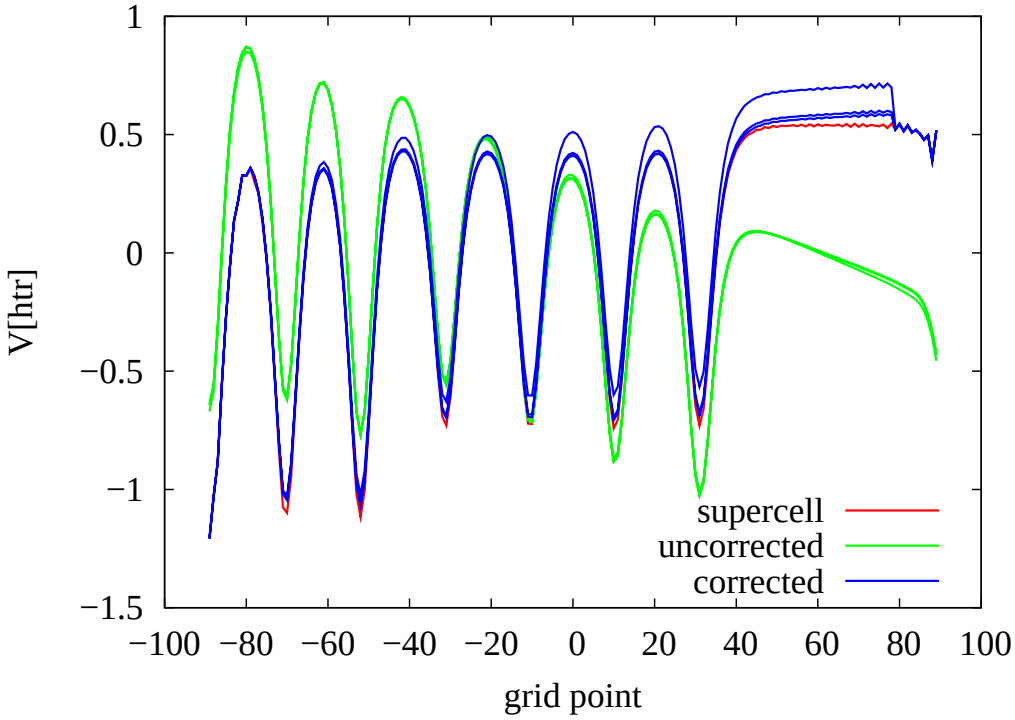

Figure 2.8: The lateral averaged potential of a platinum substrate with four layers of silver is plotted. The red curve gives the potential obtained from a supercell calculation. The blue curves give the potential obtained in the Green function embedding calculation of the first three self-consistency cycles. The potentials calculated without boundary conditions are represented by the green lines.

Coulomb potential The potential is represented in the same way than the charge density.

$$V(\mathbf{r}) \quad = \quad \left\{ \begin{array}{l|l} \sum_s V_S \Phi_S^{3\mathrm{D}}(\mathbf{r}) & \text{interstitial region} \\ \sum_\nu V_\nu^\alpha(r) K_\nu(\hat{\mathbf{r}}) & \text{muffin tin} \end{array} \right. \tag{2.121}$$

The interstitial potential $V_{\mathrm{int}}(\mathbf{g})$ is only correct in the interstitial region. Some appropriate supplementation as explained above is present inside the muffin tins. While this method is complete for periodic boundary conditions (like in `Fleur`) in `GFleur` the boundary conditions at the bulk interface and the behavior towards the vacuum have to be considered. Still the potential $V_{1,\mathbf{g}}$ taken from the Fourier transformed of the pseudocharge (2.117) is used.[7]

$$V_{1,\mathbf{g}} \quad = \quad 4\pi \frac{\tilde{\rho}(\mathbf{g})}{\mathbf{g}^2} \;, \text{ for } \mathbf{g} \neq 0 \tag{2.122}$$

The potential $V_{1,\mathbf{g}}$ is periodic in $\tilde{D}$. In figure 2.8 the lateral averaged interstitial potential is plotted for a system of 4 layers of Ag on a Pt substrate. The red line represents the

[7] $V_{1,\mathbf{g}} = V_{\mathrm{int}}(\mathbf{g})$, renamed because the potential will be used also inside the muffin-tin spheres.

potential resulting from the `Fleur` supercell calculation. $V_1(\mathbf{r})$ is given by green dots. It can be seen that the green curve is periodic in $\tilde{D}$ but the slope of the potential is wrong. To get the correct physical behavior additionally the homogeneous solution $\Delta V_{\text{corr}}(\mathbf{r}) = 0$ fulfilling the boundary condition $\partial_n V(\mathbf{r}_{\text{vac}}) = 0$ towards the vacuum has to be taken into account. Furthermore the condition $V_{\text{corr}}(\mathbf{r}_0) = V_{\text{bulk}}(\mathbf{r}_0)$ at the bulk interface $\mathbf{r}_0$ has to be fulfilled. The former boundary condition is given by a zero normal derivative of the potential towards the vacuum (only for surface calculation).

$$0 = \partial_n V_1(\mathbf{r}_{\text{vac}}) + \partial_n V_{\text{corr}}(\mathbf{r}_{\text{vac}}), \tag{2.123}$$

because the potential is given by the sum of the solutions

$$V(\mathbf{r}) = V_1(\mathbf{r}) + V_{\text{corr}}(\mathbf{r}). \tag{2.124}$$

The blue dots in the figure represent the corrected potential $V(\mathbf{r})$ where the vacuum boundary condition is applied. There are three blue curves because the system was calculated within three self-consistent loops. Each blue curve represents the result of a $V(\mathbf{r})$ calculation. While the first two curves are giving a too large workfunction the potential of the third round is converging towards the bulk potential. In order to fulfill $\Delta V_{\text{corr}}(\mathbf{r}) = 0$ we get a linear equation $V_{\text{corr}}(z) = a + bz$ in z direction normal to the surface in case of $\mathbf{g}_{\parallel} = 0$. Thus the slope of the potential can be corrected to get $\partial_n V_{\text{corr}}(\mathbf{r}_{\text{vac}}) = -\partial_n V_1(\mathbf{r}_{\text{vac}})$. Since we expect an exponential behavior of the potential $V_1(\mathbf{r}_{\text{vac}})$ from the surface to the vacuum an exponential fit can be used. By taking 4 values close to the D boundary a function $f(x) = ae^{\kappa x} + bx + c$ can be fitted. The value for the slope is given by

$$b = -\frac{x_1x_3 - x_4x_1 + x_4x_2 - x_2^2 - x_3^2 + x_2x_3}{3x_3 - x_4 - 3x_2 + x_1}. \tag{2.125}$$

Otherwise the slope can also be calculated by a linear regression through the last points towards the vacuum region. By this proceeding small periodic changes in the potential values due to the Fourier transformation are corrected, whereas the exponential fit can not correct this. The disadvantage is that a flat potential behavior in the vacuum region is needed. From the least square method $min(v = \sum_{i=1}^{n}(y_i - f(x_i))^2)$ equivalent to $\frac{\partial}{\partial b}v = 0$ and $\frac{\partial}{\partial a}v = 0$, we get with the linear function $f(x) = a + bx$ for the linear regression:

$$b = \frac{n\sum x_iy_i - \sum x_i \sum y_i}{n\sum x_i^2 - (\sum x_i)^2} \tag{2.126}$$

$$a = \frac{\sum x_i^2 \sum y_i - \sum x_iy_i \sum x_i}{n\sum x_i^2 - (\sum x_i)^2} \tag{2.127}$$

And for the standard derivative of y values, a value and slope we get

$$\sigma_y = \sqrt{\frac{\sum_{i=1}^{n}(y_i - f(x_i))^2}{n-2}} \tag{2.128}$$

$$\sigma_m = \sigma_y\sqrt{\frac{n}{n\sum x_i^2 - (\sum x_i)^2}} \tag{2.129}$$

$$\sigma_a = \sigma_y\sqrt{\frac{\sum x_i^2}{n\sum x_i^2 - (\sum x_i)^2}}. \tag{2.130}$$

The method of linear regression is tested but the convergence of the results become worse if applied in self-consistent calculations. Therefore the exponential fitting method will be used throughout the work.

2.6.3 Calculate the Embedded Green Function

The embedded Green function (2.104) can be calculated by the following inverted matrix equation for each $\mathbf{k}_\parallel$ in the two dimensional Brillouin zone and each energy E.

$$G^{\mathbf{gg'}}_{\mathbf{k}_\parallel,E}[n] = \left[ES^{\mathbf{gg'}}_{\mathbf{k}_\parallel,E}[n] - H^{\mathbf{gg'}}_{\mathbf{k}_\parallel,E}[n] - \Sigma^{\mathbf{gg'}}_{\mathbf{k}_\parallel,E}\right]^{-1} \tag{2.131}$$

The elements of the overlap matrix $\hat{\mathbf{S}}$ and the Kohn-Sham Hamiltonian matrix $\hat{\mathbf{H}}$ are given by:

$$\begin{aligned}
S^{\mathbf{gg'}}_{\mathbf{k}} &= <\text{LAPW}|\text{LAPW}'>_{\text{int}} = \int_{\text{int}} \phi_{\mathbf{k},\mathbf{g}}(\mathbf{r})\phi_{\mathbf{k},\mathbf{g}'}(\mathbf{r})d\mathbf{r} && (2.132)\\
&= \int_{\text{int}} e^{-\mathrm{i}(\mathbf{k}+\mathbf{g})\mathbf{r}} e^{\mathrm{i}(\mathbf{k}+\mathbf{g}')\mathbf{r}} dV = \int_V e^{-\mathrm{i}(\mathbf{k}+\mathbf{g})\mathbf{r}} e^{\mathrm{i}(\mathbf{k}+\mathbf{g}')\mathbf{r}} \Theta_1(\mathbf{r})dV && (2.133)\\
&= \Theta_1(\mathbf{g}'-\mathbf{g}) && (2.134)\\
H^{\mathbf{gg'}}_{\mathbf{k}} &= \int_{\text{int}} \phi^*_{\mathbf{k},\mathbf{g}}(\mathbf{r}) \left(-\frac{1}{2}\nabla^2 + V(\mathbf{r}) + \delta(n-n_S)\frac{1}{2}\frac{\partial}{\partial n_S}\right)\phi_{\mathbf{k},\mathbf{g}'}(\mathbf{r})dV && (2.135)\\
&\underbrace{=}_{\textbf{Green}} \int_{\text{int}} -\frac{1}{2}\left(\nabla\phi^*_{\mathbf{k},\mathbf{g}}(\mathbf{r})\nabla\phi_{\mathbf{k},\mathbf{g}'}(\mathbf{r})\right)dV + V^{\mathbf{gg'}}_{\text{int}} && (2.136)\\
&= T^{\mathbf{gg'}} + V^{\mathbf{gg'}}_{\text{int}} && (2.137)
\end{aligned}$$

Thereby the elements of the Hamiltonian concerning the kinetic energy part can be solved.

$$\begin{aligned}
T^{\mathbf{gg'}}_{\mathbf{k}} &= \int_{\text{int}} \frac{1}{2}(\mathbf{k}+\mathbf{g})(\mathbf{k}+\mathbf{g}')e^{-\mathrm{i}(\mathbf{g}-\mathbf{g}')\mathbf{r}}dV && (2.138)\\
&= \int_V \frac{1}{2}(\mathbf{k}+\mathbf{g})(\mathbf{k}+\mathbf{g}')\Theta_1(\mathbf{r})e^{-\mathrm{i}(\mathbf{g}-\mathbf{g}')\mathbf{r}}dV && (2.139)\\
&= \frac{(\mathbf{k}+\mathbf{g})(\mathbf{k}+\mathbf{g}')}{2}\Theta_1(\mathbf{g}'-\mathbf{g}) && (2.140)
\end{aligned}$$

In the equations only the interstitial part is considered. The muffin-tin part is a **r**-integration over the muffin-tin sphere and is therefore not treated differently than in the `Fleur` code. Thus the muffin-tin part was omitted for simplicity. The muffin-tin part is extensively treated in the PhD thesis by P. Kurz [63]. The stepfunction $\Theta_1(\mathbf{r})$ cuts out the muffin tins and is shown in figure 2.11.
The outer muffin tins can be neglected and therefore the interstitial region looks rather simple (figure 2.9). This stepfunction $\Theta_1(\mathbf{r})$ can be treated analytically. The potential is not considered yet. The potential in the delta region is set to zero. In order to describe the somehow more complicated interstitial region (figure 2.10) three stepfunctions (figures 2.11, 2.12 and 2.13) have to be used.

$$V^{\mathbf{gg'}}_{\text{int}} = \int_V e^{-\mathrm{i}\mathbf{gr}} V_{\text{int}}(\mathbf{r}) \underbrace{\Theta_1(\mathbf{r})\Theta_2(\mathbf{r})\Theta_3(\mathbf{r})}_{\Theta(\mathbf{r})} e^{\mathrm{i}\mathbf{g'r}}dV \tag{2.141}$$

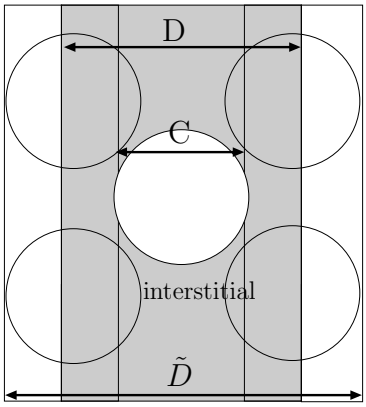

Figure 2.9: The int. region for T and S is shaded in the picture.

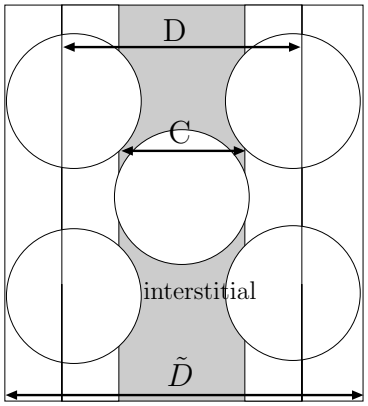

Figure 2.10: The interstitial region for V is shaded in the picture.

The potential V_{int} is given in reciprocal space as showed in section 2.6.2. But it is only correct in the interstitial region whereas inside the muffin tins an appropriate substitution was made. Therefore the correct interstitial potential has to be cut out of this interstitial representation. Since the interstitial part of the potential is more complicated than the one of the overlap matrix or kinetic energy part respectively, the potential has to be calculated in three steps.

$$\begin{array}{ccc} V_{\text{int}}(\mathbf{g}) & & \tilde{V}_{\text{int}}(\mathbf{g}) \\ \downarrow \text{FT} & & \uparrow \text{FT} \\ V(\mathbf{r}) & \underbrace{\longrightarrow}_{\Theta(\mathbf{r})} & V(\mathbf{r})\Theta(\mathbf{r}) \end{array} \tag{2.142}$$

The stepfunction $\Theta(\mathbf{r})$ is given in real space whereas for the overlap matrix $\hat{\mathbf{S}}$ and the kinetic part of the Hamiltonian a stepfunction $\Theta_1(\mathbf{g}' - \mathbf{g})$ in reciprocal space is applied. The last term needed in equation (2.131) is the matrix of the embedding potential. We

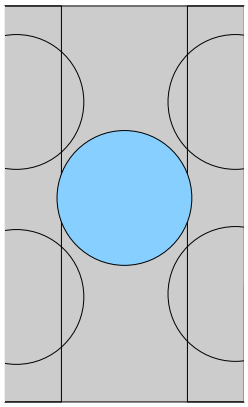

Figure 2.11: Θ_1

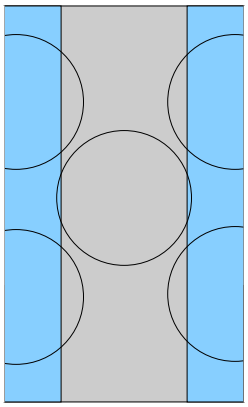

Figure 2.12: Θ_2

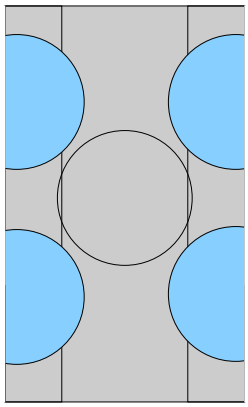

Figure 2.13: Θ_3

can write the the matrix elements of the embedding potential as

$$\Sigma^{\mathbf{g}\mathbf{g}'}_{\mathbf{k}_\parallel,E} = \sum_{S=L,R} \int_{\text{int}} \phi_{\mathbf{k},\mathbf{g}}(\mathbf{r})^* \delta(n-n_S)\delta(n'-n_S)\Sigma_{\mathbf{k}_\parallel,E}(\mathbf{r},\mathbf{r}')\phi_{\mathbf{k},\mathbf{g}'}(\mathbf{r}')d\mathbf{r}d\mathbf{r}'. \quad (2.143)$$

If we express the embedding potential in the two dimensional basis set (2.115)

$$\Sigma_{\mathbf{k}_\parallel,E}(\mathbf{r}_\parallel,\mathbf{r}'_\parallel) = \frac{1}{V}\sum_{\mathbf{g}_\parallel,\mathbf{g}\parallel'} e^{\mathrm{i}\mathbf{g}_\parallel\mathbf{r}_\parallel}\Sigma_{\mathbf{k}_\parallel,E}(\mathbf{g}_\parallel,\mathbf{g}'_\parallel)e^{-\mathrm{i}\mathbf{g}'_\parallel\mathbf{r}'_\parallel}, \quad (2.144)$$

equation (2.143) can be rewritten:

$$\begin{aligned}\Sigma^{\mathbf{g}\mathbf{g}'}_{\mathbf{k}_\parallel,E} &= \sum_{S=L,R}\int_{\text{int}} e^{-\mathrm{i}(\mathbf{k}_\parallel+\mathbf{g}_\parallel)\mathbf{r}_\parallel}e^{-\mathrm{i}g_\perp z_S}\delta(n-n_S)\delta(n'-n_S)\Sigma_{\mathbf{k}_\parallel,E}(\mathbf{r},\mathbf{r}')e^{\mathrm{i}(\mathbf{k}_\parallel+\mathbf{g}'_\parallel)\mathbf{r}'_\parallel}e^{\mathrm{i}g'_\perp z_S}d\mathbf{r}d\mathbf{r}' \\ &= \frac{1}{V}\left[e^{-\mathrm{i}g_\perp z_L}e^{\mathrm{i}g'_\perp z_L}\Sigma_{\mathbf{k}_\parallel,E}(\mathbf{g}_\parallel,\mathbf{g}'_\parallel) + e^{-\mathrm{i}g_\perp z_R}e^{\mathrm{i}g'_\perp z_R}\Sigma_{\mathbf{k}_\parallel,E}(\mathbf{g}_\parallel,\mathbf{g}'_\parallel)\right] \quad (2.145)\end{aligned}$$

The matrix is complex even in the case of real Hamiltonian and overlap matrices. But $\Sigma^{\mathbf{g}\mathbf{g}'}_{\mathbf{k}_\parallel,E}$ is also block diagonal in the three dimensional basis. All two dimensional quantities like the embedding potential and $\hat{\mathbf{T}}$ matrix[8] are handled in the two dimensional basis. The three-dimensional Green function can be projected onto the two dimensions parallel to the interface by

$$G_{b,b'}(\mathbf{g}_\parallel,\mathbf{g}'_\parallel) = \frac{1}{V'}\sum_{g_\perp,g'_\perp} e^{\mathrm{i}g_\perp z_b}G(\mathbf{g},\mathbf{g}')e^{-\mathrm{i}g'_\perp z_{b'}}. \quad (2.146)$$

2.6.4 Calculate the Embedding Potential

The embedding potential Σ was introduced to substitute the normal derivatives of the outer region wavefunctions ψ in the extended Kohn-Sham equation of the embedded region by a generalized logarithmic derivative $\Sigma = \frac{1}{2}\frac{\partial_n\psi}{\psi}$. Thus the embedding potential gives on the one side the bulk on the other interface the vacuum 'boundary conditions' to the system for a given energy E and a reciprocal vector $\mathbf{k}$. A transfer matrix $\hat{\mathbf{T}}$ has to be introduced in order to calculate the embedding potential. It will be shown that in an appropriately chosen embedding region the eigenvalues of the transfer matrix are equal to the eigenvalues of the translation operator $T_{\mathbf{R}}$. Applying the Bloch theorem we get a generalized bandstructure with real and complex $\mathbf{k}$-vectors. Finally the embedding potential can be calculated from the eigenvectors of the transfer matrix [117].

Transfer Matrix

The transfer matrix maps the value and the derivative of the wavefunction on one side of the embedded region to the other side.

$$\Psi_R = \begin{pmatrix} \psi_R \\ \partial_n\psi_R \end{pmatrix} = \hat{\mathbf{T}}\begin{pmatrix} \psi_L \\ \partial_n\psi_L \end{pmatrix} \quad (2.147)$$

[8]The transfer matrix $\hat{\mathbf{T}}$ will be introduced in the following section.

Since the transfer matrix describes the propagation of wavefunctions through the embedded region it can be expressed by the Green function at the boundaries. Generally the $\hat{\mathbf{T}}$ matrix can be related to the Green function by the Green theorem

$$\psi(\mathbf{r}) \;\; = \;\; = -\frac{1}{2}\int_{S_L+S_R}[G(\mathbf{r},\mathbf{r}_b)\partial_n\psi(\mathbf{r}_b) - \partial_n G(\mathbf{r},\mathbf{r}_b)\psi(\mathbf{r}_b)]d^2\mathbf{r} \tag{2.148}$$

giving a linear relation between ψ and $\partial\psi$ at the boundaries. We use von-Neumann boundary conditions $\partial_n G(\mathbf{r},\mathbf{r}_b) = 0$. Note that in this derivation we tread normal derivatives with different signs. In the Green theorem the direction outwards of the embedded region Ω is assumed. Though for the transfer matrix $\hat{\mathbf{T}}$ in z direction the signs of $\partial_n\Psi_R$ do not differ leading to

$$\hat{\mathbf{T}} \;\; = \;\; \begin{pmatrix} G_{RR}G_{LR}^{-1} & -\frac{1}{2}G_{RL} + \frac{1}{2}G_{RR}G_{LR}^{-1}G_{LL} \\ G_{LR}^{-1} & G_{LR}^{-1}G_{LL} \end{pmatrix}. \tag{2.149}$$

Complex Bandstructure

The concept of a complex bandstructure of the solid was already introduced in chapter 2.5 but should be repeated here for a better understanding how the embedding potential will be calculated within the `GFleur` program. It can be shown that the translation operator $T_{\mathbf{R}}f(\mathbf{r}) = f(\mathbf{r}+\mathbf{R})$ commutates with the Hamiltonian. Thus the Bloch theorem (for an infinite crystal) holds that the eigenfunctions of the Hamiltonian can be chosen such that they are also eigenfunctions of $T_{\mathbf{R}}$. The Bloch theorem states that the wavefunctions of the system are of the Bloch type

$$\psi_{n,\mathbf{k}}(\mathbf{r}) \;\; = \;\; e^{\mathbf{ikr}}u_{n,\mathbf{k}}(\mathbf{r}) \tag{2.150}$$

with $u_{n,\mathbf{k}}(\mathbf{r}) = u_{n,\mathbf{k}}(\mathbf{r}+\mathbf{R})\ \forall$ vectors $\mathbf{R}$ of the Bravais lattice. The Bloch wave is a planewave modulated by a lattice periodic function $u_{n,\mathbf{k}}(\mathbf{r})$. It can also be expressed by

$$\psi(\mathbf{r}+\mathbf{R}) \;\; = \;\; e^{\mathbf{ikR}}\psi(\mathbf{r}). \tag{2.151}$$

This follows directly from (2.150). The eigenvalues of the translation operators $T_{\mathbf{R}}$ are

$$T_{\mathbf{R}}\psi(\mathbf{r}) \;\; = \;\; \psi(\mathbf{r}+\mathbf{R}) \underbrace{=}_{(2.151)} e^{\mathbf{ikR}}\psi(\mathbf{r}) \tag{2.152}$$

$$\Rightarrow \lambda \;\; = \;\; e^{\mathbf{ikR}}. \tag{2.153}$$

If the embedding region is chosen to be a principle layer of the system the transfer matrix $\hat{\mathbf{T}}$ and the translation matrix $\hat{\mathbf{T}}_{\mathbf{R}}$ are equal. We get the so-called **generalized Bloch condition**

$$\Psi_R \;\; = \;\; \begin{pmatrix} \psi(\mathbf{r}_L+\mathbf{R}) \\ \partial_n\psi(\mathbf{r}_L+\mathbf{R}) \end{pmatrix} = \hat{\mathbf{T}}_{\mathbf{R}}\Psi_L = \lambda\Psi_L \tag{2.154}$$

and therefore with (2.147)

$$\hat{\mathbf{T}}\Psi_L = \lambda\Psi_L. \tag{2.155}$$

As the solutions of the Schrödinger equation should be normalizable the Bloch vectors $\mathbf{k}$ are chosen to be real in bulk crystals. Still complex solutions are also possible. A complex Bloch vector would lead to an exponential growth in some direction. In case of surfaces this exponentially growing or decaying solutions are important and are called evanescent states. If complex Bloch vectors are treated the well known bandstructure $E(\mathbf{k})$ has to be extended to a generalized bandstructure $\epsilon(\mathbf{k}')$ with $\epsilon,\mathbf{k}' \in \mathbb{C}$. The term **complex bandstructure** is used for the so called 'real lines' of this bandstructure. Real energies together with real or complex Bloch vector are building these lines.

In standard electronic structure calculations the $\mathbf{k}$-points determining λ are given and the energy eigenvalues of the Hamiltonian ($H\psi = E\psi$) are calculated in accordance with $T_{\mathbf{R}}\psi = \lambda\psi$. In `GFleur` a set of energies gives the $\hat{\mathbf{T}}$ matrix which is used in equation (2.154) leading to $\lambda(E)$. Since the observed system has two-dimensional symmetry a set of $\mathbf{k}_\parallel$ is given for the startup. The perpendicular component $k_z(\mathbf{k}_\parallel, E)$ is calculated.

Calculate the Embedding potential from the $\hat{\mathbf{T}}$ matrix

In the last step we have to solve (2.155) for its eigenvalue $\lambda(E)$ leading to the CBS and its eigenvectors $(\partial_n\psi, \psi)^T$. From the latter the embedding potential can be derived by equation (2.101). Now let us summarize the chapter in a simplified flow chart for a better understanding of the procedure of finding the embedding potential. Starting

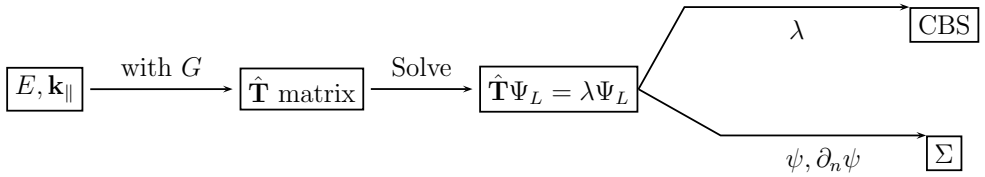

Figure 2.14: Schematic flowchart explaining how the embedding potential Σ is calculated.

with a set of energies E and Bloch vectors $\mathbf{k}_\parallel$ parallel to the interface the transfer matrix $\hat{\mathbf{T}}$ can be calculated. Therefore equation (2.149) can be used. In the last step the generalized Bloch condition (2.155) has to be solved. The eigenvalues $\lambda(E)$ are constituting the complex bandstructure and the eigenvectors ψ and $\partial_n\psi$ construct the embedding potential by solving equation (2.101).

2.6.5 Vacuum Embedding Potential

The embedding potential towards the vacuum has to be calculated in a different way than the bulk one. Using the CBS in order to construct the embedding potential is obviously not possible. Instead the wavefunction towards the vacuum can be calculated easily from the Schödinger equation of a free electron moving in the constant vacuum potential. However due to the computational setup the calculation of the vacuum embedding potential becomes a little tricky.

Move the Embedding Potential Plane

Within the calculation of the embedding potential towards the vacuum side it is necessary to consider the delta region. The delta region has to be introduced because the embedding plane cannot cut through the muffin-tin spheres in order to get a planar interface. Even though no muffin tins are present in the vacuum region, due to the periodicity of $\tilde{D}$ a delta region in the vacuum is present. On both sides the difference between $D/2$ and $C/2$ determines the size of the delta region and inside this region the potential is set to a constant value. Within the `GFleur` code the potential inside the delta region is set to zero. In practice we calculate the embedding potential at position $C/2$ and move it through the region of constant potential to the embedding potential at position $D/2$. Since the embedding potential Σ is given by the generalized logarithmic derivative we have to move the wavefunction and its first derivative through the region in order to get the correct embedding potential at the final position. In general for given boundary conditions for the left side ψ and ψ' we can calculate the modified wavefunction to the right side. The solution of the Schrödinger equation with V=0 is given by

$$\psi_R(z) = c_+ e^{\mathrm{i}\kappa_R z} + c_- e^{-\mathrm{i}\kappa_R z}, \tag{2.156}$$

where κ_R is $\sqrt{2E - (\mathbf{k}_\parallel + \mathbf{g}_\parallel)^2}$. We set

$$\psi(0) = c_+ + c_- \quad \wedge \quad \psi'(0) = \mathrm{i}\kappa_R(c_+ - c_-) \tag{2.157}$$

for the boundary conditions at the left side and solve for the coefficients of (2.156):

$$c_+ = \psi - c_- \quad \wedge \quad \frac{\psi'}{\mathrm{i}\kappa_R} = \psi - 2c_- \Leftrightarrow c_- = \frac{1}{2}(\psi - \frac{\psi'}{\mathrm{i}\kappa_R}) \tag{2.158}$$

We can solve now for the second coefficient and get

$$c_+ = \frac{1}{2}(\psi + \frac{\psi'}{\mathrm{i}\kappa_R}) \quad \wedge \quad c_- = \frac{1}{2}(\psi - \frac{\psi'}{\mathrm{i}\kappa_R}). \tag{2.159}$$

The first derivative of the wavefunction is needed.

$$\psi'_R = \mathrm{i}\kappa_R c_+ e^{\mathrm{i}\kappa_R z} - \mathrm{i}\kappa_R c_- e^{-\mathrm{i}\kappa_R z} \tag{2.160}$$

$$= \frac{\mathrm{i}\kappa_R}{2}\left((\psi + \frac{\psi'}{\mathrm{i}\kappa_R})e^{\mathrm{i}\kappa_R z} - (\psi - \frac{\psi'}{\mathrm{i}\kappa_R})e^{-\mathrm{i}\kappa_R z}\right) \tag{2.161}$$

Now the embedding potential can be calculated.

$$\Sigma = \frac{1}{2}\frac{\psi'}{\psi} = \frac{\mathrm{i}\kappa_R}{2}\frac{(\psi + \frac{\psi'}{\mathrm{i}\kappa_R})e^{\mathrm{i}\kappa_R z} - (\psi - \frac{\psi'}{\mathrm{i}\kappa_R})e^{-\mathrm{i}\kappa_R z}}{(\psi + \frac{\psi'}{\mathrm{i}\kappa_R})e^{\mathrm{i}\kappa_R z} + (\psi - \frac{\psi'}{\mathrm{i}\kappa_R})e^{-\mathrm{i}\kappa_R z}} \tag{2.162}$$

Finally we get

$$\Sigma_{LR}(z) = \frac{\mathrm{i}\kappa_R}{2}\left[\frac{\frac{\psi'}{\mathrm{i}\kappa_R}cos(\kappa_R z) + \mathrm{i}\psi sin(\kappa_R z)}{\psi cos(\kappa_R z) + \mathrm{i}\frac{\psi'}{\mathrm{i}\kappa_R}sin(\kappa_R z)}\right], \tag{2.163}$$

describing the embedding potential moved by z from the left to the right side in terms of the left side wavefunction ψ and its derivative ψ'.
Another way of solving the problem is to investigate the transfer matrix $\hat{\mathbf{T}}$ as was done in section 2.6.4.

Analytic Vacuum Embedding Potential

A constant potential $V = V_0$ is assumed in the vacuum. In order to use the correct embedding potential towards the vacuum we have to take care of the delta region. As explained we need the value of the wavefunction and its first derivative at the left position. In `GFleur` this is at position $C/2$. The solving wavefunction of the Schrödinger equation for the constant vacuum potential $V = V_0$ propagating to the right side can easily be found to

$$\psi(z) = e^{\mathrm{i}\kappa_L z} \tag{2.164}$$

with $\kappa_L = \sqrt{2(E - V_0) - (\mathbf{k}_\parallel + \mathbf{g}_\parallel)^2}$. The boundary conditions at the left side can be set to

$$\psi(0) = 1 \quad \wedge \quad \psi'(0) = \mathrm{i}\kappa_L, \tag{2.165}$$

if $C/2$ is moved to $z = 0$. However within the program the planar embedding plane is located at $D/2$ and thus we have to move from $C/2 = 0$ to $D/2$ by $\Delta D = z$. This can be done by applying the derived equation (2.163). Thus the embedding potential at $D/2$ is given by

$$\Sigma \;=\; \frac{\mathrm{i}\kappa_R}{2}\left[\frac{\kappa_L cos(\kappa_R z) + \mathrm{i}\kappa_R sin(\kappa_R z)}{\kappa_R cos(\kappa_R z) + \mathrm{i}\kappa_L sin(\kappa_R z)}\right]. \tag{2.166}$$

We can also calculate Σ by applying the transfer matrix (2.149). To do so we have to calculate the necessary Green functions (G_{LL},.. and so on). This can be done and the results are taken from equation (6.20)[116]. There they are given by

$$G_{LL}(\mathbf{g}_\parallel \mathbf{g}'_\parallel) = G_{RR}(\mathbf{g}_\parallel \mathbf{g}'_\parallel) \;=\; \delta(\mathbf{g}_\parallel, \mathbf{g}'_\parallel)\frac{2}{k} cot(kd_\parallel) \tag{2.167}$$

$$G_{RL}(\mathbf{g}_\parallel \mathbf{g}'_\parallel) = G_{LR}(\mathbf{g}_\parallel \mathbf{g}'_\parallel) \;=\; \delta(\mathbf{g}_\parallel, \mathbf{g}'_\parallel)\frac{2}{k}\frac{1}{sin(kd_\parallel)}. \tag{2.168}$$

Substituting these expressions into (2.149) leads to (2.166).

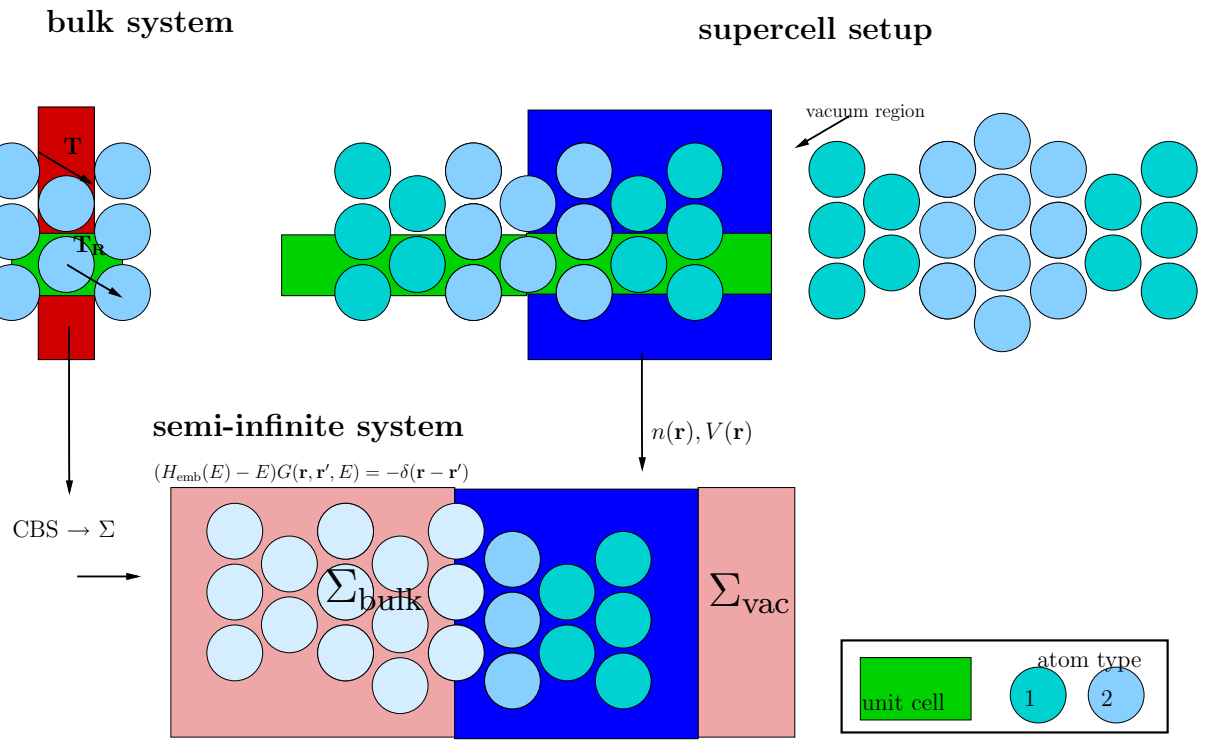

Figure 2.15: Computational method of calculating semi-infinte surface systems with the Green function embedding technique.

2.7 Summary of the Computational Method

The detailed picture of the the computational procedure given so far will be dropped in favor of giving a better overview of the method.
In order to calculate a surface with infinite leads from *ab initio* density functional theory the method of Green function embedding can be used. In a first step from the self-consistent charge density of a bulk system the embedding potential can be calculated for different surface orientations. In a second step the electronic structure of a supercell is calculated. A region of the supercell is then cut and used for the embedding region within the Green function embedding scheme. The left border of the embedding region will be attached to the infinite lead through the embedding potential calculated before. The right border is built by a vacuum region. There the embedding potential can be calculated analytically. In the two dimensional interface area the system is translational invariant and infinite. This computational setup is sketched in figure 2.15. In a third step the embedded Green function can be calculated from the embedding region bordered by the two embedding potentials within a self-consistency cycle. Thereby the Coulomb potential is gained from the charge density via the Poisson equation. Two boundary conditions are needed to solve the equation completely. On the left side boundary the value of the bulk potential is used and on the vacuum side the slope towards the vacuum is set to zero. The self-consistency cycle can be used because the charge density is obtained from the embedded Green function and because the embedded Green function itself depends on the charge density.
If an electric field should be applied to the surface region we can implement this in our

method by changing the boundary condition for the Coulomb potential and the embedding potential of the vacuum region. The slope of the potential towards the vacuum is set to the slope introduced by a constant electric field. The correct physical behavior of the potential results.
In the next chapter this computational scheme will be extended to treat image potential states. In front of metal surfaces the potential decays like $1/z$, due to the screening charge induced. The potential in the surface region obtained from the DFT calculation employing the common approximations LDA or GGA is not correctly reproducing the expected $1/z$ behavior. Instead the potential decays exponentially towards the vacuum. In order to investigate the image potential states, which are a direct result of the $1/z$ decay, the potential has to be modified. The vacuum embedding potential is now calculated numerically by solving the Schrödinger equation on a discrete grid using the Numerov algorithm for a model potential (with or without electric field) with the parameter z_{I} representing the image plane. In order to avoid an discontinuous gradient of the potential curve the modeled image potential is mixed with the Coulomb potential. The mixing region and mixing function is entering our calculations as a second parameter.

3 Localized States

In this work localized states in front of transition metal surfaces are investigated. In the first step the well known phenomenon of surface states is explained in section 3.1. Then image potential induced states are treated in section 3.2. These states are located close to the vacuum energy and can be measured by a variety of experimental techniques (section: 3.2.1). Usual DFT approaches fail to constructed the image potential states and our method to implement them nevertheless is introduced (section: 3.2.3). How the image potential states react if an electric field is applied will be shown in section 3.3. Our method can be extended to allow calculations of surfaces in an electric field. By this the calculation of image potential induced field states become feasible and the implementation into the embedding method will be shown in section 3.3.1.

3.1 Surface States

At the surface the electronic structure changes enormously compared to the bulk one. The broken 3-dimensional symmetry gives rise to electronic states where the wavefunction is concentrated at the surface of the crystal. To be more precise, the periodicity of the wavefunction in the z direction (normal to the surface) is no longer required in case of an interface. The different boundary conditions for the wavefunction give rise to states which are forbidden in the bulk. Depending on their physical origin these states can be divided into crystal or barrier derived surface states.
The former are named Tamm states [106]. This kind of surface states is split off by the surface potential into a band gap of the bulk bands. Tamm showed that these solutions are possible in a modified Kronig and Penney [61] potential. (E.g. on silver (100) at the $\overline{M}$ point of the two dimensional Brillouin zone a Tamm surface state split of from the d-bands.)
The barrier derived surface state is called Shockley surface state [95]. They appear in a projected energy gap of the bulk bands, due to the termination of the infinite crystal. Shockley observed a periodic potential with variable inter-atomic spacing a. For large spacing no surface state exists and the energy bands look like free electron bands. For small a bands arise in the band structure and for even smaller a two discrete states split off from the band. The term 'surface resonance' is used for surface states leaking into the substrate. The concept of complex band structures explained in section 2.5 is useful for the treatment of surface states, because finding surface states can be regarded as the problem of matching wavefunctions outside the surface to those inside the bulk crystal. The latter are called evanescent waves. If the Bloch theorem is extended to the complex $\mathbf{k}$-vectors these evanescent waves result. Thus it is clear that surface states exist most of the time in band gaps joint by loops of real lines with complex $\mathbf{k}$. There the evanescent waves needed for matching can be found [43]. Additionally surface states can exist at

all energies due to matching to one of the real lines running to infinity as mentioned in [42].

3.2 Image Potential States

Beside the crystal induced surface states, namely Shockley and Tamm states, there can be image potential induced surface states in metals.
If an electron is placed at position z in front of a metallic surface an electric charge is induced into the metal. The induced charged is positive and screens the outer negative charge. From the Maxwell equations it follows that the electric field has to be perpendicular to the metal surface at the interface.

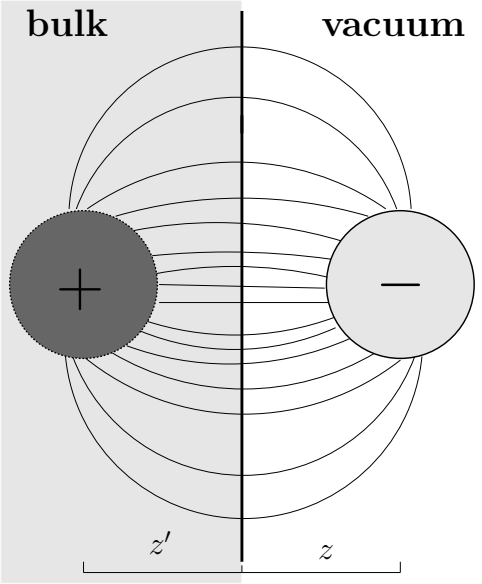

Figure 3.1: Construction of the image potential.

In order to construct the electric field outside the bulk usually an image charge of opposite sign is placed inside the bulk at a distance z' equal to $-z$. The distance between the charge outside and its image charge inside the bulk is two times the distance between the surface and the outer charge position, thus $2z$. This is shown in figure 3.1. Note that the electric field inside the bulk is not the correct physical one but it is used just for construction purpose. If we now apply the law of Coulomb force to the setup of two electric charges of different sign placed in a distance of $2z$ the potential outside the bulk can be given by (3.5) in the one dimensional picture. This is the so called image potential. The potential decays $1/z$ like towards the constant vacuum potential V_{vac}. This behavior is characteristic for the image potential.

Coulomb force and potential

$$\mathbf{F} = \frac{1}{4\pi\epsilon_0} q_1 q_2 \frac{\mathbf{x}_1 - \mathbf{x}_2}{|\mathbf{x}_1 - \mathbf{x}_2|^3} \tag{3.1}$$

$$\mathbf{F} = -\nabla V \tag{3.2}$$

1D image potential

$$\mathbf{F} = \frac{1}{4\pi\epsilon_0}(-e^2)\frac{z+z}{|z+z|^3} \tag{3.3}$$

$$= -\frac{e^2}{4\pi\epsilon_0}\frac{1}{4z^2} \tag{3.4}$$

$$\Rightarrow V = V_{\text{vac}} - \frac{e^2}{4\pi\epsilon_0}\frac{1}{4z} \tag{3.5}$$

In the simplest model system an infinitely high potential wall could be placed at the interface forcing an electron to rebound from the surface. An electron with energy below the vacuum energy is now trapped inside a potential well formed by the infinite

potential wall towards the bulk and the $1/z$ decaying potential towards the vacuum side. The eigenenergies of the electron can be calculated by solving the one dimensional Schrödinger equation.

$$\left(-\frac{\hbar^2}{2m}\frac{\partial^2}{\partial z^2}+V\right)\psi(z) = E\psi(z) \tag{3.6}$$

$$\underbrace{\Rightarrow}_{(3.5)}\left(-\frac{\hbar^2}{2m}\frac{\partial^2}{\partial z^2}-\frac{e^2}{4\pi\epsilon_0}\frac{1}{4z}+V_{\text{vac}}\right)\psi(z) = E\psi(z) \tag{3.7}$$

It is the same equation as the radial part of the s-wavefunction for the hydrogen atom, except a factor of 4. Thus the eigenenergies are

$$E_n = E_{\text{vac}}-\frac{m}{32}\left(\frac{e^2}{4\pi\epsilon_0\hbar^2}\right)^2\frac{1}{n^2} \tag{3.8}$$

$$= E_{\text{vac}}-\frac{1}{16}\frac{E_{\text{Ry}}}{n^2}. \tag{3.9}$$

Whereas the length scales are stretched by a factor of 4 the energies are compressed by a factor of 16 compared to the hydrogen atom. The Rydberg energy E_{Ry} is 13.6 eV. In summary, the coulomb tail of the potential form a Rydberg series of possible electron states (3.9). This series of electronic states are called image potential states or Rydberg surface states in literature. In general they are unoccupied but they can be occupied by lifting the energy of a surface electron by an emitted photon or an electric field. But of course in this simple model the potential wall is not a good representation of the metallic surface. If for example unoccupied states of the bulk close to the vacuum level exists the outer electron would penetrate into the bulk, occupying one of the unoccupied states. Since all states above the Fermi level are unoccupied a band gape close to the vacuum level is required. A bandgap in a metal above the Fermi level is not forbidden because a metal is defined by a continuous bands across the Fermi level which is some eV below the vacuum level of the system. In this model an electron with energy below the vacuum energy is confined between the metal with a band gap close to the vacuum level and the coulomb tail of the image potential towards the vacuum. The simple model with infinite potential wall has to be extended. Since the electron is not only considered to be outside the crystal the finite probability to find the electron at the surface changes the potential depending on the band structure of the crystal. This effect is taken into account by the so called image plane z_{I} in the potential and a quantum defect a in the energy. The image plane z_{I} can be seen as an effective position of the metal surface and thus can be calculated in an electro-static picture. The parameter a was already used in one of the first theoretical papers about Rydberg states by Echenique and Pendry in 1978 [30]. They treated the states as standingwave resonances of an electron caught in a box of the semi infinite solid and the surface barrier normal to the surface. This considerations lead to the following equations:

$$V = V_{\text{vac}}-\frac{e^2}{4\pi\epsilon_0}\frac{1}{4(z-z_{\text{I}})} \tag{3.10}$$

$$E_n(a) = E_{\text{vac}}-\frac{1}{16}\frac{E_{\text{Ry}}}{(n+a)^2} \tag{3.11}$$

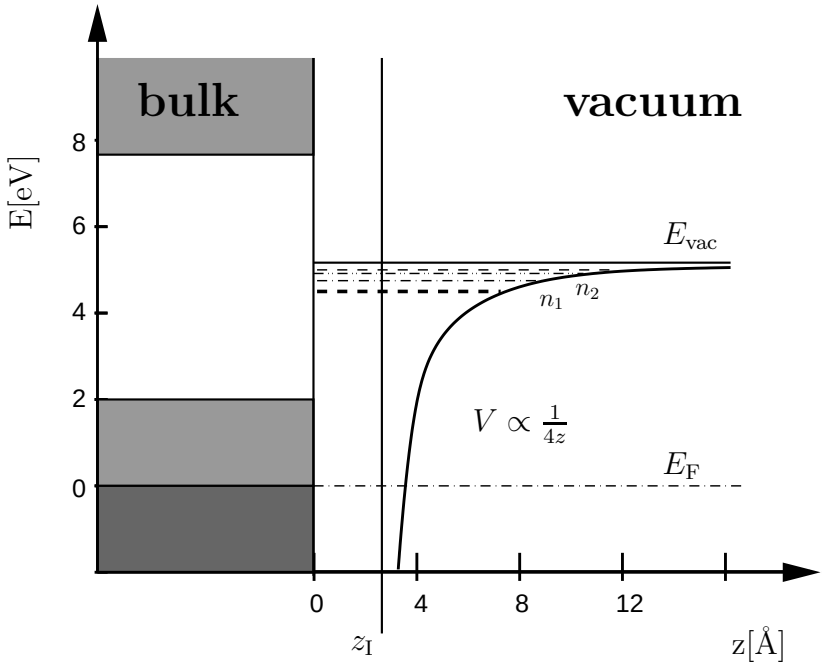

Figure 3.2: Charge in front of a metal with a bandgap close to the vacuum level. Electrons are caught in the potential well between band gap and coulomb tail of the potential towards the vacuum. Thereby hydrogen-like states, called image states, result.

According to [21] there are two different ways to calculate the image plane position z_{I} in the static case. Using a jellium model Lang and Kohn [64] showed how the image plane can be given by the center of a field-induced charge distribution. Calculations of the image plane for several metal and transition metal surfaces are done using either Goodwin's model (see [41]) of the crystal wavefunctions or by ab initio calculations [113, 53, 67].
Secondly a model potential can be constructed. The model-potential barrier is a function of several parameters including the image plane. A well known model is the JJJ-model by Jones, Jennings and Jepsen [55]. Fitted to the experimental results the image plane can be calculated [24].

Unfortunately image potential states cannot be calculated from first principle DFT calculations directly because the commonly used approximations LDA and GGA fail to produce the correct asymptotic image tail of the potential. By additionally taking into account the long range correlation effects, e.g. by GW-approximations, the image-like behavior in the vacuum can be achieved. But the computational effort to treat these correlation effects is huge [33]. In this work the DFT result for the semi-infinite bulk is calculated within the Green function embedding approach and the $1/z$ potential is modeled by adding the corresponding embedding potential to the vacuum site. A detailed description will follow in chapter 3.2.2.

Surface induced image potential states can be observed in experiments. Image potential states were first detected in experiments with metals by low-energy-electron diffrac-

tion (LEED) measurements [92] and thereafter by a variety of different techniques. The experimental approaches will be described in detail in section 3.2.1. The experiments offer a possibility to observe local changes in the workfunction by measuring the convergence of the binding energies of the Rydberg states.[1] Furthermore the binding energies provide information about the shape of the surface structure. Another interesting application arise if the image potential states are occupied. Then the image potential states form a free two dimensional electron gas nearly completely decoupled from the substrate which allows to study low dimensional electron dynamics [70].

Image Potential States of Magnetic Materials

The interaction of the image states with a ferromagnetic surface results in a lifting of the spin degeneracy of these states. This can be explained by the spin dependence of the band structure. The energy bands of ferromagnets depends on their spin magnetic mo-

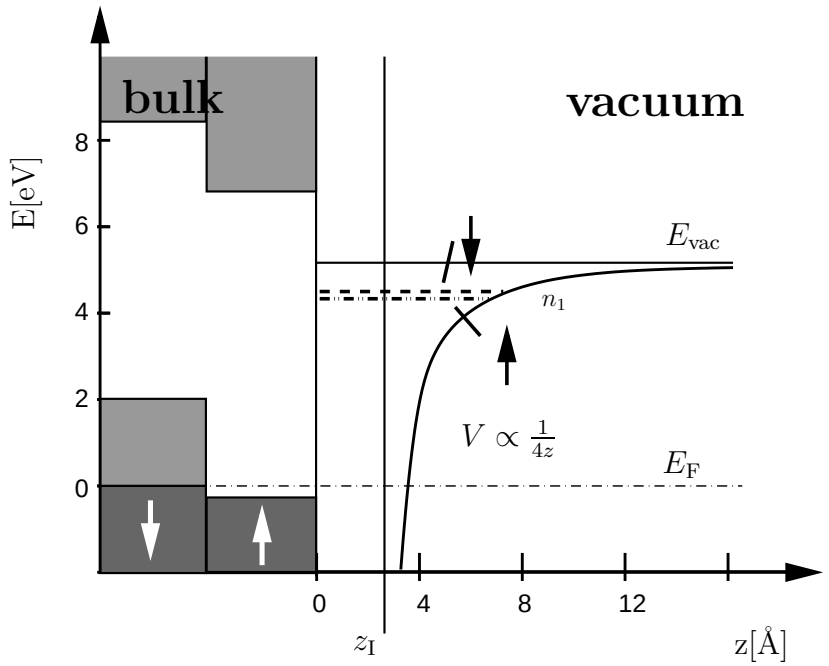

Figure 3.3: Magnetic exchange splitting of the image potential states ($n = 1$ shown), due to the spin dependent influence of the projected band of the substrate.

ment with respect to the magnetization direction. In general electrons with parallel spin magnetic moment have lower energies (majority spin) and antiparallel electrons (minory spin) have higher energies. Thus also the band gap binding the electrons in image states becomes spin dependent resulting in spin dependent image potential states. It is obvious that the spin splitting is material dependent because the splitting is determined by the band gap boundaries. If the edges of the gap are reached the splitting increases. The splitting is expected to increase from Ni to Co to Fe and this has been verified by several

[1] Contrariwise the DFT calculation has to give a correct workfunction in order to calculate the image states correctly.

experiments [82, 28]. Nekovee, Crampin and Inglesfield [71] showed that the splitting has in fact two different origins with opposite effects. The first one is bulk induced. The spin up and spin down electrons are scattered from different substrate potentials. The second contribution to the spin splitting is surface barrier induced. The surface barrier influencing the outer electrons is also spin dependent due to exchange interaction. The bulk induced effect is dominant. The surface-barrier contribution is smaller and has a sign opposite to the substrate contribution.

3.2.1 Experimental Approach to Image Potential States

While photoemission dominates the field of occupied states there are several comparable techniques available to investigate unoccupied states. These techniques are inverse photoemission (IPE) [102] , two-photon photoemission (2PPE) [34, 28] , time resolved photoemission spectroscopy [115] , bremsstrahlung isochromat spectroscopy (BIS) [4] , X-ray absorption [36] and electron energy loss spectroscopy [1]. Additionally image potential states can be observed with (spin-resolved) scanning tunneling microscopy (STM) [10, 66, 62]. Following the spin resolved STM experiment will be closely investigated because it allows to observe the spin resolved image potential states under electric field which is comparable to the theoretical results obtained in this work. Furthermore photoemission will be explained in detail because it is at the fundament of several other methods and the concepts of IPE and 2PPE will be given because they allow to investigate image potential states with high energy resolution.

STM

The idea of the vacuum tunneling dates back to the 1960ths, when Giaever [38] and Esaki[2] and several other groups were experimentally investigating tunneling phenomena in semiconductors and superconductors. Already in 1976 the first attempt to tunnel through vacuum with a positionable tip was published by W.A. Thompson [109] from the IBM T. J. Watson Research Center in New York. This publication drew the attention of his colleagues Binnig and Rohrer at the IBM Research Division in Zürich. They submitted their first patent disclosure on STM in January 1979, started to build the first scanning tunneling microscope and published first measurements in 1982 [13, 12]. Binnig and Rohrer shared half the Nobel price four years later for 'the design of the scanning tunneling microscope'. It should be mentioned that already in 1972 a field-emission microscope named 'topograliner' was proposed by R. Young *et al.*, which had common basic principles of operating like the STM except that the tip was far away from the surface in contrast to STM and therefore field-emission was rather used than tunneling current. Binnig and Rohrer remarked in their worth-reading Nobel lecture that Young "came closer than anyone else"[11].

The physical principle is rather simple and discussed in introductory courses to quantum mechanics. Nevertheless the basic principle will be given for the sake of complete-

[2]Both awarded the Nobel price in physics 1973 'for their experimental discoveries regarding tunneling phenomena in semiconductors and superconductor' together with Josephson 'for his theoretical predictions of the properties of a supercurrent through a tunnel barrier, in particular those phenomena which are generally known as the Josephson effects'.

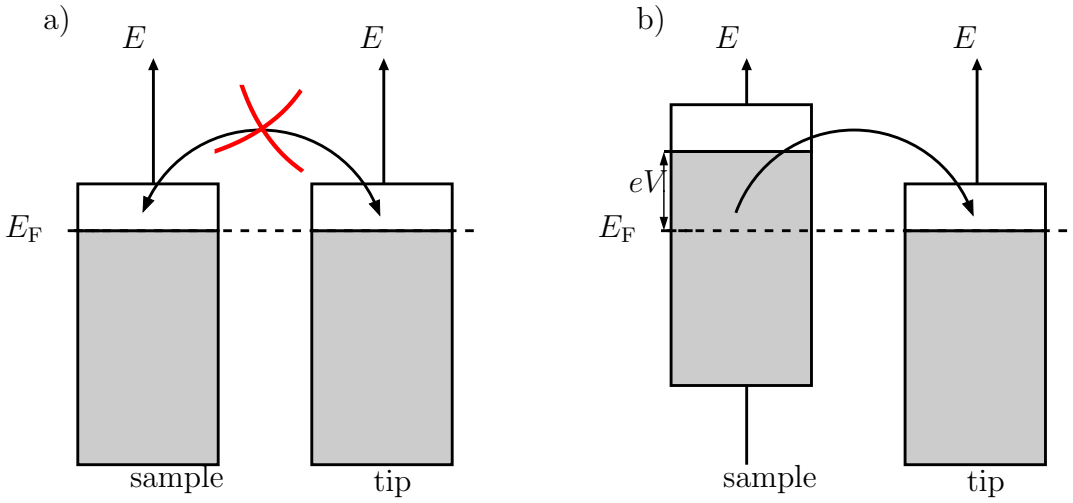

Figure 3.4: Principle of the scanning tunneling microsopy (STM). By applying an electric field, states above the Fermi level can be occupied and electrons in this states can tunnel to unoccupied states of the tip. The tunneling current depends exponentially on the tip-sample distance.

ness. Quantum mechanics allow the electron to tunnel trough barriers, whereas classical mechanics would force them to recoil. This effect can be exploited to obtain a microscope with atomic resolution. A metal tip is placed within a distance of 5 to 10 Å above a conducting sample. The vacuum region separating both builds the potential barrier. An applied bias enabled the electrons to tunnel from the tip to the sample and vice versa for a bias of opposite sign. This tunneling current is exponentially dependent on the vertical separation of the two leads. This dependency makes the high accuracy of the STM measurement feasible.

Let us assume an one dimensional model of the STM. Two metals are separated by the vacuum potential barrier. Let us further assume that both metals have the same workfunction, zero temperature resulting in a sharp Fermi edge and that no bias is applied to the system. Elastic tunneling, that is tunneling without change in energy, is not possible because both Fermi energies are equal (figure 3.4.a). Occupied energy levels of the sample do not match with unoccupied states of the tip. Now if a small bias is switched on the two Fermi levels separate. A tunneling current can flow and the value of the current can be calculated (figure 3.4.b). The wavefunction decays in z direction exponentially and is given by

$$\psi(z) = \psi(0)e^{-\kappa z} \quad \text{and} \quad \kappa = \sqrt{\frac{2m\phi}{\hbar^2}}, \tag{3.12}$$

where the decay 'constant' κ is a function of the distance between the band energy of the electron and the vacuum level. In case of small bias voltages the electrons are all close to the Fermi energy and thus their decay constant is nearly the same and can be expressed by the workfunction $\phi = E_{\text{vac}} - E_\mu$ resulting in the equation above. The probability to find a tunneled electron at the tip at distance s is given by

$$P = |\psi(z = s)|^2 \quad = \quad |\psi(0)|^2 e^{-2\kappa s}. \tag{3.13}$$

The tunneling current is proportional to the sum over all electron states E_μ, from where the electrons are able to tunnel. These states are determined by the applied bias.

$$I(s,V) \propto e^{-2\kappa s} \sum_{E_\mu = E_\mathrm{F} - eV}^{E_\mathrm{F}} |\psi_\mu(0)|^2 \tag{3.14}$$

$$= e^{-2\kappa s} \int_{E_\mathrm{F}-eV}^{E_\mathrm{F}} \sum_\mu \delta(E_\mu - E)|\psi_\mu(0)|^2 dE \tag{3.15}$$

$$= e^{-2\kappa s} \int_{E_\mathrm{F}-eV}^{E_\mathrm{F}} n(s,E) dE \tag{3.16}$$

The exponential dependence of the tunneling current from the distance allows measurements with high vertical resolution. A STM can be run in several modes allowing to investigate either the topography of the sample or to use the STM as a spectroscope. In order to get information about the topography the STM can be used either in constant distance or constant current mode. The constant distance mode is fast but it has two drawbacks. First the surface does not have to be planar and therefore can have a slope or the tip moves uncontrolled horizontal during the run. Secondly a rapid changing surface might result in a tip crashing onto the sample destroying the STM tip[3]. The second method of constant current is the favored one. The feed-back loop keeps the current constant by varying the distance. The distance is controlled by piezo elements and the displacement of the tip is tracked. While an atomic scale, with vertical resolutions of order 0.01 Å can be achieved the recorded images do not have to be equivalent to the sample topography. As can be seen in equation (3.16) by replacing the summation over the discrete states by an energy integration the current. Hence the tip position are not a direct measurement of the landscape but a measurement of $n(s,E)$, the local density of states (LDOS), at position s. Keep in mind that the electronic structure of the tip is not taken into account by the simple model leading to equation (3.14). Apart from the two mentioned operation modes to obtain the sample LDOS two spectroscopy modes can be used. The STM is then sometimes called STS, an abbreviation for scanning tunneling spectroscope. To relate the topography to the electronic structure a dI/dV mode can be used. This mode is called 'differential conductivity spectroscopy mode' [110] or just dI/dV mode. In this mode the distance is kept constant and the bias is modulated by a small AC bias voltage δV. The derivative of I with respect to the voltage in equation (3.16) leads to [44]:

$$\frac{dI(s,V)}{dV} \propto n(s, E_\mathrm{F} + eV) \tag{3.17}$$

The LDOS is connected to the dI/dV data at an energy chosen by the applied bias V. Thus the dI/dV mode enhances the spin-sensitive contrast compared to the constant current mode if the energy is chosen in the energy range where the difference between the spin dependent DOS is highest.
Another method is the dz/dV mode. Here the change of the tip position during modulation of the bias voltage is recorded. This mode can be used to determined local changes

[3]Due to this disadvantage the constant distance mode is sometimes referred to as 'the fastest way to destroy the STM tip'.

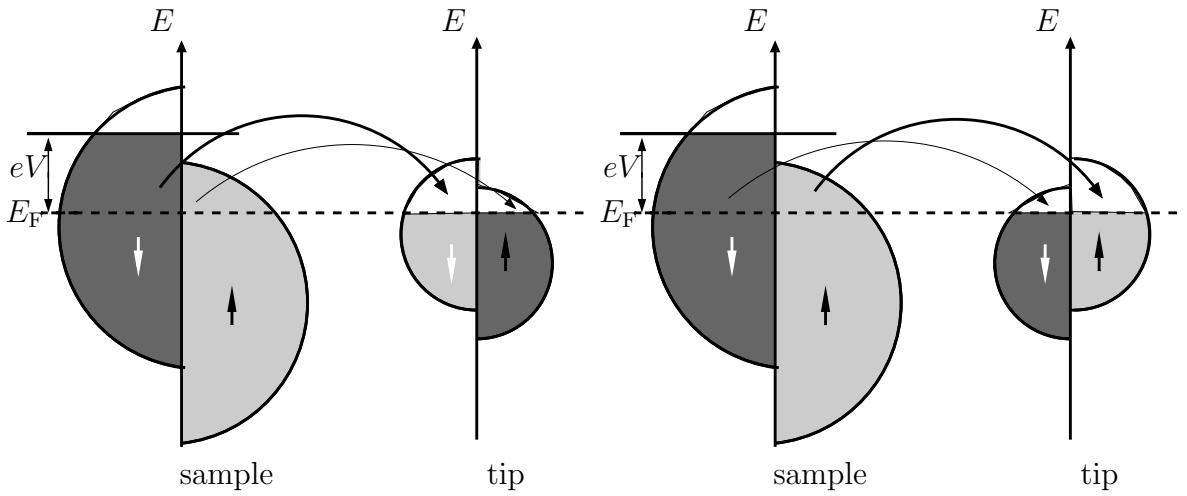

Figure 3.5: Principle of the spin dependent STM [17] in a simple Stoner model. The magnitude of the tunneling current is symbolized by the line thickness of the arrows. The more unoccupied states in the tip can be occupied via tunneling the higher is the magnitude of tunneling current.

in the workfunction of the sample or the energy position of the image potential states. So far the influence of the tip has been neglected. Three dimensional model systems taking into account the tip sample interaction are available, i.e. Tersoff, Hamman and Baratoff [107, 7] applying the Bardeen approach [8] of a transfer Hamiltonian to the small tip and an atomically corrugated surface.
Through the tunneling process the electrons conserve their energy, momentum and spin. In the usually used tungsten or platinum tips there is no spin dependency because the number of states for both spin directions is equal. But a spin-polarized STM (SP-STM) can be constructed by coating the tip with magnetic materials such as Fe or Gd. The tunneling current becomes spin dependent because the density of states of the tip is spin-dependent. The tunneling current is dominated by the contribution of the electrons from either majority band or minority band. If the magnetization direction of the tip is changed the tunneling current is dominated by the contribution of electrons with the opposite spin direction. Hence by changing the tip magnetization a magnetic contrast of the sample can be obtained. This principle is drafted in figure 3.5. In the left picture the tunneling current is mainly determined by the minority band contribution, visualized by the thicker arrow representing the tunneling current, because the tip has more unoccupied states in the minority band. If the magnetization of the tip is switched to the antiparallel case the number of unoccupied states of the spin down band decrease drastically and on the contrary the number of unoccupied states of the spin up band increases. The tunneling current is now dominated by the majority band of the sample even though less electrons above the Fermi edge contribute to the current compared to the minority band of the substrate. It is the number of unoccupied states of the tip with the same spin that is responsible for the current dependence. The same principle holds for a tip coated with a material that shows permanent magnetization. Different magnetic domains of the sample result in a different tunneling current. In this way the topology of the magnetic sample can be measured without changing the tip magentization. This mode is commonly used due to the easier setup. For a theoretical approach

to SP-STM have a look at the PhD thesis of S. Heinze [44] or his science article [45] and for some examples consult the script of Ph. Ebert [110]. For a detailed analysis of the tunneling process from one ferromagnet to another via a tunneling barrier have a look at [100]. STS can be used to measure image potential states as demonstrated by Binnig *et al.* in 1985 [10]. Recently Kupetzka *et al.* [62] used a SP-STM to investigate the spin-splitting of the image potential states and Pivetta, Ploigt *et al.* [84, 85] made STM image potential measurements of metal surfaces with overlayer of non magnetic materials.

Photoemission

In 1887 Hallewachs and Herz performed first experiments that revealed interaction of light with solids and showed the effect which Einstein explained in 1905 as the photoelectric effect[4]. He gave the fundamental photoelectronic equation:

$$E_{\text{kin}}^{\max} = h\nu - \Phi_0 \tag{3.18}$$

Φ_0 is the workfunction of the sample and $h\nu$ the energy of the photon. The maximum energy of an emitted electron of the solid is given by the difference of the energy of the photon and the energy needed to lift an electron from the Fermi edge to the vacuum level. Photons from a monochromatic source are directed on a sample and the energy $E_{\text{kin}}^{\max}$ of the via the photoelectric effect emitted photoelectrons can be measured (figure 3.6).

In a single-particle picture the distribution of the photoelectrons is an image of the occupied density of states. Since the first years of photoemission spectroscopy (PES) a lot of technical improvements have been made resulting in energy resolution up to 1 meV available nowadays.

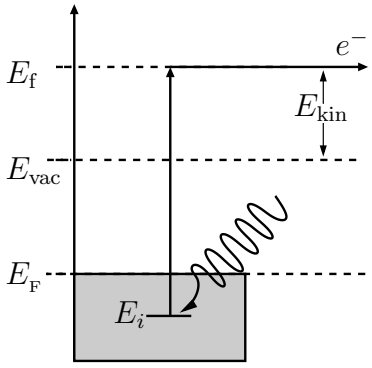

Figure 3.6: PE schematic

The distinct techniques of PES can be classified by the energy of the light used to probe the material. Valence band states can be investigated by photons with energies of some eV whereas core levels are probed by photons with energies above 1 keV. In general synchrotron light can be used. Thereby the photon energy can be selected from a continuous spectrum with high intensity and brightness but to more expense than laboratory sources. In laboratories ultraviolet photoemission (UPS) employing line spectra of discharge lamps filled with rare gases in the energy range of 10-50 eV can be used to investigate valence band states. The measurement can also be done angle resolved (ARUPS). For investigations of the core level states x-ray can be used (XPS). X-ray tubes emit light, depending on the anode materials, with energies above 1 keV.

By employing the perturbation theory in first order a theoretical description of PES can be derived. This is known as Fermi's golden rule. The photocurrent is given [49] by

$$J(\mathbf{k}) = \frac{k}{4\pi^2} \sum_s \sum_i |< \psi_{\mathbf{k},s} | H_{\text{PE}} | \psi_i >|^2 \delta(\epsilon_{\mathbf{k},s} - \epsilon_i - \hbar\omega), \tag{3.19}$$

[4]Einstein was awarded the Nobel prize in physics in 1921 "for his services to Theoretical Physics, and especially for his discovery of the law of the photoelectric effect".

where $H_{\rm PE}$ can be derived from the electron field interaction

$$H = \frac{1}{2m_e}[\mathbf{p}-\frac{e}{c}\mathbf{A}]^2 + eV(\mathbf{r}) = H_0 + \underbrace{\frac{e}{2m_e c}[\mathbf{A},\mathbf{p}]^+ + \frac{e^2}{2m_e c^2}A^2}_{H_{\rm PE}}. \quad (3.20)$$

$\psi_{\mathbf{k},s}$ is the final state s resulting from the initial state ψ_i after emitting an electron with momentum $\mathbf{k}$ and energy $\epsilon_{\mathbf{k}}$. The sum is carried out over all possible excited states $\psi_{\mathbf{k},s}$ and over all occupied electronic states in the emitter. Most of the time the quadratic term in $H_{\rm PE}$ is neglected (dipole approximation). Equation (3.19) can be rewritten

$$J_k(\mathbf{k}) = \frac{k}{4\pi^2}\sum_s \int d\mathbf{r}\int d\mathbf{r}'\psi^*_{\mathbf{k},s}(\mathbf{r})H_{\rm PE}\sum_i \psi_i(\mathbf{r})\psi_i^*(\mathbf{r}')\delta(\epsilon_{\mathbf{k},s}-\epsilon_i-\hbar\omega)H_{\rm PE}\psi_{\mathbf{k},s}(\mathbf{r}') \quad (3.21)$$

$$= \frac{k}{4\pi^2}\sum_s \Im\int d\mathbf{r}\int d\mathbf{r}'\psi^*_{\mathbf{k},s}(\mathbf{r})H_{\rm PE}G(\mathbf{r},\mathbf{r}',\epsilon_{\mathbf{k},s}-\hbar\omega)H_{\rm PE}\psi_{\mathbf{k},s}(\mathbf{r}'). \quad (3.22)$$

The sum over states in the equation above can be expressed by the spectral function $A(E)$.

$$A(E) = \sum_i \psi_i(\mathbf{r})\psi_i^*(\mathbf{r}')\delta(E-E_i) = \frac{1}{\pi}\Im G(\mathbf{r},\mathbf{r}',E) \quad (3.23)$$

This equation for the photocurrent is convenient to evaluate because the Green function is given by the initial states alone. But many aspects of photoemission can be explained better by a single-particle picture. Thereby the sum over all possible initial states ψ_i in equation (3.19) is neglected, resulting in a transition from an occupied one-electron orbital to the propagating electron state. To derive an expression we have to write the matrix elements like

$$\langle\psi_{\mathbf{k},s}|\psi_i\rangle = \langle\mathbf{k};N{-}1,s|N,0\rangle = \langle\mathbf{k};N{-}1,s|c^\dagger(\mathbf{r})c(\mathbf{r})|N,0\rangle. \quad (3.24)$$

Extending the equation above with a complete set of (N-1) states and using the electron creation operator $c^\dagger(\mathbf{r})$ and annihilation operator $c(\mathbf{r})$, we get

$$\langle\mathbf{k};N{-}1,s|H_{\rm PE}|N,0\rangle = \int d\mathbf{r}\langle\mathbf{k};N{-}1,s|c^\dagger(\mathbf{r})\left(\sum_j |N{-}1,j\rangle\langle N{-}1,j|\right)c(\mathbf{r})|N,0\rangle H_{\rm PE}. \quad (3.25)$$

Using this expression for the intrinsic contribution (j=s) in (3.19) gives:

$$J_k(\mathbf{k}) = \frac{k}{4\pi^2}\iint d\mathbf{r}d\mathbf{r}'\langle\mathbf{k};N{-}1,s|c^\dagger(\mathbf{r})|N{-}1,s\rangle H_{\rm PE}A(\mathbf{r},\mathbf{r}',\epsilon_{\mathbf{k},s}-\hbar\omega) \quad (3.26)$$

$$\times H_{\rm PE}\langle N{-}1,s|c(\mathbf{r})|\mathbf{k};N{-}1,s\rangle \quad (3.27)$$

$A(\mathbf{r},\mathbf{r}',E)$ is the interacting spectral function. Core states, energy bands and surface states measured in photoemission can be regarded as quasiparticle states in the interacting spectral function.

$$A(\mathbf{r},\mathbf{r}',\epsilon_{\mathbf{k},s}-\hbar\omega) = \sum_s \langle N,0|c^\dagger(\mathbf{r})|N{-}1,s\rangle\langle N{-}1,s|c(\mathbf{r})|N,0\rangle\delta(\epsilon_{k,s}-\epsilon_i-\hbar\omega) \quad (3.28)$$

The intrinsic contribution to the photocurrent dominates for high kinetic energies of the electrons and finite systems. Nowadays PES is used for investigation of the electronic structure of solids and surfaces and most of the knowledge about band structure and Fermi surfaces is a direct result of PES experiments. Reinert *et al.* give an extensive introduction to PES and its application in reference [89]. Another review by C. Fadley on core- and valence-level photoemission can be found in reference [110].

Two Photon-Photoemission Spectroscopy

The two photon photonemission (2PPE) spectroscopy is used to measure positions and lifetimes of intermediate states between the Fermi energy and the vacuum energy with high resolution. Therefore a pulsed laser creates an initial photon. This photon excites an electron from an occupied state of the bulk E_i to the unoccupied state E_{im} above the fermi energy. A second photon is then used to excite the electron in the intermediate state E_{im} above the vacuum level E_{vac} that can be detected energy resolved. This procedure is sketched in figure 3.7.

Obviously the energy of the initial electron has to be smaller than the workfunction to avoid single photon emission which would cover the 2PPE signal. On the other hand the energy has to be large enough to excite the electron to the intermediate states which are in case of image potential states quite close to the vacuum energy. In addition to that the lifetime of the electron in the intermediate state has to be longe enough to be excited by the second photon. In practice this forces the intensity of the photon beam to be large, limited by the heating introduced to the sample. Since image potential states on metal surfaces are long living and can easily be treated by 2PPE experiments they are the "most successful application of 2PPE spectroscopy" [34] and vice versa 2PPE is one of the most useful method to measure image potential states.

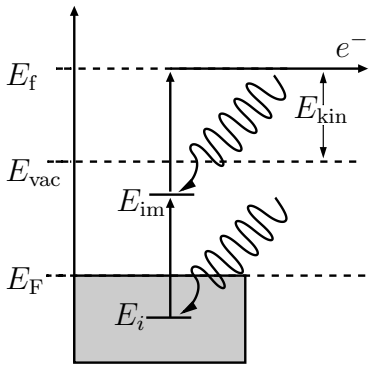

Figure 3.7: 2PPE schematic

Inverse Photoemission

The inverse photoemission is the time inverted (single photon) photoemission process explained in section 3.2.1 and sketched in figure 3.6. An electron with given initial energy E_i and defined angle of incidence is impinged into an unoccupied state E_f of the sample (figure 3.8).

The energy difference between the initial energy and the energy of the final state is emitted by a photon due to the energy conservation.

$$E_i \quad = \quad E_\mathrm{f} + \hbar\omega \tag{3.29}$$

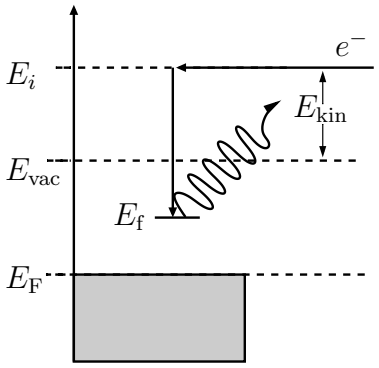

Figure 3.8: IPE schematic

The final energy E_f is given by the energy level of the unoccupied state. Surely it is above the Fermi energy E_F to be unoccupied. Furthermore it is clear that the initial energy has to lie above the vacuum energy. Inverse photoemission and photoemission complement each other but the energy resolution of inverse photoemission is limited. The resolution is up to an order of magnitude lower than in case of photoemission. For a deeper theoretical review see the report of Bostel and Thörner [19].

3.2.2 Image Potential States in `GFleur`

The potential towards the vacuum decays $1/z$ like in front of a metal surface as was derived in section 3.2 already. It is known that DFT gives an incorrect asymptotic behavior of the potential toward the vacuum due to the local and semi-local approximations used for the evaluation of the exchange correlation functional. An exponential asymptotic decay of the potential is the result of the approximations. In order to also find the image potential induced surface states the potential outside the surface has to be corrected. This can be done by starting with the exponentially decaying surface potential and mixing it with the coulomb tail of the correct potential at some distance. For `GFleur` an embedding potential for this constructed potential in the vacuum is calculated and add to the surface (embedded) region.

3.2.3 Implementation into the `GFleur` Code

Estimate the embedding potential The embedding potential of the vacuum region with the corrected potential is calculated numerically. Therefore an integration mesh in the vacuum region is generated. The analytic image potential is set up on the mesh and the value of the wavefunction and its first derivative is calculated by solving the Schrödinger equation numerically with given initial values. The embedding potential can be expressed by ψ and ψ' at the embedding plane. In order to calculate the wavefunctions at the boundary the Schrödinger equation has to be solved.

$$\left(-\frac{1}{2}\nabla^2 + V_0(\mathbf{r}) - E\right)\psi(\mathbf{r}) \quad = \quad 0 \tag{3.30}$$

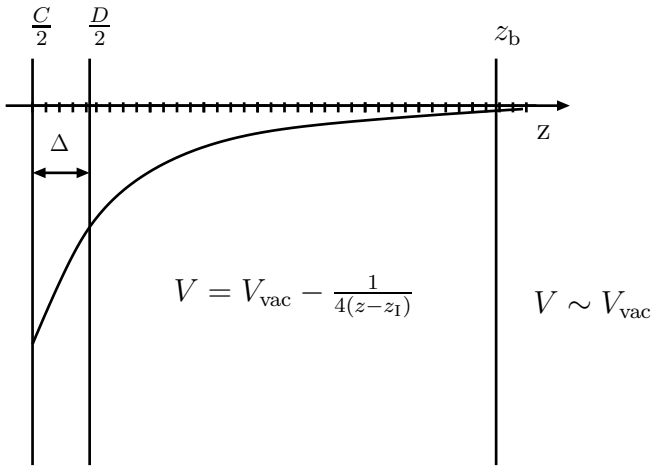

Figure 3.9: The embedding potential of the $1/z$ like potential is calculated numerically. Therefore the Schrödinger equation is solved on an integration mesh between $C/2$ and z_b. The values of ψ and ψ' at $C/2$ give the embedding potential which is then moved through the Δ region analytically. The embedding plane is located at $D/2$.

Here we can make an anzatz for the potential to be $V_0(\mathbf{r}) = V_0(z)$ and thus the wavefunctions can be given by

$$\psi_{\mathbf{k}_\parallel}(\mathbf{r}) = e^{\mathrm{i}(\mathbf{k}_\parallel+\mathbf{g}_\parallel)\mathbf{r}_\parallel}\psi(z). \tag{3.31}$$

If we use this approach the Schrödinger equation (3.30) becomes

$$\left(\frac{1}{2}(\mathbf{k}_\parallel+\mathbf{g}_\parallel)^2 - \frac{1}{2}\frac{\partial^2}{\partial z^2} + V_0(z) - E\right)\psi(z) = 0 \tag{3.32}$$

$$\Rightarrow \psi(z) = ce^{\mathrm{i}\sqrt{2(E-V_0(z))-(\mathbf{k}_\parallel+\mathbf{g}_\parallel)^2}\cdot z}. \tag{3.33}$$

At z_b in the vacuum the potential $V_0(z_\mathrm{b})$ can be approximated by a constant V_0. We get

$$\psi(z) = ce^{\mathrm{i}\kappa z} \tag{3.34}$$

with $\kappa^2 = 2(E-V_0) - (\mathbf{k}_\parallel+\mathbf{g}_\parallel)^2$. With this initial wavefunction for every $\mathbf{g}_\parallel$ at z_b the wavefunction at z_0 can be calculated numerically by the Numerov or Runge-Kutta algorithms. Both methods are known for a long time and showed to be suitable for an uncounted number of applications. While Boris V. Numerov developed his method in 1923 the work by C. Runge and M.W. Kutta was already done in 1895.[5] The more suitable algorithm is the one by Numerov because it is one order higher than Runge-Kutta and is simpler to implement. The Numerov algorithm can easily be derived by a Taylor series as will be shown in appendix A.1. For one integration step it is given by

$$\psi_{n+1} = \frac{2\left(1-\frac{5}{12}\Delta_x^2k_n^2\right)\psi_n - \left(1+\frac{1}{12}\Delta_x^2k_{n-1}^2\right)\psi_{n-1}}{1+\frac{1}{12}\Delta_x^2k_{n+1}^2} + O(\Delta_x^6). \tag{3.35}$$

[5]Just for curiosity: Both Numerov and Runge have there own lunar crater named after them.

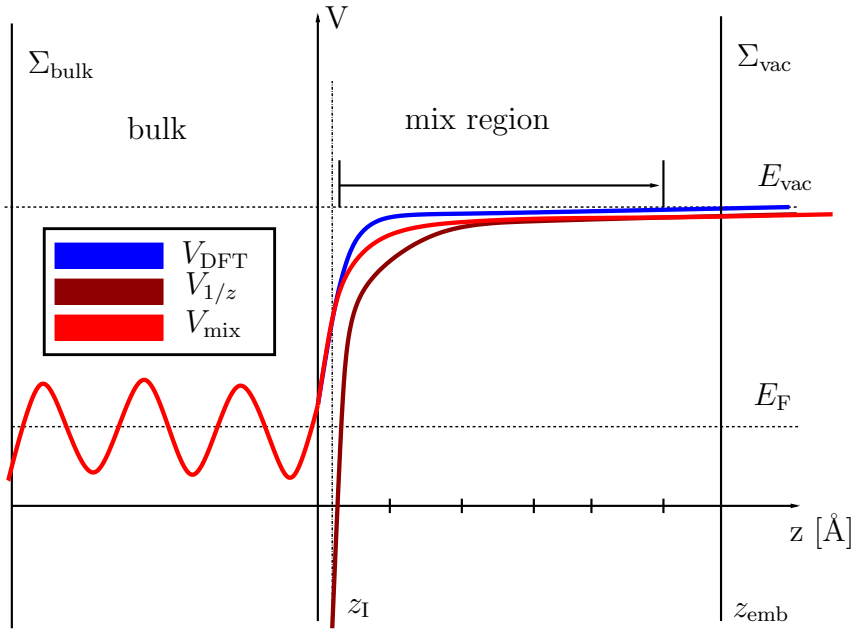

Figure 3.10: Smoothen the DFT potential (blue) my mixing the correct $1/z$ like potential (brown) in some defined mixing region into it until the correct behavior of the potential (red) is modeled.

written tidily for the mesh points n. Since in the `GFleur` implementation the vacuum region is at the right side the formula has to be rewritten as

$$\psi_n = \frac{2\left(1-\frac{5}{12}\Delta_x^2 k_{n+1}^2\right)\psi_{n+1} - \left(1+\frac{1}{12}\Delta_x^2 k_{n+2}^2\right)\psi_{n+2}}{1+\frac{1}{12}\Delta_x^2 k_n^2} + O(\Delta_x^6), \tag{3.36}$$

in order to integrate numerically from the right to the left side.
We finally get the wavefunctions $\psi_{E,\mathbf{g}_\parallel}$ and their derivatives $\psi'_{E,\mathbf{g}_\parallel}$ at z_0. We can construct the embedding potential out of them by employing equation (2.101). The position z_0 is equal to the position $C/2$ of the `GFleur` embedded region. The delta region has to be taken into account. The potential inside the delta region is set to zero. The embedding potential can be moved by (2.163) as was shown in section 2.6.5.

Smoothen the potential The potential in the embedded vacuum region is till exponentially decaying and has to be modified in order to get a smooth behavior. In figure 3.10 the mixing scheme is sketched. The red curve is the resulting potential which is the DFT (blue) calculated one before and the model potential (brown) behind the mixing region. Inside the mixing region both the DFT and the model potential are combined. As explained in 2.6.2 the Hartree potential is given by solving the Poisson equation and adding a linear correction.

$$V_{\text{H}}(\mathbf{r}) = V_1(\mathbf{r}) + V_{\text{corr}}(\mathbf{r}) \tag{3.37}$$

The Hartree potential will be corrected by mixing the coulomb potential into it.

$$V'_{\mathrm{H}} = f(z)\underbrace{\left(V_{\mathrm{vac}} - \frac{1}{4(z-z_{\mathrm{I}})}\right)}_{V_{\mathrm{model}}} + (1-f(z))\,V_{\mathrm{H}} \tag{3.38}$$

$$\underbrace{=}_{3.37} f(z)V_{\mathrm{model}} + (1-f(z))\,(V_1 + V_{\mathrm{corr}}) \tag{3.39}$$

In practice the correction of the Hartree potential is changed. We can rewrite the formula and solve for a new correction term added to the potential V_1. The potential V_1 is not fulfilling the correct boundary conditions towards the vacuum and the bulk side.

$$V'_{\mathrm{H}} = V_1 + V'_{\mathrm{corr}} \tag{3.40}$$

$$\underbrace{\Rightarrow}_{3.39} V'_{\mathrm{corr}} = f(z)(V_{\mathrm{model}} - V_1 - V_{\mathrm{corr}}) + V_{\mathrm{corr}} \tag{3.41}$$

The mixing function $f(z)$ is chosen to

$$f(z) = \left\{ \begin{array}{c|l} 0 & z < z' \\ 0.5 - 0.5 \cdot \cos(\pi \cdot \frac{z-z'}{z_{\mathrm{mix}}}) & z' < z < z'+z_{\mathrm{mix}} \\ 1 & z > z'+z_{\mathrm{mix}} \end{array} \right. \tag{3.42}$$

for simplicity.

3.2.4 Verification of the Implementation

Constant Potential The first test is to run the image potential part of the code for a constant potential V_0 equal to the vacuum level without any potential mixing. The calculated embedding potential should be the same as the one calculated analytically by formula (2.166). For the case of $(\mathbf{k}_\parallel + \mathbf{g}_\parallel)^2 = 0$ the embedding potential is given by

$$\psi(z) = ce^{\mathrm{i}\sqrt{2(E-V_0)-(\mathbf{k}_\parallel+\mathbf{g}_\parallel)^2}} \tag{3.43}$$

$$\Rightarrow \frac{\psi'}{2\psi} = \frac{\mathrm{i}}{\sqrt{2}}\sqrt{E-V_0} = \Sigma. \tag{3.44}$$

Figure 3.11 shows the embedding potential of the vacuum calculated by the `GFleur` program applying (2.166) for z=0. The `GFleur` program using the numerically-integrated embedding potential for constant potential and the analytic solution (3.44) are compared. The numerical and the analytic calculated solutions fit. Now we take the delta region into consideration. We use (2.163) in order to move through the delta region, if we integrate numerically. The real part of the embedding potential moves downwards and still the solutions fit (figure 3.12).

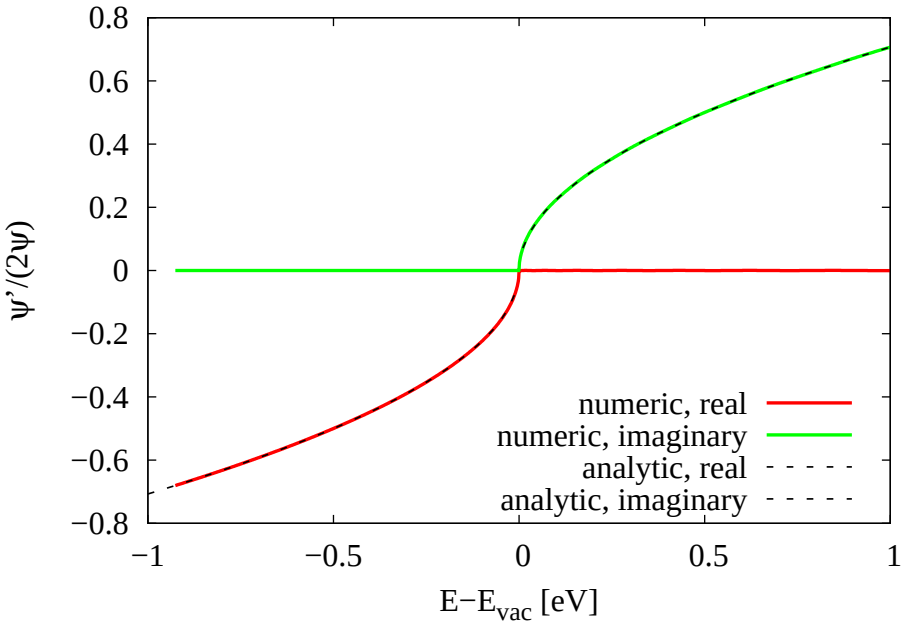

Figure 3.11: The embedding potential for a constant vacuum potential calculated analytically (dotted line) and numerically (solid lines) are compared. The results match perfectly. Both real and imaginary part of the embedding potential are plotted.

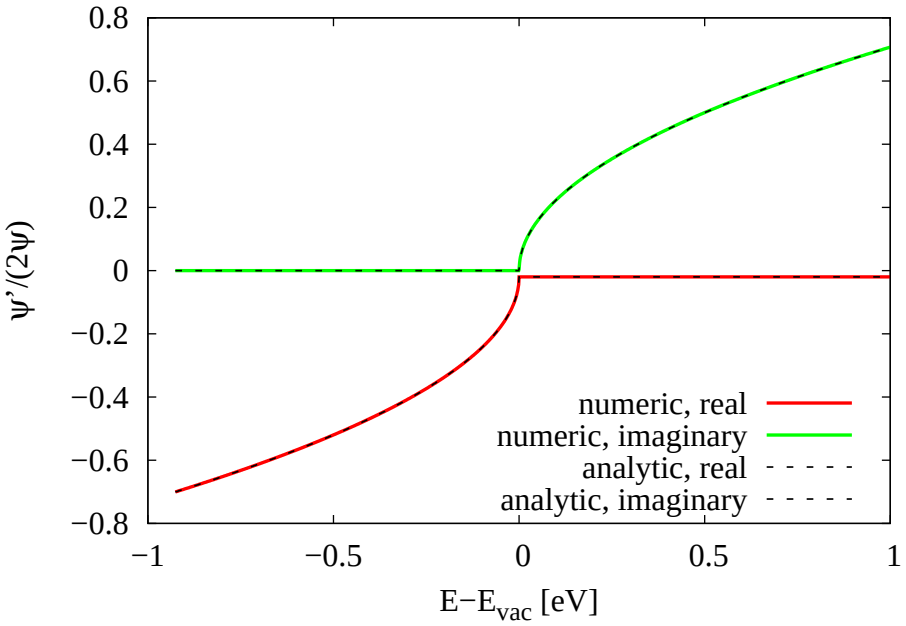

Figure 3.12: The embedding potential for a constant vacuum potential calculated analytically (dotted line) and numerically (solid lines) are compared after moving them analytically through the delta region of zero potential. It can be seen that the real part of the embedding potential of both calculations is shifted downwards.

Gridpoints The number of gridpoints used for the numerical integration determines the gridspacing, if the image boundary is kept constant. The gridspacing determines the numerical quality of the integration. In the following plots 3.13 the number of gridpoints is increased from 10^4 to 10^5 and 10^6. The image boundary z_b is set to 100 a.u. and the image plane z_I to zero giving the distance between the integration steps. We tested gridspacings of 10^{-2}, 10^{-3} and 10^{-4} a.u.. The gridspacing should be around 10^{-4} a.u. to get reasonable results. This can be reached by increasing the gridpoints as done here or by decreasing the starting point of the integration z_b. The first costs CPU time the latter might lead to numerical instability of the integration, if the z_b is chosen too close to the image plane.

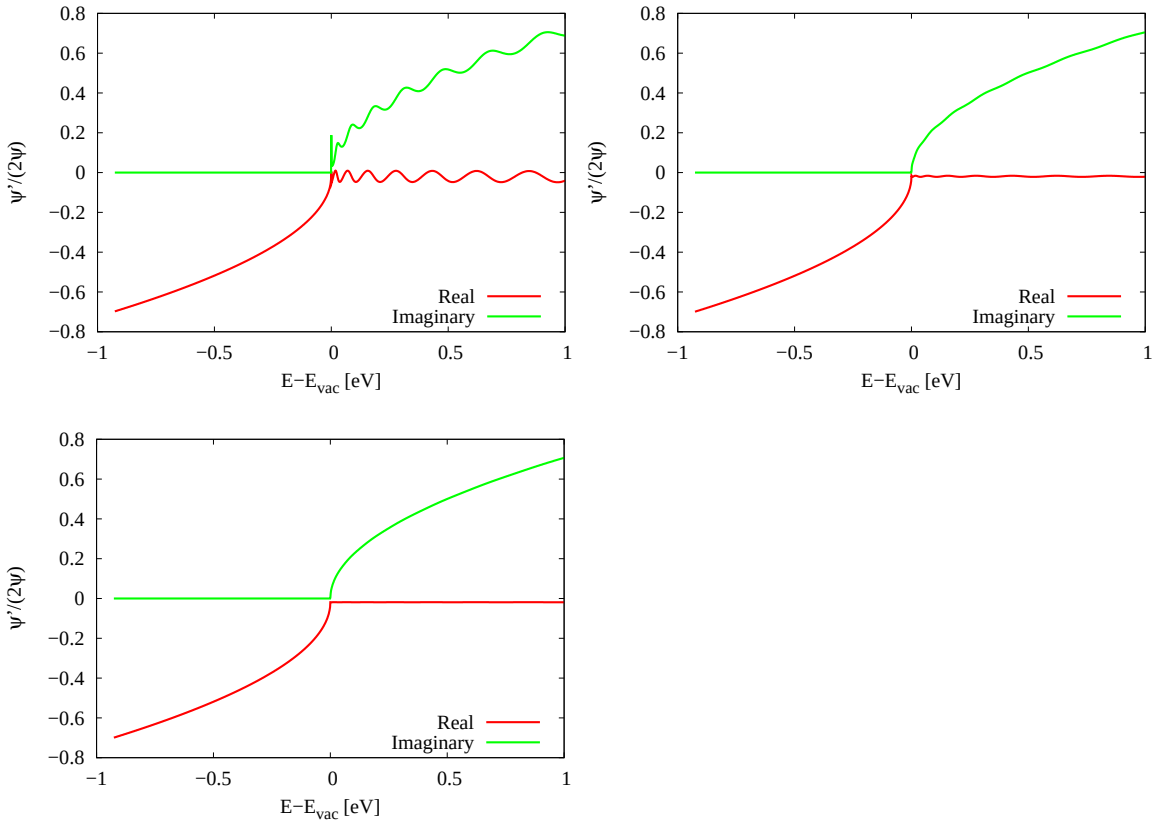

Figure 3.13: The embedding potential for a constant vacuum potential calculated numerically and moved analytically through the delta region of zero potential is drawn for increasing number of gridpoints between z_0 and z_b. The number of gridpoints determined the quality of the numerical solution of the Schrödinger equation. The gridspacing changes from 10^{-2} in the upper left corner and 10^{-3} to 10^{-4} a.u. in the lower row. It can be seen that for gridspacings larger than 10^{-4} a.u. the embedding potential exhibits numerical problems.

Imaginary Energy without V_{corr} In order to show the correct implementation of complex energies two calculation are done with an energy with imaginary part of 0.03 htr. This is a large value compared to around 10^{-5} htr used to broaden the delta peaks in the following surface calculations. The first calculation is done with the image potential generated vacuum embedding potential. This could be achieved by setting the potential equal to the vacuum level instead of using a $1/z$ like image potential. The second run is done with the analytic vacuum embedding potential. Due to the imaginary part in energy all structures of the data are washed out but the results are the same for both runs.

After these tests we are convinced that our code to give high accurate embedding potentials if the gridspacing is chosen reasonably.

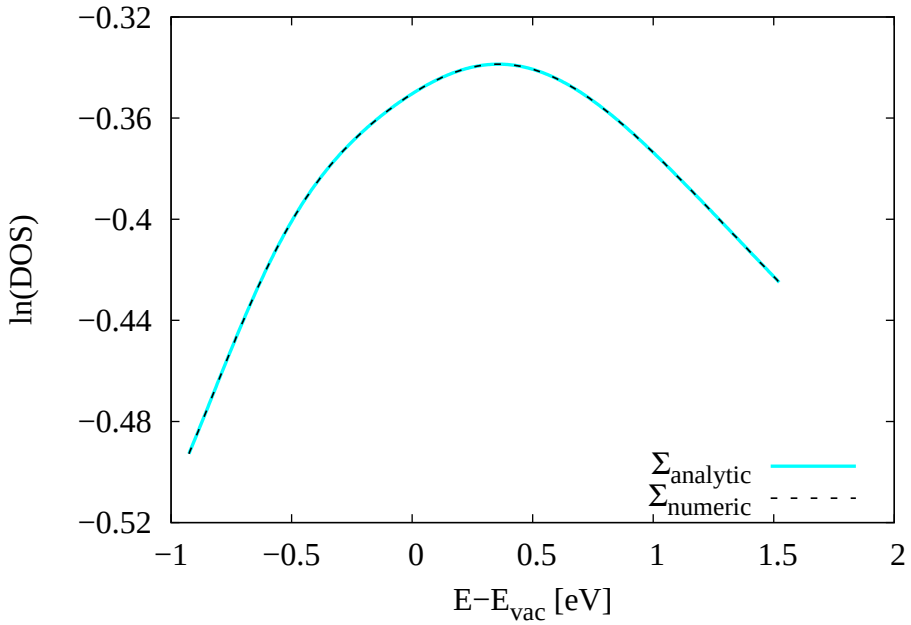

Figure 3.14: Testing the numerically determined embedding potential with complex energies of $\Im(E) = 0.81$ eV. Both analytic and numerical calculated embedding potentials result in the same density of states of the system tested.

Mixing To test the mixing, calculations with two different mixing regions are done. In figures 3.15 and 3.16 the potentials of an Ag(111) surface are shown for either a mixing region of 20 or 50 grid points. It can be seen that for larger mixing region the potential is varying slower and smoother. But it can happen that the Coulomb potential exhibits an unphysical local maximum. This would lead to an unphysical behavior of the image potential states. In contrast to a large mixing region the change of the potential is drastically in a small mixing region. The result is less smooth but without the problem of a local maximum.

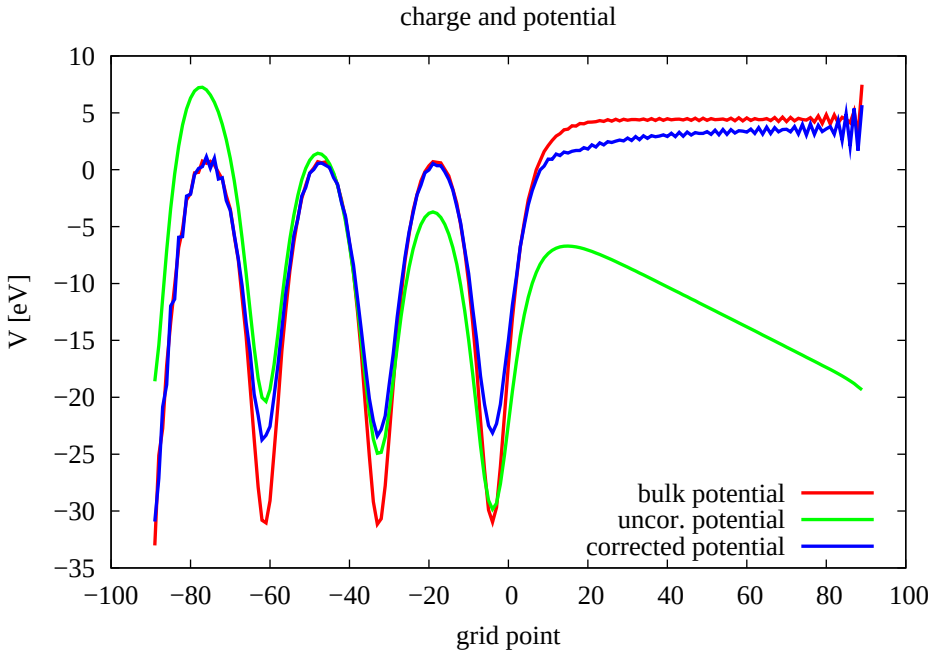

Figure 3.15: The potential of the topmost layers of Ag(111) is plotted. The potential given by a `Fleur` supercell calculation (red) and the potential of the Green function embedding calculation (blue) can be seen. Thereby the potential of the embedding method is changed by a $1/z$ like potential in a mixing region 20 grid points.

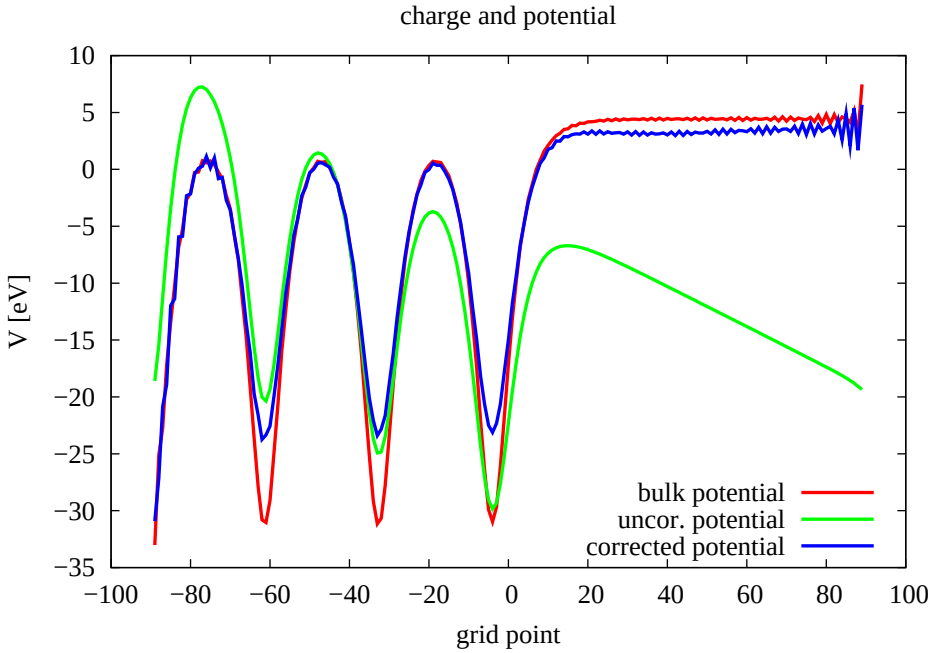

Figure 3.16: A mixing region 50 grid points is chosen this time. The blue curve representing the potential obtained by the Green function embedding technique is mixed with the $1/z$ like potential in such a large region that a local maximum results. The mixing region has to be adjusted.

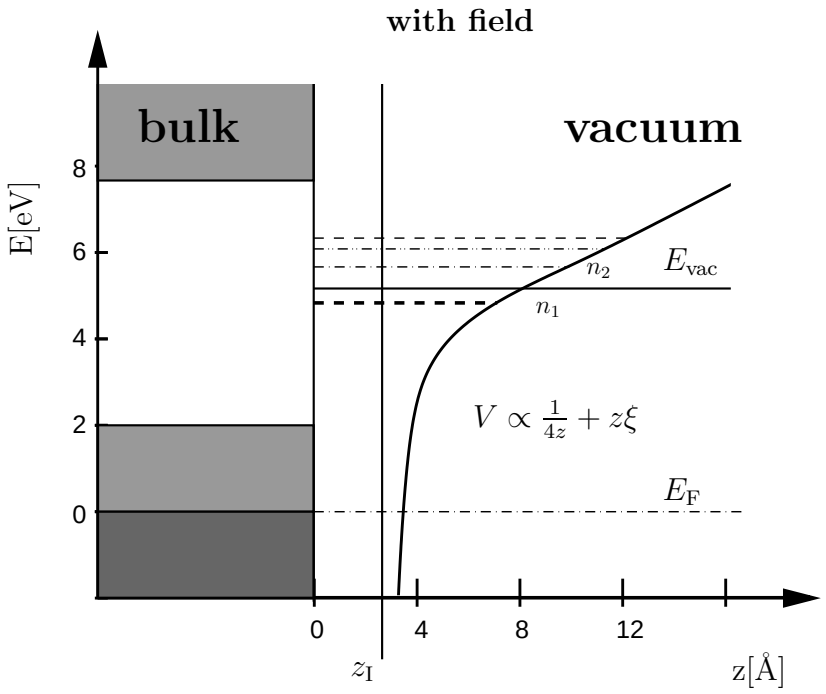

Figure 3.17: A constant electric field ξ is applied to the surface. Image potential induced field states are created. With increasing index the Rydberg states are pushed further towards the surface. This results into an increase in energy higher than the lower indexed states. Thus a large separation of these higher states can be seen.

3.3 Surface with External Constant Electric Field

If an electric field ξ is applied the image potential states at the surface are energetically shifted. In a simple model the potential can be approximated by an infinite triangular well. The eigenvalues $E_n^{\mathrm{t.w.}}$ can be given by [54]:

$$E_n^{\mathrm{t.w.}} = -\left(\frac{\hbar^2 e^2}{2m}\xi^2\right)^{\frac{1}{3}} a_n \tag{3.45}$$

The a_n are the root of the Airy function [111] of nth order. The energetically shift of the image potential states can be observed intrinsically in STM measurements. Here an electric field is always applied to the sample. The first to investigate the image potential induced states with an applied electric field were Binnig *et al.* in 1985 [10]. Binnig *et al.* called the states **field states** and that is the term we will use in the following. The systems they treated were the clean and oxygen covered Ni(100) surface and they could resolve the first 4 to 5 image states by analyzing the dI/dV spectrum. No spin resolved measurement was done. Still Ni is a demanding material to investigate with spin resolved STM because the splitting of the image state without electric field is measured with spin-polarized IPE (SP-IPE) to be only 13±3 meV for Ni(001) [104] and 18±3 meV for Ni(111) [76]. A better material to investigate is Fe(110) because the image potential splitting is found to be 57±5 meV by SP-IPE [77]. Measurements

on Fe(110) with SP-STM are done in the group of Wiesendanger [62]. The behavior of localized states in general and specially the behavior of the image potential states are sketched in figure 3.17. If compared to figure 3.2 it can be seen that the states shift up in energy. Furthermore the position of the state with respect to surface changes.

3.3.1 Implementation into the `GFleur` Code

In order to implement the electric field into our calculations the Hartree potential has to be changed. The constant electric field leads to a modified slope in the vacuum potential used for the correction (see chapter 2.6.2) of the solution of the Poisson equation. Additionally the embedding potential has to be adjust. In order to calculate the correct embedding potential the slope of the constant electric field is continued from the embedding plane towards the vacuum. The embedding potential is then calculated by a numerical integration equivalent to the procedure used for the $1/z$ like potential explained in section 3.2.3. Moving through the delta region is done analytically. The embedded Green function and consequently the charge density is calculated within the self-consistent scheme. Thereby on the one hand the correct potential inside the metallic material can be reproduced and on the other hand the correct slope of the potential towards the vacuum will be obtained.

Verification of the Implementation

In the series of figures 3.18 the potential of a surface is plotted on a discrete grid of the `GFleur` embedded region perpendicular to the surface. 6 atoms can be identified at the minima in the potential curve. The red curve is representing the potential resulting from the `Fleur` supercell calculation, the green curve the uncorrected and the blue curve the corrected potential in the `GFleur` program. In the first picture no electric field is applied to the system. The corrected potential nearly fits the potential given by the supercell calculation and is shown for comparison with the potential behavior if an electric field is applied. In the upper right plot of figure 3.18 an electric field is present. The potential before the self-consistency cycle is plotted. As can be seen in the picture the constant electric field is also present in the metallic material before the self-consistent calculations are done. The slope of the constant electric field is simply added to all the potentials inside and outside the crystal. No screening effects take place which are expected in case of a metal surface. With increasing number of self-consistent steps this slope inside the bulk is decreasing until the potential inside is flat and the constant electric field is screened 3.18c). The slope of the potential of the converged result is the same as the one applied. Thereby the correct physical properties of a metallic surface in an electric field are reproduced.

Now systems with different strength of the electric fields can be calculated self consistently. They will be used for the investigation of the image potential induced state in electric fields.

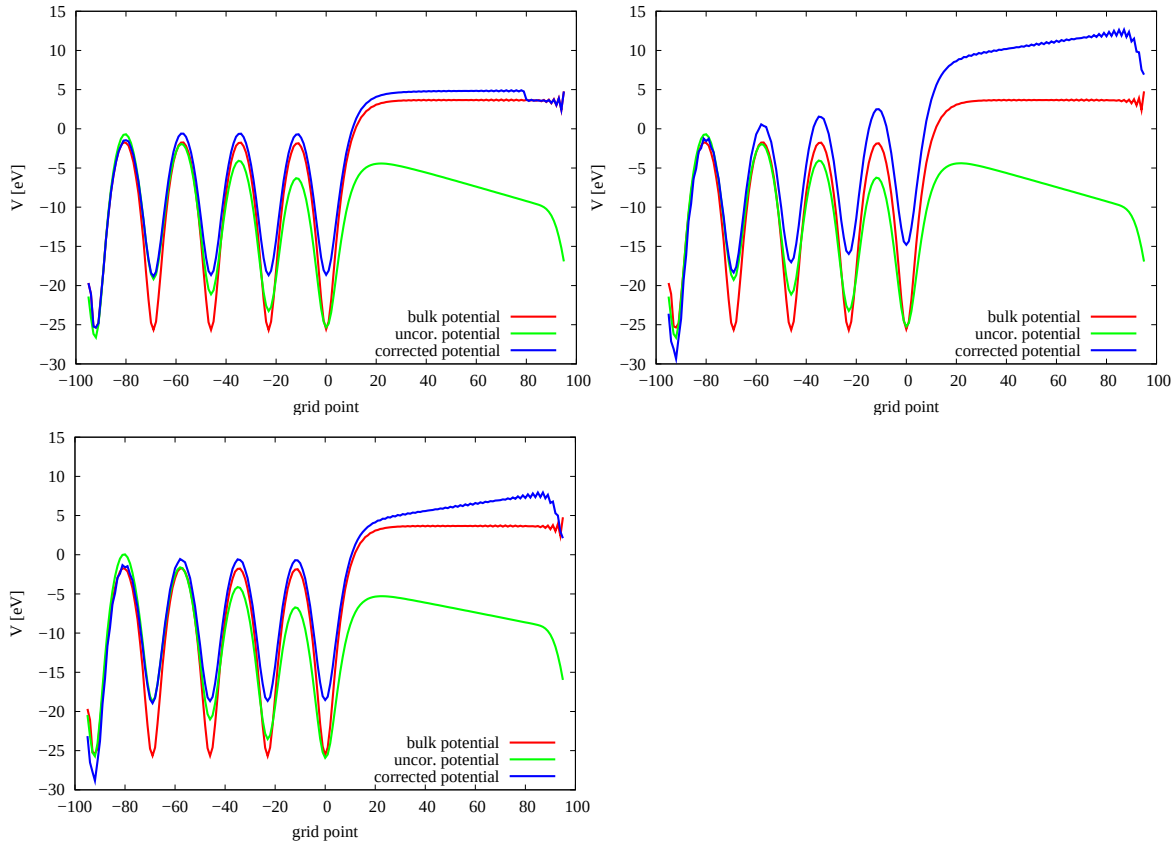

Figure 3.18: In the first picture no electric field is applied to the surface. The Green function embedding technique gives a similar potential (blue) than a `Fleur` supercell calculation (red). An electric field is introduced by changing the boundary condition towards the vacuum. An electric field of $0.01\frac{htr}{A}$ is applied and a series of self-consitentcy steps is shown. After the first iteration the potential inside the substrate increases linearly (upper right picture). In the last picture the potential after 40 iterations is plotted. Inside the substrate the potential is screened and he correct slope in the vacuum region is produced.

3.3.2 External E-Field and Image Potential States

If we take the image potential induced states into consideration, the potential towards the vacuum needs a correction to catch the $1/z$ behavior. In fact the correction to the Hartree potential is quite straightforward. In formula (3.38) V_{model} has to be changed leading to

$$V'_{\text{H}} = f(z)\left(V_{\text{vac}} + \xi(z - z_{\Sigma}) - \frac{1}{4(z - z_{\text{I}})}\right) + (1 - f(z))\, V_{\text{H}}. \tag{3.46}$$

The resulting potential is needed for the numerical calculation of the embedding potential leading to the image potential induced states. In figures 3.19 and 3.20 the potential is given for different positions of the image plane for an Ag(100) surface. In the pink curve the image potential is plotted. In order to see that the correct slope of the applied

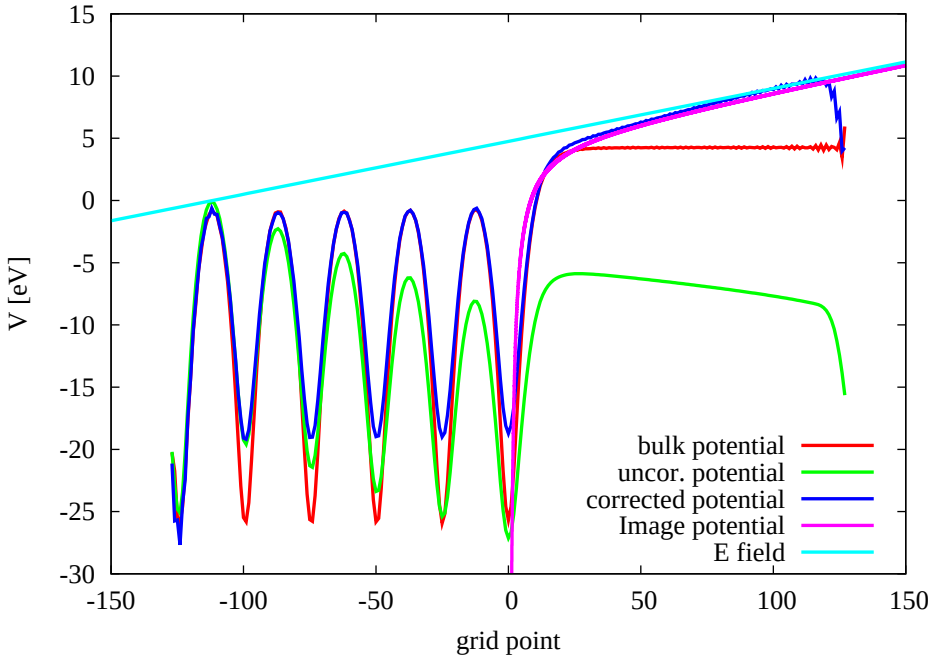

Figure 3.19: The image plane is placed at $z_{\mathrm{I}} = 0$ a.u.. The $1/(z - z_{\mathrm{I}})$ potential is given by the pink line. A constant electric field is applied to the surface. The resulting slope in the potential is close to the expected value (light blue line) after self consitency is reached.

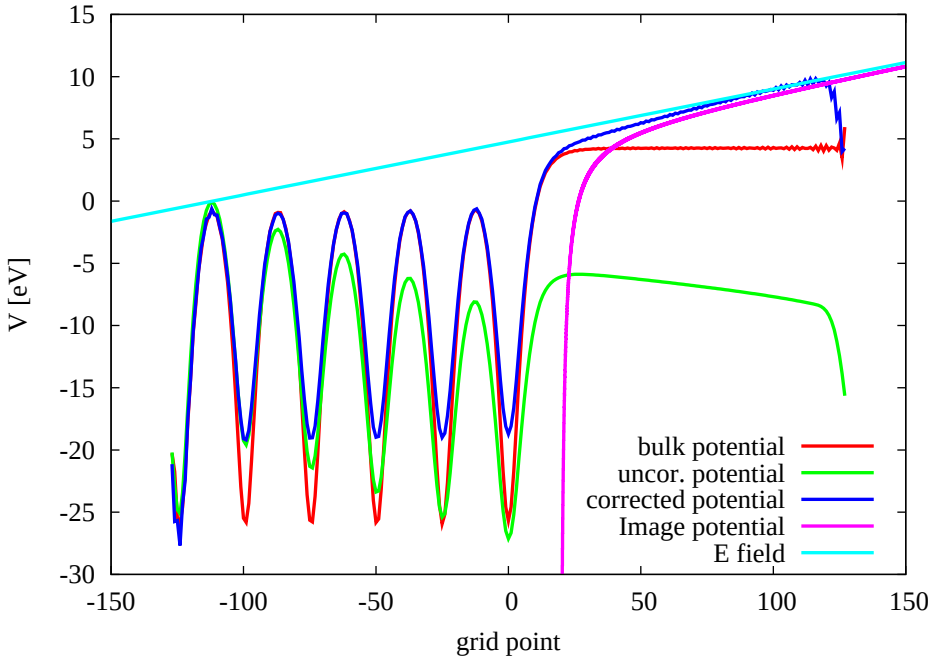

Figure 3.20: The image plane is moved to $z_{\mathrm{I}} = 3$ a.u.. Therefore the $1/(z - z_{\mathrm{I}})$ potential given by the pink line would lead to a different model potential. In this picture the potential is not yet mixed.

electric field is reproduced the blue line is drawn with the given slop. In the left picture z_{I} is set to zero in the right picture z_{I} is chosen to be 3 a.u. relative to the position of the topmost atom. In this test a mixing is not included but the embedding potential is already calculated from the image potential.

4 Calculations

The computational method we will use in the following is summarized in chapter 2.7. In section 4.1 the results of an Ag(111) surface calculation are given. A surface state close to the Fermi energy is observed at $\overline{\Gamma}$ and compared to experimental results. In this calculation furthermore the differences between a film setup and an embedding approach are discussed. We use this calculation to evaluate the accuracy of the embedding method.
In section 4.3 the image states of Ag(100) and Fe(110) are investigated without applied electric field. Thereby the non-magnetic Ag(100) is chosen to test our approach on a simple surface with huge bandgap. The bandgap allows to rule out resonance states and thereby to observe the free electron behavior of the image potential states dispersion. The magnetic Fe(110) is chosen to calculate the magnetic exchange splitting of the image states. The splitting was investigated by several experiments.
In the last section both systems (Ag(100) and Fe(110)) are calculated with applied electric fields and the image potential induced field states are investigated. STM measurements are compareable to this setup and are done in various groups.

4.1 Surface State

4.1.1 Surface State of Ag(111)

To check the accuracy of the computational method applied to localized states in a first step the surface state of Ag(111) is calculated. The surface state is located 63 meV below the Fermi energy at the gamma point of the projected Brillouin zone. Thus the state is occupied and can be investigated by photoemission spectroscopy. Such measurements were done by Reinert *et al.* on Ag, Au and Cu [90]. We will take their measurements for comparison with our calculated results.
Before the Green function embedding method is used we will start by investigating the electronic structure at the surface by a film calculation with `Fleur`. The film setup was introduced in chapter 2.2.2. By comparing the film setup results and the results obtained by Green function embedding the advantages of latter becomes obviously.
In the film setup GGA (PBE) is chosen for the exchange-correlation potential, the muffin-tin radius is set to 2.3 a.u. and the planewave cutoff is 3.7 a.u.$^{-1}$. A series of calculations is done with increasing number of layers in the film calculation. In figure 4.1 the Ag surface projected band structure is shown for four different calculations. The result of a 11 layer film setup is given in the upper left corner of figure 4.1. A surface state close to the Fermi level is visible at $\mathbf{k}_{\parallel} = \overline{\Gamma}$. It splits into two lines because of finite size effects. Since the film has a finite size the two surfaces interact resulting in the splitting of the surface state. Additionally, we get a finite number of lines in the projected band instead of a continuous band because the states are calculated for a finite

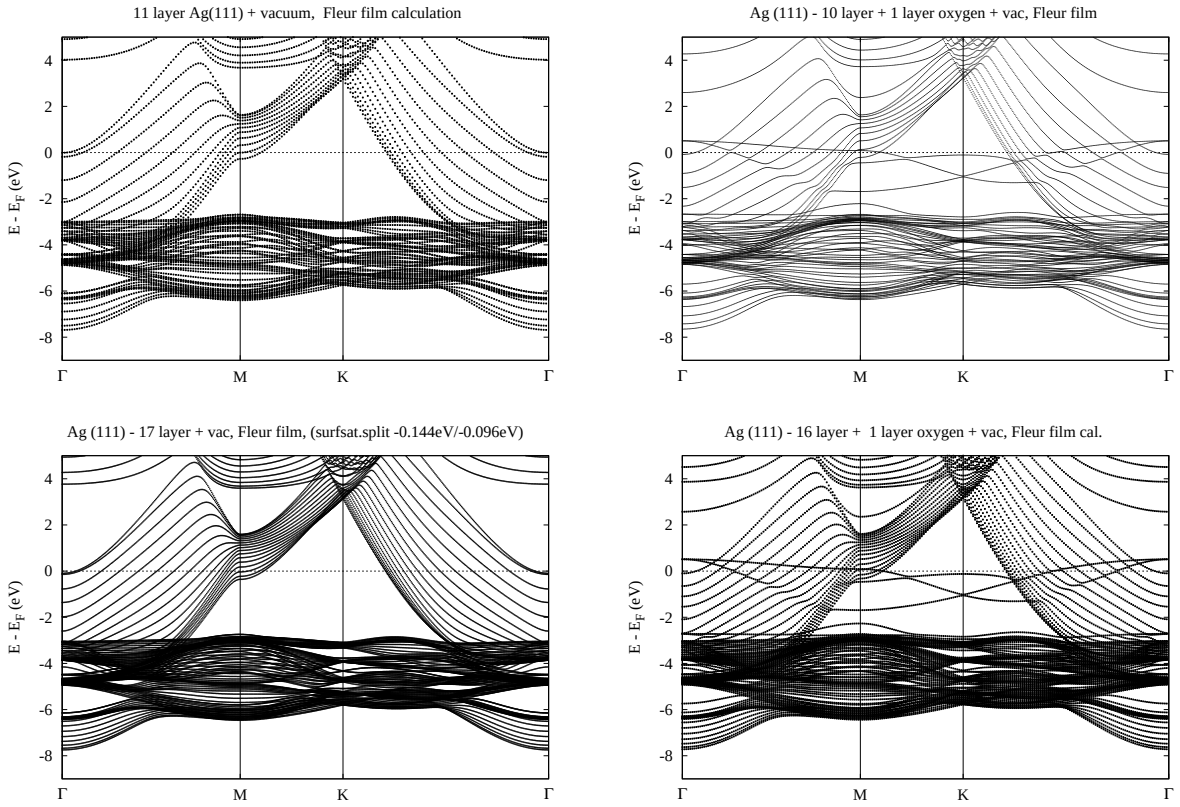

Figure 4.1: `Fleur` film calculations for different systems. On the left hand side the projected bandstructure of 11 layers of silver and 17 layers of silver are shown. The projected bands are discretised due to the finite system size. Also the surface state is splitted because the both surfaces states can interact. With increasing number of layers this effects become less important. In order to get rid of the surface state splitting one surface can be covered by a different material, destroying the surface state on this surface. The results of a layer of oxygen onto one of the surfaces can be seen on the right hand side. The surface state is not split but additional states are introduced.

system and the continuous band results from an infinite substrate. The interaction of the two surfaces is decreasing with film thickness as can be seen by comparing with the bandstructure of the 17 layer system drawn in the lower left corner. With an infinite substrate the splitting will disappear and the projected band will be continuous. This is what `GFleur` will provide. An alternative solution to the problem of surface state splitting is to cover one film surface with a different material annihilate one surface state. The remaining surface state cannot interact with the surface state with at same energy on the other surface anymore and the splitting is vanishing. This is done by a layer of oxygen instead of one of the topmost Ag layer. The results are shown on the right hand side of figure 4.1. The splitting of the surface state disappears but new states are created, due to the oxygen. Note that the system is not inversion symmetric any more and the computational effort increases. In order to get a reasonable value of the surface state energy a 21 layer film calculation is done. The unit cell contains 21 Ag atoms and is inversion symmetric. In figure 4.2 the projected band structure of the

Ag(111) surface is given. The region close to the Fermi level is enlarged in order to resolve the splitting. The position of the surface states is determined to $-28/-49$ meV and presented in the table 4.1. The position is some meV above the measured one. More layers and a relaxation of the surface would probably result in a better agreement with the experiment.

Now the Green function embedding method will be used with the same exchange

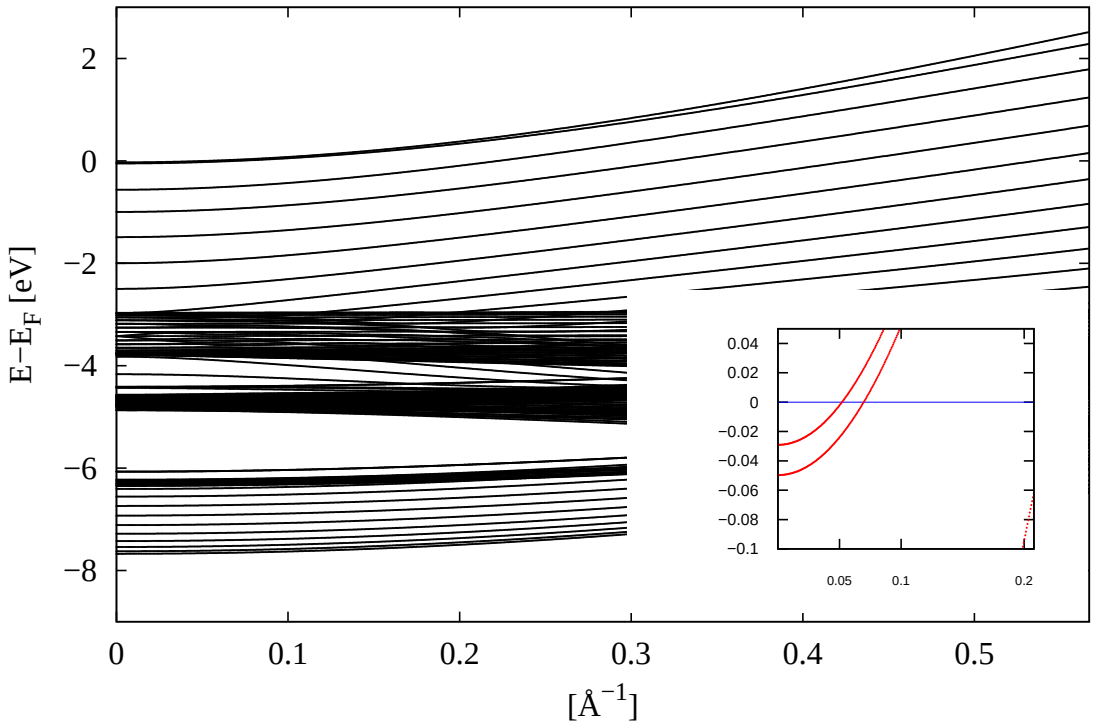

Figure 4.2: The bandstructure of the Ag(111) supercell of 21 layers at $\mathbf{k}_{\|} = \overline{\Gamma}$ towards $\overline{M}$ is plotted. The splitting of the surface state can be seen in the enlarged subfigure.

correlation potential. A seven layer slab of silver atoms is separated by a vacuum region of 19.78 a.u.. The muffin-tin radius is set to 2.235 a.u., the planewave cutoff for the wavefunction basis to 3.7 a.u.$^{-1}$ and the cutoff for the potential basis set to 18.2 a.u.$^{-1}$. The charge density of the embedded region built from the three topmost layers of the slab is then calculated self consistently by the Green function embedding method. A set of 15 energies and 55 **k**-points from the irreducible part of the Brillouin zone are chosen and the basis set cutoff is reduced to 3.5 a.u.$^{-1}$. The energies are taken from a half circle in the imaginary plane, running from the lowest valence band energy to the Fermi energy. The **g** vectors defining the basis are taken from a spherical region of the reciprocal space in the self-consistent run. In the case of the embedding potential calculation the **g** vectors are chosen from a cylindrical region. In order to obtain the plot 4.3, the **k**-resolved density of states n(E,**k**) (spectral function) has to be calculated for 1600 different energies and 200 points in the two dimensional Brillouin zone along

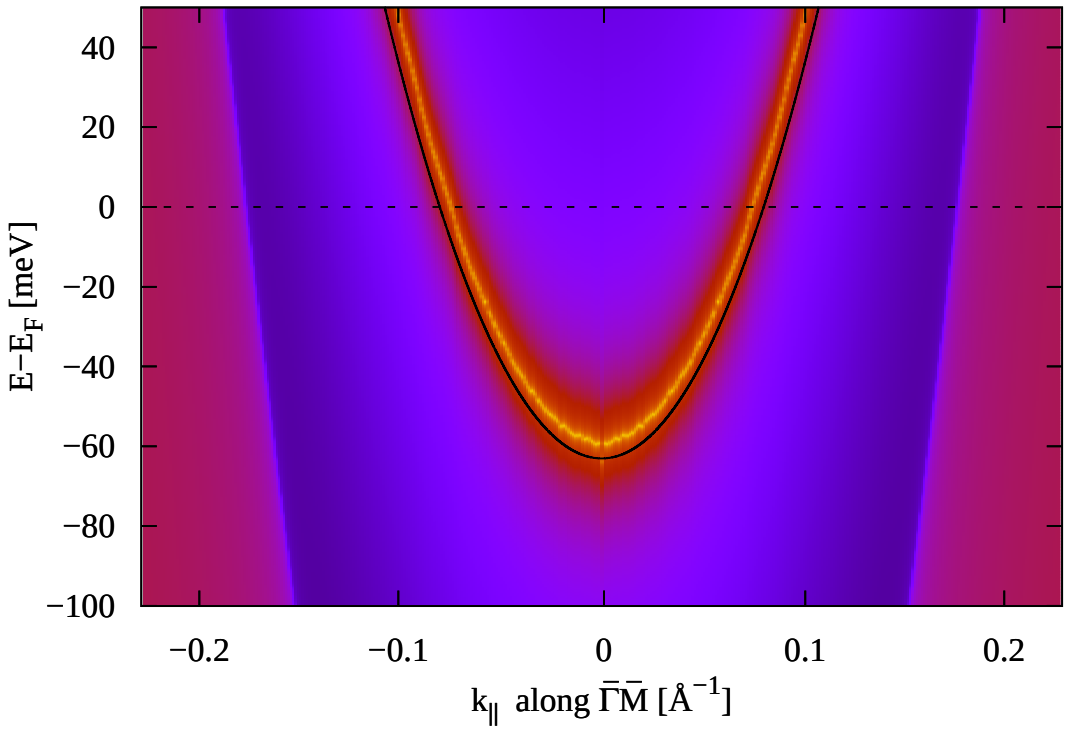

Figure 4.3: **k**-resolved density of states n(E,**k**) of Ag(111) along $\overline{\Gamma M}$. Bright colors representing huge DOS. The calculated surface state can be compared to the experimental result given by the black line.

the high symmetry line $\overline{\Gamma M}$. Note, that in the plot the data is mirrored at the Γ point and therefore 400 **k**-points are drawn. The energy has a small imaginary part in order to resolve the localized state, because the state is a delta peak in n(E,**k**). The broadening by different values of imaginary energy are tested and the value of 1.36 meV is determined to give good resolution without washing out the state. Experimental results from Reinert *et al.* [90] are given as black line in figure 4.3. The experimental value is nicely reproduced. Note that the energy scale is meV resolved.

	E [meV]	k_F [Å^{-1}]
DFT & film 21 layers	−28/−49	0.053/0.072
DFT & embedding	−59	0.075
exp. (PE) [90]	−63±1	0.080

Table 4.1: Theoretical results compared to experimental value of the Ag(111) surface state position.

4.2 Image Plane

The image plane z_I introduced in chapter 3.2 can be seen as the center of screening charge in the electrostatic case [64]. The screening charge is induced into metallic surfaces if an electric field is applied. The charge distribution is roughly approximated by using the lateral average pseudocharge. The distribution can be calculated for different applied electric fields. This approach gives reasonable results.

4.2.1 Screening Charge Ag(100)

We use the relaxed setup and the exchange correlation potential of LDA to calculate the center of gravity of the screening charge. By calculating the mean screening charge position from the lateral-averaged charge we get approximately 2.7 a.u.. Our calculated value is close to the result obtained by Ishida and Liebsch [53] who got 2.86 a.u.. The positions are given on the vacuum side relative to the atomic surface. In figure 4.4 the lateral-averaged screening charge are plotted for three different values of the electric field. The screening charge is given by the difference between the charge distribution with and without an applied electric field.

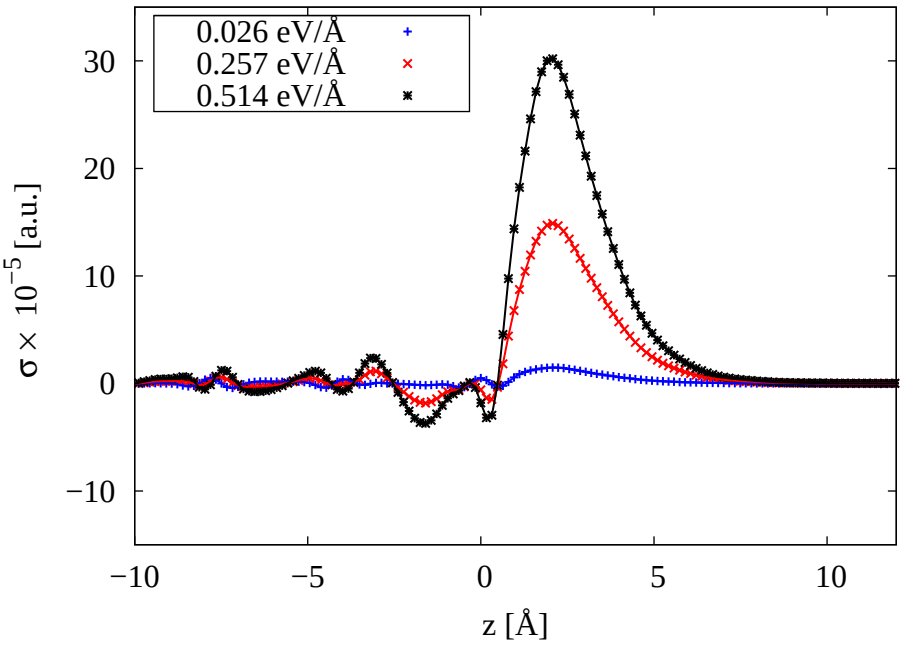

Figure 4.4: Screening charge σ induced into the Ag(100) surface with different values of electric field. $z = 0$ marks the atomic surfaces. The center of screening charge can be regarded as the image plane position z_I.

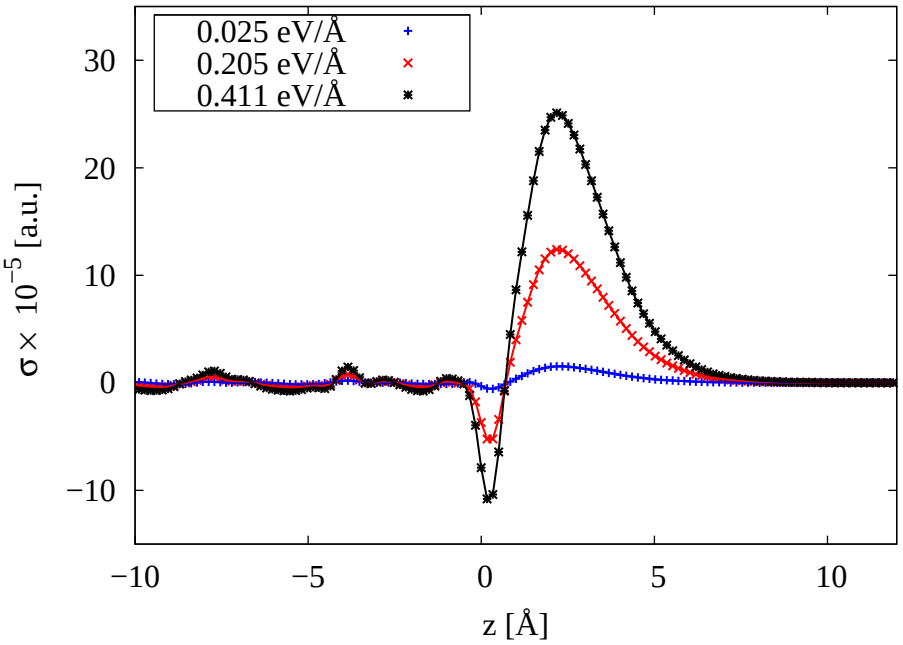

Figure 4.5: Screening charge σ induced into the Fe(110) surface for different values of the applied electric field.

4.2.2 Screening Charge Fe(110)

In order to estimate the position of the the image plane the center of gravity of the screening charge is calculated for several values of the applied field. The self-consistent LDA calculation in the unrelaxed setup is taken. The lateral-averaged pseudo charge is used and a position of the image plane of around 3.1 a.u. results. To our knowledge there is no further published position for the Fe(110) image plane calculated by *ab initio* methods available. Figure 4.5 shows our calculated screening charges for several different values of applied electric field.

4.3 Image Potential States

We will calculate the image potential states of Ag(100) and Fe(110) in the following sections. For both surfaces the surface setup will be explained in detail because the influence of the surface relaxation will be investigated. Therefore the results of setups employing the experimental lattice constant are compared to setups using the theoretical estimated lattice constant with relaxed surface layers.

4.3.1 Image Potential States of Ag(100)

Surface Setup The image potential states are influenced by the potential in the vacuum region. Therefore the workfunction of the surface should be correct estimated. Since the relaxation of the atoms at the surface result in a change of the workfunction the surface relaxation has to be taken into account. In order to estimate the relaxed atom positions the `Fleur` code offers the option to calculate forces on individual atoms. Before the forces of the topmost layers of atoms can be calculated the lattice constant of the substrate has to be determined. This is done by calculating the bulk system of minimal energy with respect to the lattice constant. For the calculation LDA in the parametrization by v. Barth and Hedin [9] (called BH in the following) and for GGA in parametrization by Perdew, Burke and Ernzerhof [80] (abbreviated by PBE) is used. The total energy of the bulk system is calculated for several different lattice constants. The results are plotted in fig 4.6, where the red line is a guide to the eye. The minimum of the total energy is extracted by a parabolic fit (green curve) through a set of the lowest data points. The resulting lattice constants are 3.993 Å (LDA) and 4.147 Å

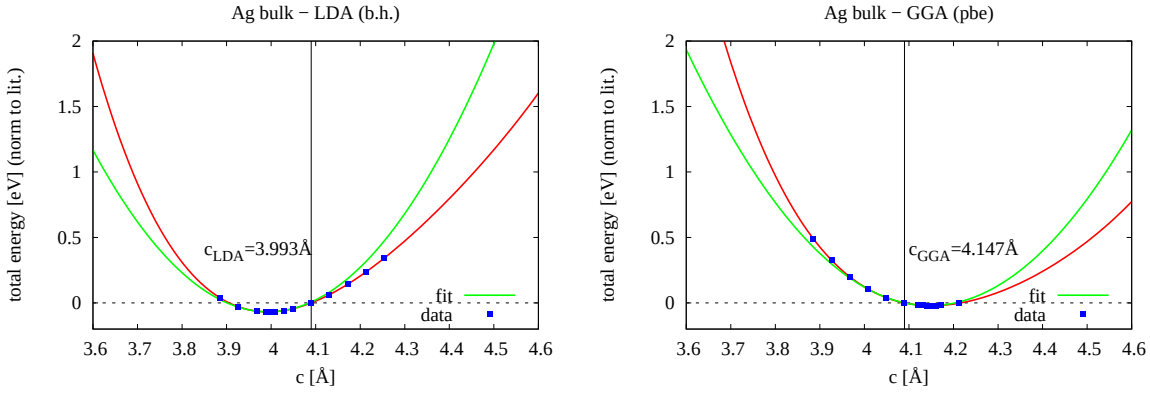

Figure 4.6: Estimated the theoretical lattice constant of Ag bulk by searching for the setup with lowest total energy.

(GGA). The results are in good agreement with the results given by Asato *et al.* [6] who calculated 3.989 Å (LDA) and 4.138 Å (GGA). Pivetta *et al.* [84] estimated the lattice constant to 4.19 Å and Clarke *et al.* [25] 4.15 Å in case of a GGA. Asato and Pivetta used GGA with PW91 the parametrization by Perdew and Wang [81]. In comparison with the experimental lattice constant of 4.09 Å[120] the general trend can be reconfirmed that LDA gives a too small lattice constant and on the contrary that GGA slightly overestimated the value.

The forces acting on the atoms of the three topmost layers are calculated in the following with the lattice constant of lowest energy. A planewave cutoff of 4.0 a.u. and 45 **k**-points give converged results. Clarke *et al.* state that the Δd_{ij} are expected to be insensitive to the choice of the functional. Using their argument we only investigate the relaxation employing the GGA approximation. Thereby Δd_{ij} is the change in separation between the first and second layer given as a percentage of the bulk interlayer distance ($\Delta d_{ij} = (d_{ij} - d_0)/d_0$). Our results are in well agreement with other calculated values and they are summarized in tabular 4.2. Thus for the surface setup we get spacings sketched in figure 4.7.

	this work c=4.147 Å	Clarke *et al.* [25]	Bohnen *et al.* [18]	Methfessel *et al.* [68]
Δd_{12}	−1.15	−1.86	−1.3	−1.8
Δd_{23}	+0.92	+0.68	+1.0	-
Δd_{34}	+0.85	-	-	-

Table 4.2: Relaxation of Ag(100) in percent of the unrelaxed interlayer spacing.

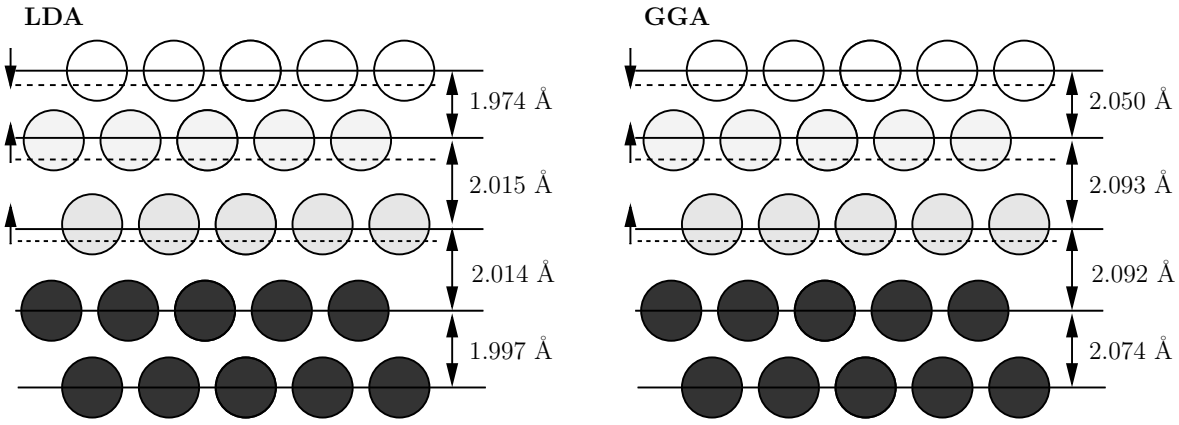

Figure 4.7: Positions of the relaxed Ag(100) surface atoms. The topmost three layers are relaxed.

Workfunction The Green function embedding method is applied until self consistency is reached. In order to evaluate the influence of the exchange correlation approximation and system relaxation used three calculations of the workfunction for each approximation are done. The first calculation uses the experimental lattice constant while the second uses the theoretical lattice. The third calculation is additionally taking the relaxation of the three topmost layers into account. The FLAPW-method with a 9 layer film setup using GGA and LDA is employed for comparison for all three cases. The workfunction calculated with the `Fleur` program is determined by a series of self-consistent 9 layer film calculation with increasing planewave cutoff and number of **k**-points in the Brillouin zone. The values of parameters are increased until the results of the workfunction become stable. The results of our workfunction calculation are summarized

c [Å]	layer relaxed	method		ϕ [eV]
4.09	-	FLAPW (`Fleur`)		5.12
3.993	-		LDA (BH)	5.15
3.993	√			5.14
4.09	-			4.27
4.147	-		GGA (PBE)	4.25
4.147	√			4.25
4.09	-	FLAPW+embedding (`GFleur`)		5.59
3.993	-		LDA (BH)	5.47
3.993	√			5.46
4.09	-			4.72
4.147	-		GGA (PBE)	4.69
4.147	√			4.58

Table 4.3: Calculated workfunction of Ag(100). Results of the `Fleur` film calculations in the upper and the results obtained from Green function embedding in the lower part of the table.

in table 4.3. The LDA calculations always overestimate the workfunction. The GGA results are comparable to the experimental values. We will use the GGA in the following to determine the image potential states. Our results can be compared to experimental and theoretical workfunction. In table 4.4 published values for the workfunction of the Ag(100) surface are summarized. Experimental results are given in the upper and calculated values in the lower part of the table. It can be seen that the Green function approaches slightly overestimate the value for the workfunction of Ag(100) while slab calculations come close to the experimental values found by 2PPE or PE measurements. It seems to be a general phenomenon that the Green function method gives slightly higher workfunctions than the corresponding DFT film or supercell calculation. For the Cu and Au surface this was also observed by Ohwaka, Ishida and Liebsch [74]. They calculated $\phi_{\mathrm{Au(111)}}$=5.67 eV, $\phi_{\mathrm{Au(001)}}$=5.71 eV, $\phi_{\mathrm{Cu(111)}}$=5.19 eV and $\phi_{\mathrm{Cu(100)}}$=5.01 eV all slightly above the experimental workfunctions.

Calculate the Image Potential States We calculate the embedding potential from the CBS of bulk silver. The embedding region is cut out of a supercell calculation with 9 layers. The region includes the middle layer, the 4 surface layers and a vacuum region of 17 a.u.. The embedding potential is replacing the atom layer to the left of the atomic layer in the middle of the slab. The planewave cutoff determining the size of the interstitial basis set is chosen to 3.4 a.u.$^{-1}$. The muffin-tin radius of the Ag atoms is chosen to 2.235 a.u.. The embedding potential is calculated with a planewave cutoff of 3 a.u.$^{-1}$ and napw[1] set to 15. A self-consistent charge density of the embedding region is calculated with a mesh of 16 **k**-points in the irreducible part of the projected two dimensional Brillouin zone and 15 energies lying on a half cycle in the imaginary plane.

[1]napw=number of augmented plane waves

		method	published	ϕ [eV]
Schuppler *et al.*	[94]	Bi2PPES	1990	4.43 ± 0.01
Giesen *et al.*	[39]	2PPES	1987	4.42 ± 0.02
Reihl *et al.*	[88]	IPE	1987	4.35 ± 0.05
Chelvayohan *et al.*	[23]	PE	1982	4.22 ± 0.04
Dweydari *et al.*	[29]	PE	1974	4.64 ± 0.02
Pivetta *et al.*	[84]	DFT - PAW GGA (PW91), c=4.19 Å	2005	4.36
Ishida and Liebsch[1]	[53]	DFT+embedding FLAPW/LDA	2002	4.71
Ishida	[52]	DFT+embedding FLAPW/LDA	2001	4.80
Aers and Inglesfield	[2]	DFT+embedding LAPW/LDA (BH)	1989	4.95
Smith *et al.*	[101]	DFT - local orbital LDA (Wigner)	1980	4.2

Table 4.4: Workfunction of Ag(100) given in literature. Experimental values in the upper part of the table. Results of DFT calculations are summarized in the lower part of the table. [1]Improved version of the embedding potential generated from the CBS of bulk Ag compared to reference [52].

The position of the image plane is set fixed to the position calculated by Ishida and Liebsch [53]. By a first-principle surface embedded Green function approach they got a position of 2.86 a.u. on the vacuum side of the surface relative to the atomic position[2] of the topmost layer. In literature Aers and Inglesfield [2] and Weinert *et al.* [113] give values of the image plane close to the one calculated by Ishida *et al.*. The mixing region starts 14 a.u. in the vacuum region behind the atomic plane. The mixing function is applied in a region of 7.97 a.u. (50 points on the FFT grid). Thereby the potential is only slightly modified. The calculated local density of states (LDOS) at $\mathbf{k}_{\parallel} = \overline{\Gamma}$ for the unrelaxed GGA calculation is plotted in figure 4.8. The result for the case of the relaxed silver surface in (100) orientation can be seen in figure 4.9. Comparing both reveals that the relaxation of the surface results in a better agreement of the image state energies with experimental data. The effect on the first image state located closest to the surface is a shift of around 50 meV. The higher Rydberg states are less influenced by moderate changes of the surface due to their positions further outside in the vacuum. The experimental results of a 2PPE experiment by Schuppler *et al.* are given in table 4.5 and as dotted line in the picture. Our calculated states are below the experimental results except for the measurement of Reihl and Nicholls [88]. They got a value close to our result for $n = 1$. To our knowledge there are no other *ab initio* calculations of the image potential states of Ag(100) available in literature in order to compare our results whereas theoretical approaches with model potentials of course always reach close to

[2]Sometimes the geometric surface is used for reference. The geometrical surface is placed 1/2 interlayer spacings above the surface while the atomic plane is given by the atomic position of the topmost layer.

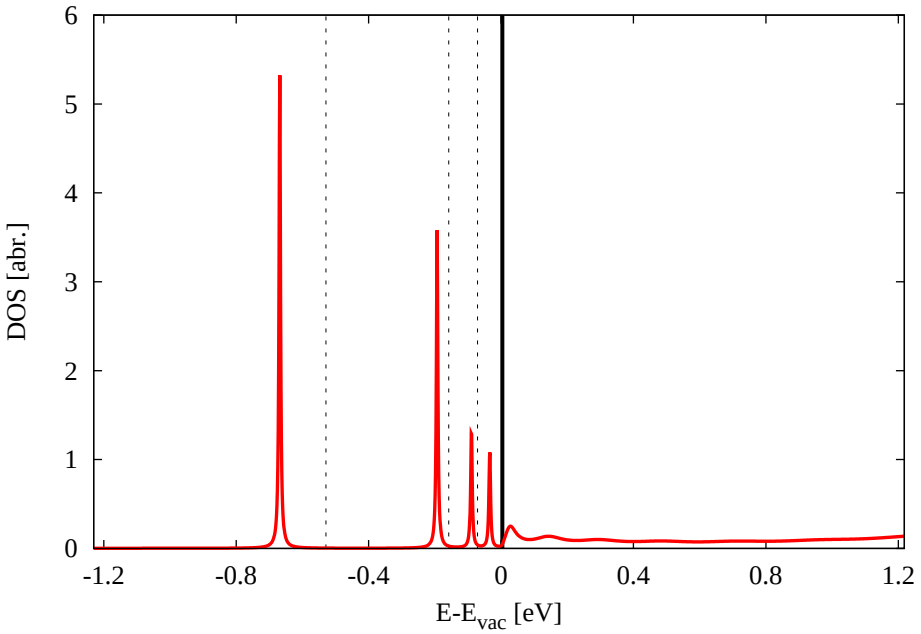

Figure 4.8: The LDOS of the Ag(100) surface at $\mathbf{k}_{\parallel} = \overline{\Gamma}$ (unrelaxed GGA) is plotted. The first four image potential states can be seen. Experimental values are given by vertical dotted lines. Delta peaks broadened by $\Im(E) = 10^{-4}$ htr (2.7 meV).

the measured values [34].

		method	E_1 [eV]	E_2 [eV]	E_3 [eV]
Goldmann *et al.*	[40]	IPE	-0.5 ± 0.2	-	-
Schuppler *et al.*	[94]	2PPE	-0.533 ± 0.015	-0.162 ± 0.015	-0.075 ± 0.015
Altmann and Dose	[4]	BIS	-0.5 ± 0.2	-	-
Reihl *et al.*	[87]	IPE	~ -0.5	-	-
Reihl and Nicholls	[88]	IPE	-0.67	-	-
this work:					
GGA unrelaxed		embed-	-0.668	-0.193	-0.090
relaxed		ding	-0.613	-0.182	-0.087

Table 4.5: The positions of the image potential states of Ag(100) observed by experiment are compared to our results.

Calculate the Dispersion Relation In order to calculate the behavior of the image potential states a set of 21 **k**-points along a high symmetry line of the two dimensional Brillouin zone starting at $\overline{\Gamma}$ is chosen with a mesh of 200 energy points. The setup is unchanged to the one used for calculating the image potential positions. In figure 4.10 the dispersion relation of the first image potential states of the Ag(100) surface can be observed. The dispersion of a free electron is given by the bright turquoise line in the

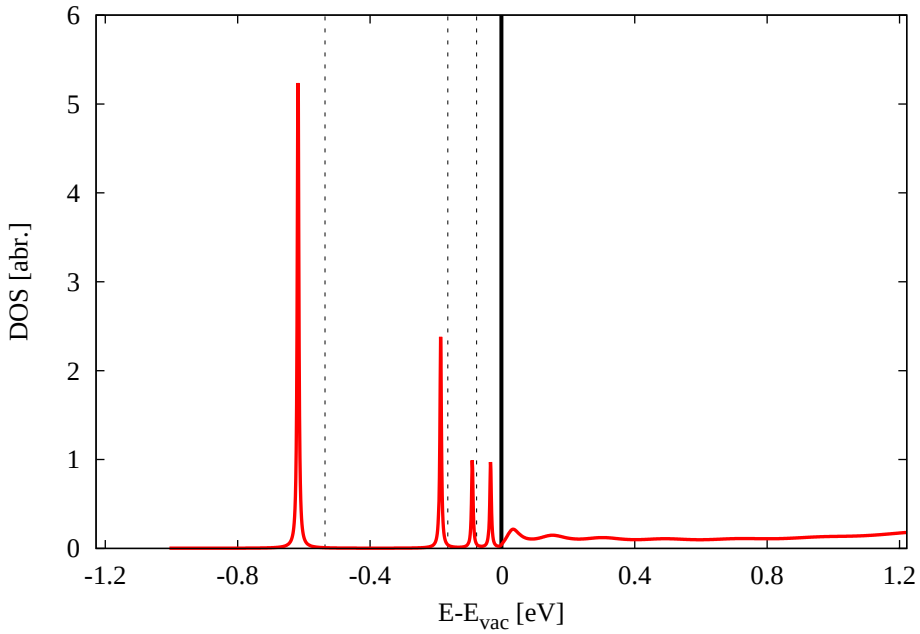

Figure 4.9: The LDOS of Ag(100) at $\mathbf{k}_{\parallel} = \overline{\Gamma}$ (relaxed GGA) is plotted with $\Im(E) = 10^{-4}$ htr (2.7 meV). The three topmost layers are relaxed. The positions of the image potential states are close to the experimental values given by vertical dotted lines.

plot for comparison. By a first qualitative investigation the effective mass of the state is close to the electron mass. This result is expected because the electrons are located far outside the surface and therefore are free in the two dimensional plane parallel to the surface. In 1985 Garcia *et al.* [37] measured that in case of surface corrugations the effective mass is above $1.3m_e$.

Decay of the Image Potential States The image potential states while localized mainly on the vacuum side can penetrate into the substrate with exponentially decaying probability density. This can be investigated by analyzing the local density of states at the different muffin-tin positions. In figure 4.11 the local density of states of the first three image states is plotted for each of the five muffin-tin types. Indeed the decay into the substrate follows the assumed $\psi = exp(-\kappa z)$ behavior. By employing linear regression we get $\kappa_{n=1}$=0.091, $\kappa_{n=2}$=0.088, $\kappa_{n=3}$=0.086 and $\kappa_{n=4}$=0.086 a.u.$^{-1}$. The LDOS of the first image state is higher than the one of the others because it is located closer to the surface than any other state of the Rydberg series. Furthermore it decays also fastest. This can be explained by the CBS of Ag. In figure 2.4 the CBS is shown between the high symmetry points Γ and X. In the (100) direction all $\mathbf{k}$-vectors between them are projected onto $\overline{\Gamma}$. An arrow in the figure marks the position of the band gap at the vacuum level. The higher the Rydberg state the closer the state is located at the band edge. The bandgaps are either connected by loops or the band edge is continued with an infinite lines in the CBS. In this case a loop connects the band edges. The closer the Rydberg state the smaller is the decay. The corresponding values obtained

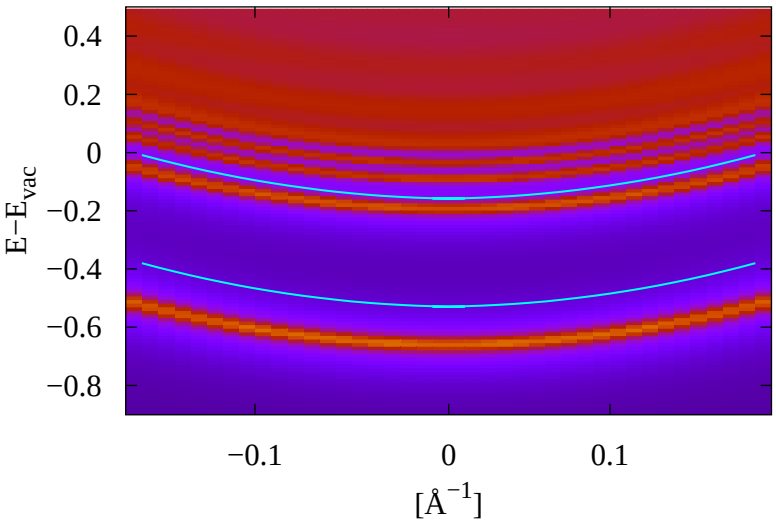

Figure 4.10: Dispersion relation calculated at the unrelaxed Ag(100) surface. Plotted is the **k**-resolved LDOS. The introduced lines represent the experimental values by Schuppler *et al.* [94] with an effective mass of $1m_e$.

from the CBS of the silver substrate are $\kappa_{n=1}^{\mathrm{CBS}}$=0.094, $\kappa_{n=2}^{\mathrm{CBS}}$=0.091, $\kappa_{n=3}^{\mathrm{CBS}}$=0.091, and $\kappa_{n=4}^{\mathrm{CBS}}$=0.090 a.u.$^{-1}$ close to the values calculated from the LDOS. The decay is quite slow, around 6.5 layers are needed before a decay to 1 % is reached.

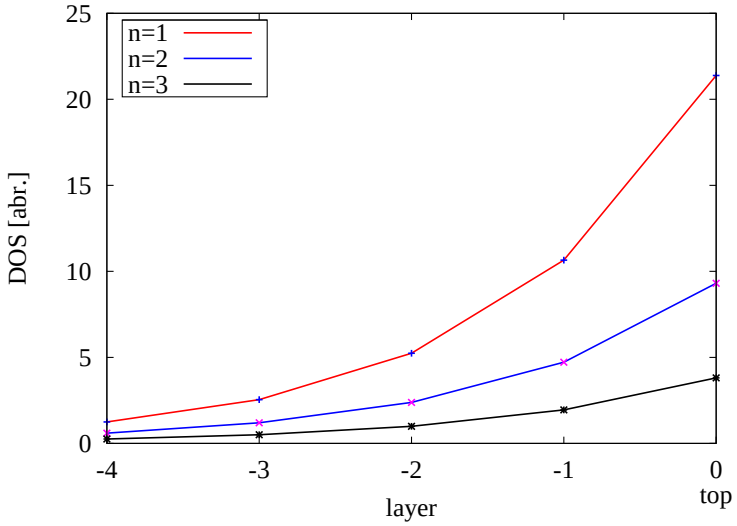

Figure 4.11: The image state decay is investigated in the relaxed Ag(100) surface setup. The LDOS at the topmost layer is highest. The LDOS decays towards the continuum exponentially. The higher the index of Rydberg series the smaller is the LDOS in the substrate because the states are located farther in the vacuum.

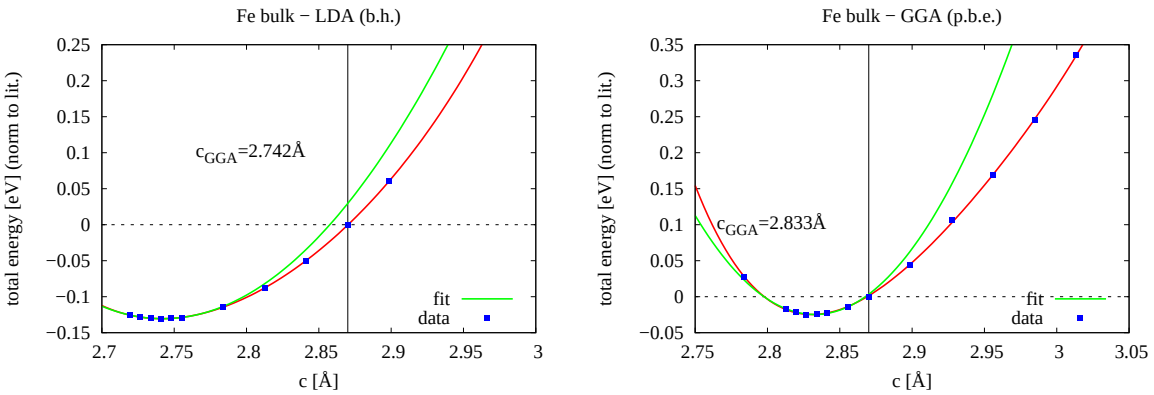

Figure 4.12: Estimated lattice constant of Fe bulk. The total energy of the system is given with respect to the bulk lattice constant. The lowest value is fitted by the green curve in the plot.

4.3.2 Image Potential States of Fe(110)

Before the energies of the image states can be investigated the surface setup has to be explained.

Surface Setup The surface will be relaxed. Therefore the theoretical bulk lattice constant for the chosen exchange correlation potential is estimated like in the case of silver. We obtain 2.833 Å in case of the GGA (PBE) calculation and 2.742 Å for the LDA calculation using the parameters by BH. These results are in very good agreement with 2.83 Å for GGA and 2.74 Å for LDA calculated by Asato *et al.* [6] and with 2.744 Å calculated by Pentcheva [79] with LDA employing also the BH parametrization. The experimental bulk lattice constant is given by 2.87 Å [78]. Again the forces acting on the topmost layers are calculated and the positions are changed until the system with zero forces is found. Two calculations are done with 30 **k**-points in the 2 dimensional irreducible Brillouin zone, a planewave cutoff of 4.0 a.u.$^{-1}$ and the GGA. In the first, the two topmost layer are relaxed and in the second the three topmost layers are relaxed. The results are summarized and compared to published values in table 4.6. The order of magnitude of the relaxation and trend that the layers alter between inwards and outwards relaxation can be reproduced. The influence of the third layer relaxation onto

	this work		Błoński & Kiejna	Stibor *et al.*	Spencer *et al.*	Eder *et al.*
	3layers	2layers	[15]	[14]	[105]	[103]	[32]
Δd_{12}	−0.23	−0.23	−0.1	−0.11	−0.08	−0.13	−0.2
Δd_{23}	+0.61	+0.62	+0.3	+1.16	+0.40	+0.20	-
Δd_{34}	−0.21	-	−0.5	+1.14	−0.25	−0.06	-

Table 4.6: Relaxation of Fe(110) in percent of the unrelaxed interlayer spacing. Stibor *et al.* [105] relaxed four and Błoński *et al.* [15] the seven topmost layers. Our results show a qualitative correct behavior.

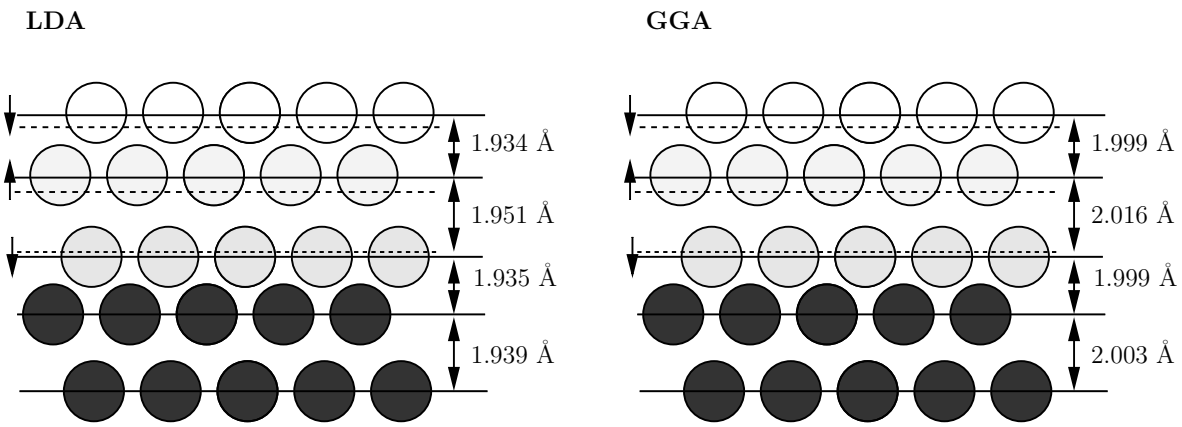

Figure 4.13: Positions of relaxed Fe(110) surface atoms. The three topmost layers are relaxed. Arrows on the left side indicate the relaxation direction.

the two topmost layers is marginal, but nevertheless in the following setups all three topmost layers are relaxed. Thus for the surface setup we get spacings sketched in figure 4.13.

Workfunction The workfunction of a nine layer film and the workfunctions calculated by Green function embedding are summarized in table 4.7. In case of the FLAPW film setup a planewave cutoff of 4.0 a.u.$^{-1}$ and a mesh of 132 **k**-points is taken. The embedding results are obtained by the same setup used in the calculation of the image potential states and will therefore be explained in detail in the next paragraph. In

c [Å]	layer relaxed	method		ϕ [eV]
2.87	-	FLAPW (`Fleur`)	LDA (BH)	5.52
2.742	√			5.72
2.87	-		GGA (PBE)	4.75
2.833	√			4.78
2.87	-	FLAPW+embedding (`GFleur`)	LDA (BH)	5.49
2.742	√			5.70
2.87	-		GGA (PBE)	4.67
2.833	√			4.70

Table 4.7: Calculated workfunctions of Fe(110) for different exchange-correlation potentials, surface setups and methods. The results of the film calculations in the upper and the results of the Green function embedding method in the lower part of the table.

table 4.8 published values of the Fe(110) workfunction are given. Again the Green function method by Inglesfield seems to slightly overestimate the workfunction. The result obtained for the `Fleur` film calculation with the GGA for the exchange-correlation potential is in good agreement with the GGA slab calculation by Błoński *et al.*. We get

		method	published	ϕ [eV]
Fischer *et al.*	[35]	2PPE	1992	5.12 ±0.06
Pirug *et al.*	[83]	X-ray PE (XPS)	1980	5.05
Błoński and Kiejna	[15]	`VASP`, DFT - PAW GGA	2007	4.75 (4.76)
Błoński and Kiejna	[14]	`VASP`, DFT -pseudopotential GGA	2004	4.82 (4.81)
Nekovee *et al.*	[71]	DFT+embedding - LAPW LDA (BH)	1993	5.30
Aldén *et al.*	[3]	TB-LMTO Green func.[97] LDA (BH/C.A.)	1992	5.21
Skriver *et al.*	[98]	TB-LMTO Green func.[97] LDA (C.A.)	1992	5.16

Table 4.8: Published workfunctions of the Fe(110) surface (Relaxed result given in parentheses). Experimental results in the upper and theoretical estimations in the lower part of the table.

the same value of 4.75 eV in case of the unrelaxed system and similar result of 4.78 eV in case of the relaxed system.

Calculate the Image Potential States We calculate the embedding potential from the CBS of bulk iron. The embedding region is cut out of a supercell calculation with 9 layers. The region includes the 4 surface layers and a vacuum region of approximately 14 a.u.. The embedding potential is replacing the atom layer in the middle of the slab. Within the `Fleur` calculations a planewave cutoff, determining the size of the interstitial basis set, is chosen to 3.7 a.u.$^{-1}$. The muffin-tin radius of the Fe atoms is chosen to 2.31 a.u.. The embedding potential is calculated with a planewave cutoff of 3 a.u.$^{-1}$ and napw set to 15 defining the basis set. A self-consistent charge density of the embedding region is calculated with a mesh of 20 **k**-points in the irreducible part of the projected two dimensional Brillouin zone and 15 energies lying on a half cycle in the imaginary plane.
An image plane at $z_{\mathrm{I}} = 3.835$ a.u. (one interlayer spacing) measured from the atomic position of the topmost layer is used in the setup employing the GGA. The mixing region is starting at $z_{\mathrm{m}} = 7.2$ a.u. and is reaching over 8.37 a.u. (50 FFT grid points). In case of the relaxed setup the position of the mixing region is changed slightly to be $z_{\mathrm{m}} = 7.1$ a.u.. In figure 4.15 the LDOS of the relaxed Fe(110) setup is plotted using the GGA. The first image state of the minority spin still shows a little double peak due to the additional state mentioned above. In case of the LDA a different image plane position is chosen. We use the calculated value of the screening position of $z_{\mathrm{I}} = 3.1$ a.u.. The mixing parameter has to be adjusted to $z_{\mathrm{m}} = 12.2$ a.u. in order to obtain the experimental value of the first image state. In general the positions of the image states and the magnetic exchange splitting are stable under reasonable changes in position of the image plane and mixing parameter. Only the energy of the first Rydberg state

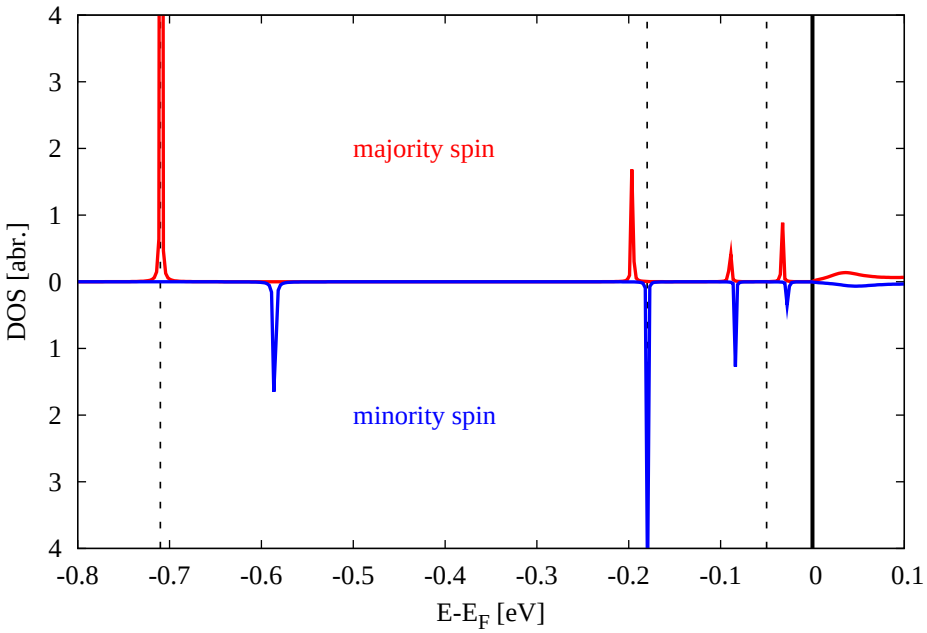

Figure 4.14: Spin resolved LDOS of Fe(110) at $\mathbf{k}_{\parallel} = \overline{\Gamma}$ (unrelaxed GGA). Dotted lines indicate experimental values by Fischer *et al.* [35]. All energies are given relative to the vacuum energy. Delta peaks broadened by a complex energy of $\Im(E) = 10^{-5}$ htr (0.27 meV).

can be influenced by the parameters. The calculated image state energies are in good agreement with the measured values. In table 4.9 our results are summarized. The image state position of the majority spin is given by Nekoveek *et al.* and our work whereas the experimental values are not spin resolved. We are not getting better results by taking care of the relaxation of the topmost layers. As shown before the relaxation is of the order of half a percent of the bulk interlayer spacing and is therefore not influencing the electronic structure of the surface to a large extent.

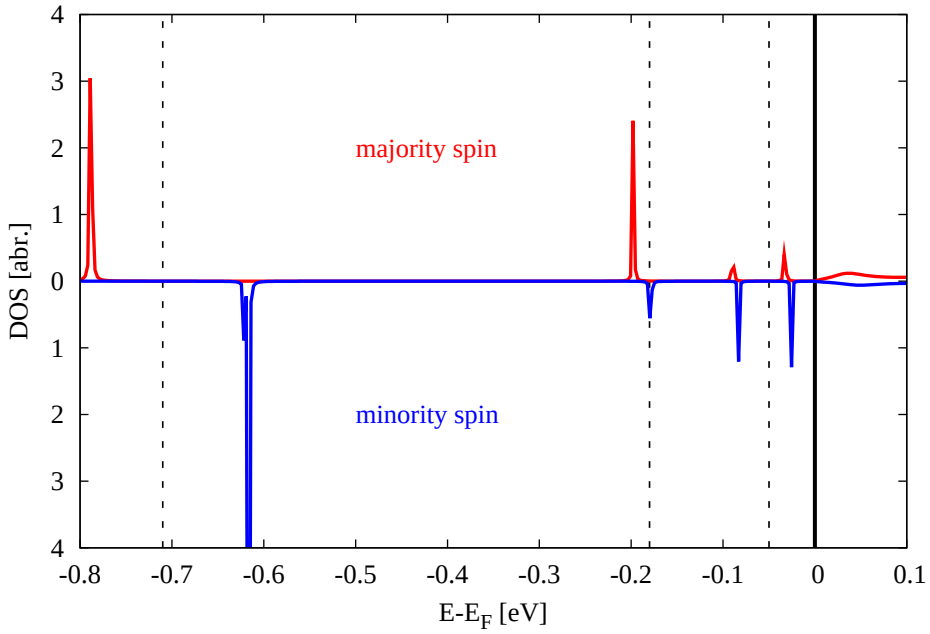

Figure 4.15: LDOS of Fe(110) at $\mathbf{k}_{\parallel} = \overline{\Gamma}$ (relaxed GGA). The artificial broadening is introduced by a complex energy of $\Im(E) = 10^{-5}$ htr (0.27 meV).

		method	year	E_1 [eV]	E_2 [eV]	E_3 [eV]
Fischer *et al.*	[35]	2PPE	1992	-0.73	-0.18	-0.05
Himpsel	[46]	IPE	1991	-0.70 ± 0.15	-	-
Scheidt *et al.*	[93]	IPE	1983	-	-	-
Nekovee *et al.*	[71]	embedding	1993	-0.71	-	-
this work:						
LDA unrelax.			2007	-0.76	-0.22	-0.10
relaxed		embedding	2007	-0.81	-0.22	-0.09
GGA unrelax.			2007	-0.71	-0.20	-0.09
relaxed			2007	-0.79	-0.20	-0.09

Table 4.9: Experimental and theoretical energies of the image potential states of Fe(110). The image plane for both of our LDA/GGA calculations is fixed. The energy of the $n = 1$ image states is moved by the mixing paramenter to be in good agreement with experiment and previous theoretical values.

		method	year	ΔE_1 [meV]	ΔE_2 [meV]	ΔE_3[meV]
Thomann *et al.*	[108]	2PPE	2000	85±20	-	-
Passek *et al.*	[77]	IPE	1995	57± 5	-	-
Fischer *et al.*	[35]	2PPE	1992	< 80	-	-
Nekovee *et al.*	[71]	embedding	1993	55	-	-
Himpsel	[46]	model	1991	27	-	-
Borstel *et al.*	[19]	model	1987	30-200	-	-
this work:						
LDA unrelax.			2007	133	25	10
relaxed		embedding	2007	108	20	5
GGA unrelax.			2007	124	16	7
relaxed			2007	167	18	5

Table 4.10: Splitting of the image potential states of Fe(110). Our splitting is larger than values of previous publications. The splitting is stable under changes of image plane position or applied mixing but it turns out to be influenced by the surface setup.

Magnetic Exchange Splitting The magnetic exchange splitting is investigated and compared with published data (see table 4.10). Obviously our calculations reproduce the splitting in a qualitative way. While the splitting for the Rydberg states higher than $n = 2$ are nearly unchanged by the exchange correlation functional, the layer setup or the mixing parameter chosen, the splitting of the first state is changing. The relaxed setup is giving a bigger splitting of the states if GGA is employed. If the LDA is used in the relaxed setup the splitting becomes smaller. Nekovee *et al.* [71, 72, 73] got a splitting of 55 meV in very good agreement with the experimental result [77] by using also the Green function embedding technique. In contrast to our calculations they used the LDA in a smaller embedding region consisting of only one atom and some vacuum region.

4.4 Image Potential Induced Field States

An electric field is applied to the surface setup and the energies of the image potential states are investigated. Experimentally, the investigation of image potential states via STS is equivalent to our calculation in a first approximation (e.g. neglecting the influence of the tip [75, 26]). In STM experiments the energies of the image states can be measured and in spin-polarized STM experiments even the splitting of the image states can be resolved. The STM spectra are smeared due to the influence of the tip [75] making the evaluation of the spectra difficult. Strictly speaking in this measurements not the image potential states are investigated but image potential induced field states because in all STM measurements an electric field is applied to the surface. We will use the computational method as explained in chapter 2.7. The calculations are done for both systems with setups described in detail in the previous section.
For a first example the Ag(100) surface is calculated. Compareable measurements with STM were done by Pivetta *et al.* [84]. The image potential induced field states show the same qualitative dispersion than the measurement of the image potential states of Ni with applied electric field of Binnig *et al.* [10] in 1985 with non spin-resolved STM.
After silver we investigate the Fe(110) surface. Especially the change in magnetic exchange splitting was traced for different values of applied electric field strength. The results can be compared to measurements done with spin-resolved STM [62]. The transition of field states located in a band gap of the substrate to resonances which are formed at energies with the bulk states present can be observed in both calculations.

4.4.1 Field States of Ag(100)

First the unrelaxed GGA setup explained in 4.3.1 is used for different applied electric fields reaching from 0 to 0.5 eV/Å. For each electric field the local density of states is calculated at $\mathbf{k}_{\parallel} = \overline{\Gamma}$. The properties of the image potential states can be extracted from the broadened delta peaks of the plot. The artificial broadening is introduced by a complex energy of $\Im(E) = 10^{-4}$ htr (2.7 meV). In figure 4.16 the local density of states is given at an applied electric field strength of 0.025 eV/Å. The resulting energies of the image potential states for several different electric fields are plotted in figure 4.17. We find that with increasing electric field the energy of the field states rises. The qualitative behavior of the calculated field states is in accordance to experimental results [10] and reproduces the $E_n \propto \xi^{\frac{2}{3}}$ behavior found for an infinite triangular potential well model given by Eq. (3.45). While most of Fig. 4.20 might have been deduced from a much simpler calculation, a detail in this plot shows the advantage of our semi-infinite *ab initio* calculation. At about 1.9 eV above the vacuum level a bending of the curve can be seen (especially for $n = 2$ and $n = 3$ states). We claim that this is a result of the image potential states reaching the bulk states of the silver surface. Thus the field states become **resonance states**. An investigation of the transition from an image state to an image resonance in the case of zero field with increasing $\mathbf{k}_{\parallel}$ was published by Nekovee and Inglesfield [72]. Here we get a transition due to the increasing of the electric field pushing the image states up in energy and thus out of the band gap.
In figure 4.18 the local density of states of Ag(100) is given for energies far above the vacuum energy without applied electric field. In the region below the vacuum energy

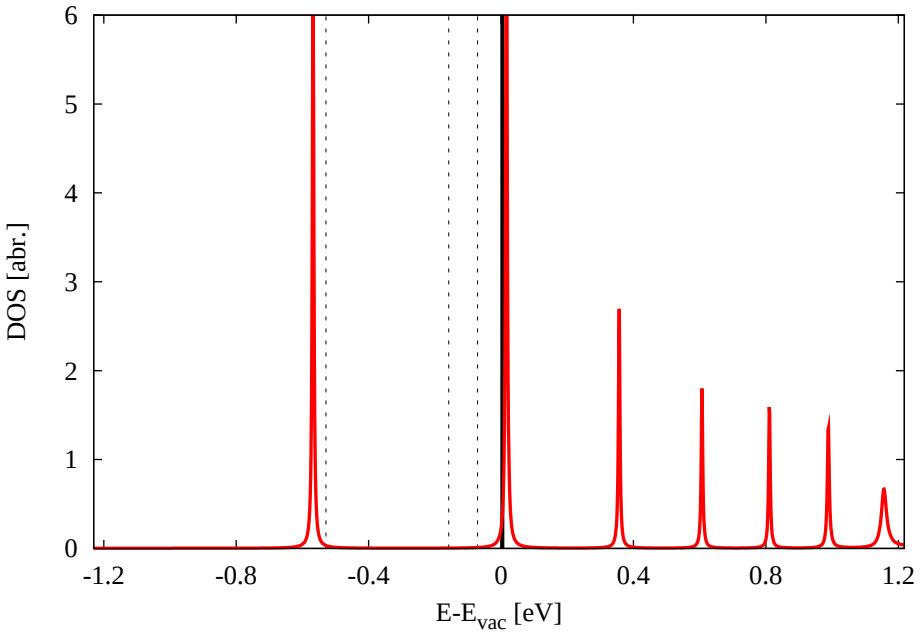

Figure 4.16: LDOS of Ag(100) at $\mathbf{k}_{\parallel} = \overline{\Gamma}$ (unrelaxed GGA) with applied field of 0.025 eV/Å. The states of the Rydberg series are separated because they are pushed towards the substrate by the electric field.

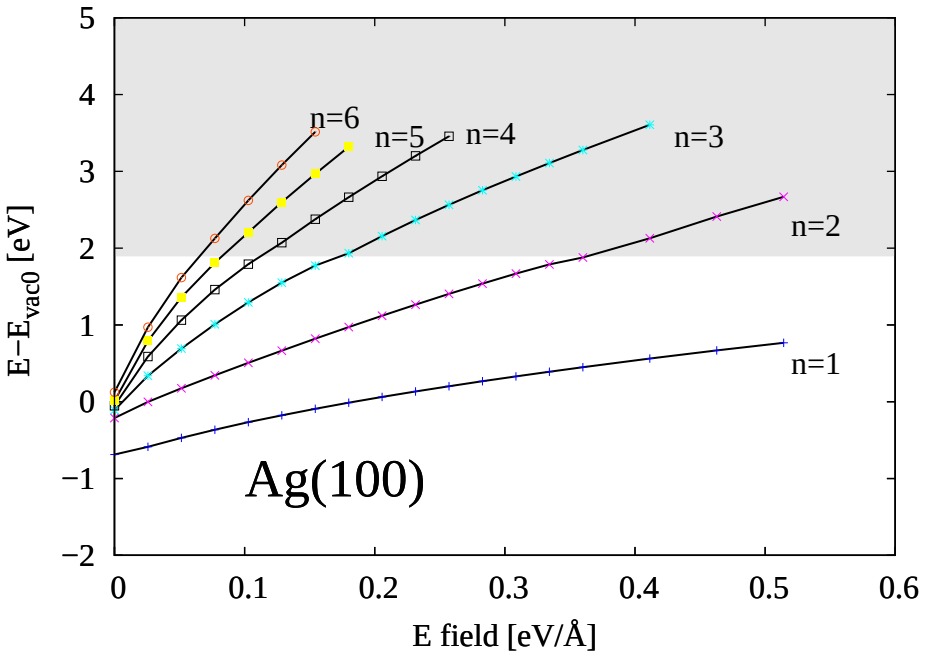

Figure 4.17: Field states of Ag(100) at $\mathbf{k}_{\parallel} = \overline{\Gamma}$ (unrelaxed GGA). At around 1.9 eV a change in slope can be seen. At this point the band edge of the substrate is reached and the field states become resonance states.

four delta peaks are visible at the image potential energies. Then a region of a free electron-like square root behavior follows. At about 1.9 eV the projected bulk band appears. In order to investigate the transition from image states to resonance states

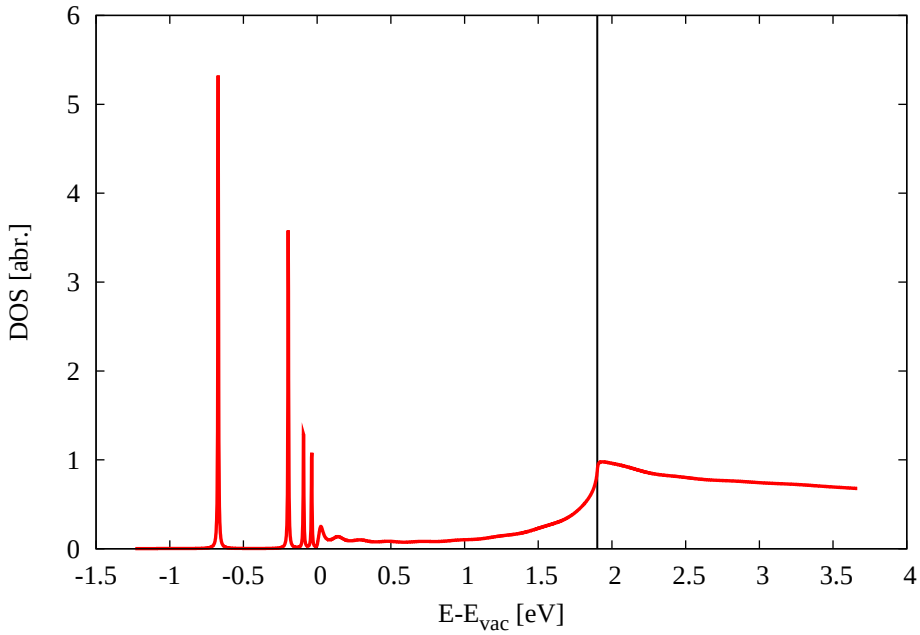

Figure 4.18: LDOS of Ag(100) at $\mathbf{k}_{\parallel} = \overline{\Gamma}$ (unrelaxed GGA). The band edge of the substrate can be found at around 1.9 eV by a rapid increase in local density of states. Its position is marked by a vertical black line.

the two pictures 4.19 are given. The upper LDOS is obtained by calculating the LDOS with an electric field of 0.129 eV/Å. Three delta peaks are present below band edge at 1.9 eV. Above this energy four broadened peaks are visible. The discrete states are interacting with the continuum band of the bulk. Resonance states are resulting. In the lower picture the electric field is increased to 0.231 eV/Å. Only two delta peaks remain because the third one is already pushed into the bulk band. The separation between the states is large compared to the system with lower electric field and the states are moved to higher energies.

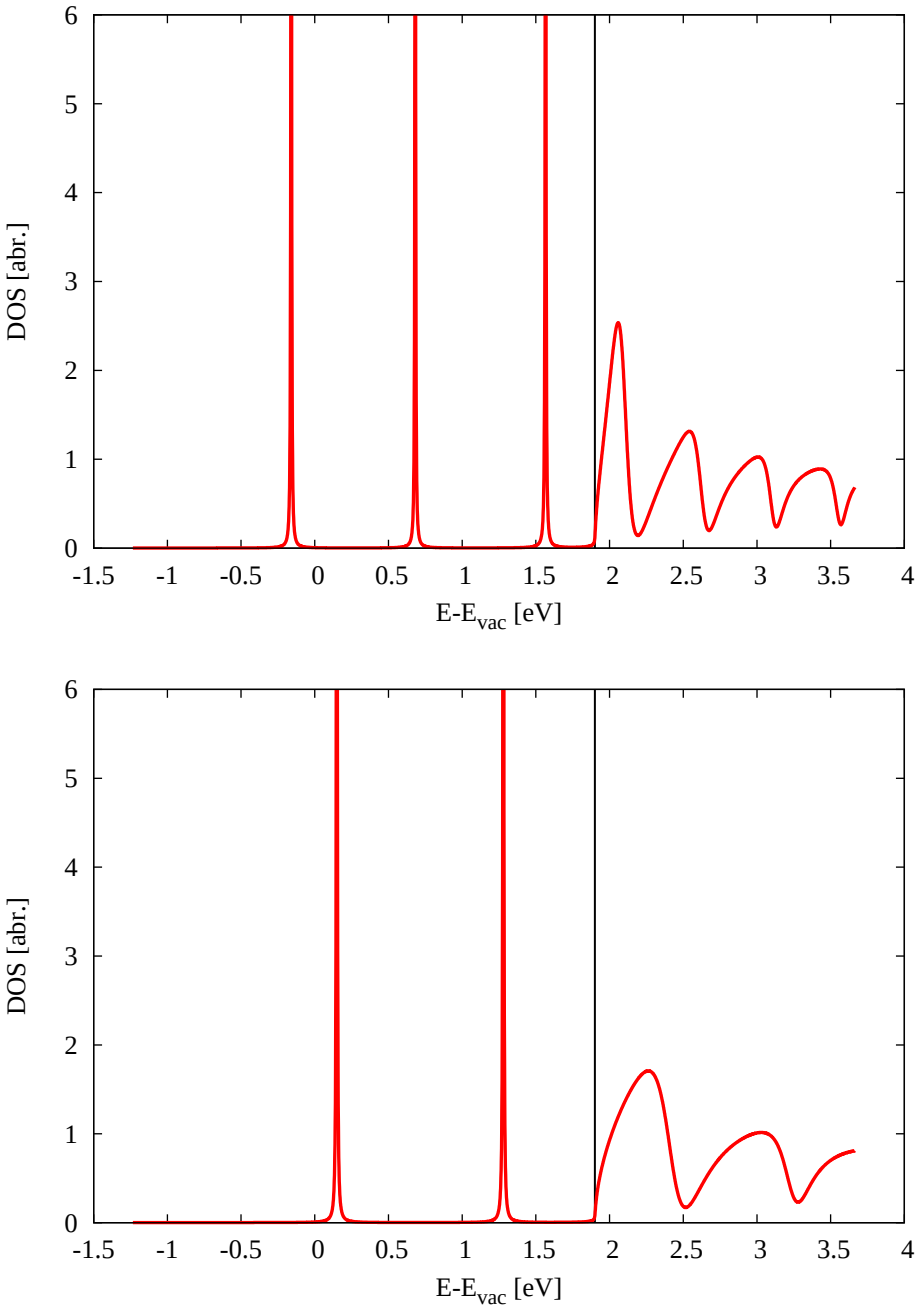

Figure 4.19: Field states of Ag(100) at $\mathbf{k}_{\|} = \overline{\Gamma}$ (unrelaxed GGA) for E-field of 0.129 eV/Å and 0.231 eV/Å. The band edge of the substrate at around 1.9 eV is marked by a vertical black line. The field states become resonance states.

Relaxed Surface The image potential induced field states are calculated for the relaxed surfaces. The surface relaxation of Ag(100) is explained in section 4.3.1. Only small qualitative changes can be seen by comparing figure 4.20 with figure 4.17 presenting the results for the unrelaxed surface. From the LDOS at zero electric field the band edge is determined to be 1.79 eV above the vacuum energy. By investigating the CBS of the silver substrate shown in figure 2.4 the band edge can be found at 1.73 eV. Both values agree nicely if the artificial introduced broadening of the LDOS is considered.

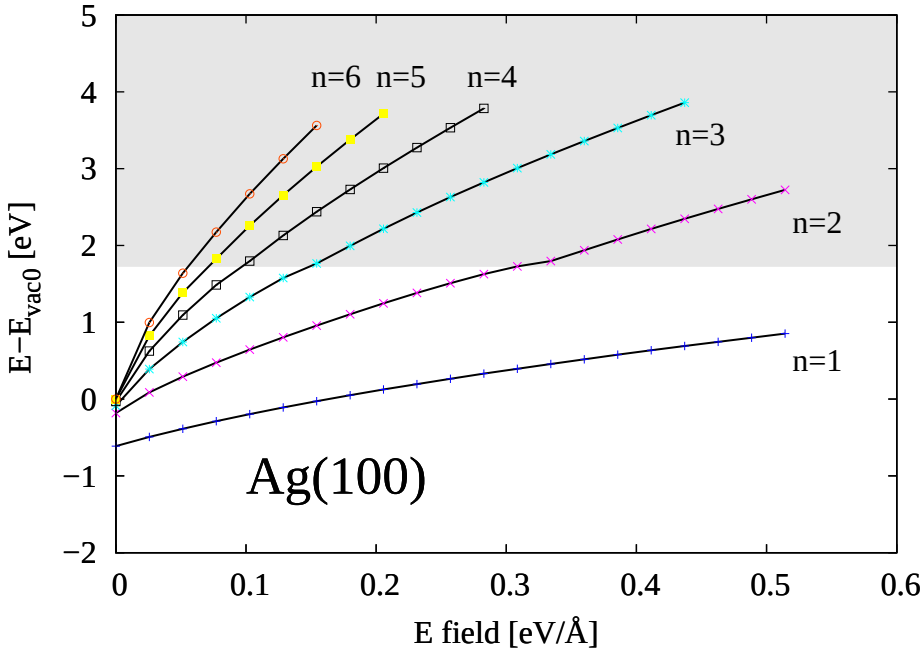

Figure 4.20: Field states of Ag(100) at $\mathbf{k}_{\parallel} = \overline{\Gamma}$ (relaxed GGA). Only marginal changes compared to the unrelaxed setup are visible. The shaded area marks the projected band of the silver substrate at 1.73 eV above the vacuum level. At this energy a transition from the field states to the resonance states takes place and can be observed by the change of slope.

4.4.2 Field States of Fe(110)

The unrelaxed GGA setup from 4.3.2 is calculated for different values of the applied electric field. In the subfigure the change in magnetic exchange splitting is shown. This

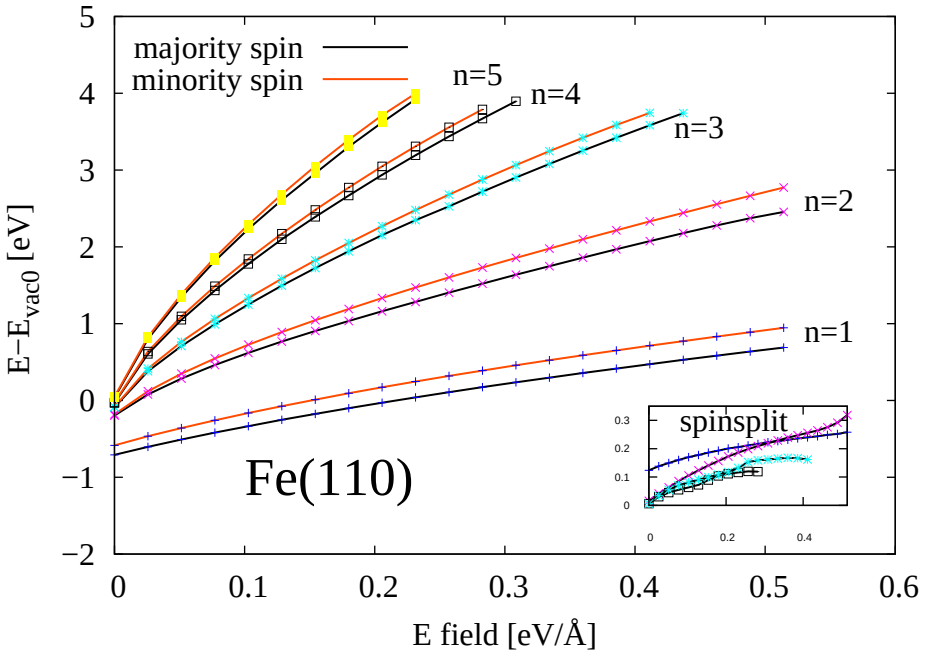

Figure 4.21: Field states of Fe(110) at $\mathbf{k}_{\parallel} = \overline{\Gamma}$ (unrelaxed GGA). The differences of the image state position between minority and majority spin are plotted in the small subfigure.

is the most exciting result of the calculation. In figure 4.22 the result is shown enlarged. Two remarkable features are visible. At a point of about 0.32 eV/Å the splitting of the second image potential state becomes larger than the splitting of the first state. This point is marked 'A' in the picture. This has also been observed experimentally [62]. A second feature is the bending of the curve marked by point 'B' in the plot. This bending can be observed for the image states $n = 2$ to $n = 4$. The same behavior for the first image state is expected above the calculated energy. The interpretation needs another visualization combining both pictures. In figure 4.23 both plots are combined. The vertical lines are marking the beginning of the curvature of the $n = 4$, $n = 3$ and $n = 2$ state from left to right. The horizontal line[3] in the upper part is connecting all three lines and indicates that in all three cases the bending begins at 2.4 eV. We expect this feature to result from the projected band structure of the substrate. A bulk band begins and instead of image states resonance states are resulting [72]. To confirm this the local density of states of the field free system is investigated in figure 4.24. If the energy is above the vacuum energy a free electron like behavior with some oscillations due to the integration over finite regions is observed. The majority state reaches the projected bulk band at ∼2.4 eV, the projected bulk band of the minority spin is ∼3.9 eV above the vacuum energy. By evaluating the CBS of the Fe substrate the band edge is

[3]crossing all others at a right angle

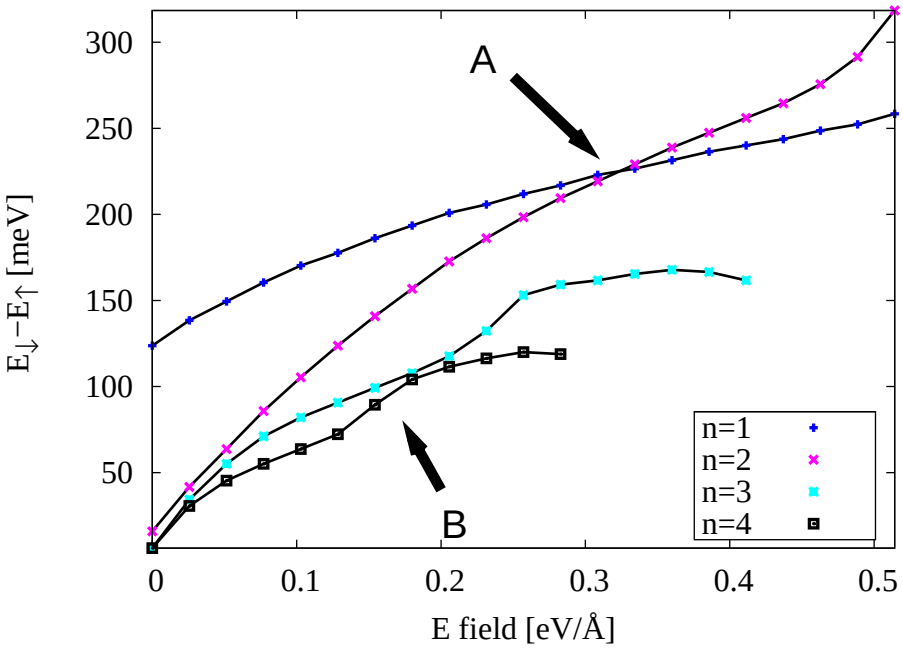

Figure 4.22: Magnetic exchange splitting, Fe(110) at $\mathbf{k}_{\parallel} = \overline{\Gamma}$ (unrelaxed GGA). Two remarkable features are highlighted. At point 'A' the splitting of the second image state becomes larger than the splitting of the first image state. At point 'B' the slope of the curvature changes. Both features can be explained by the projected band structure of the substrate.

determined to 2.46 eV and 3.95 eV. Now the bending can be explained. If the energies of the majority field states reach the band edge of the majority state the states are deflected. This results in a larger spin splitting.

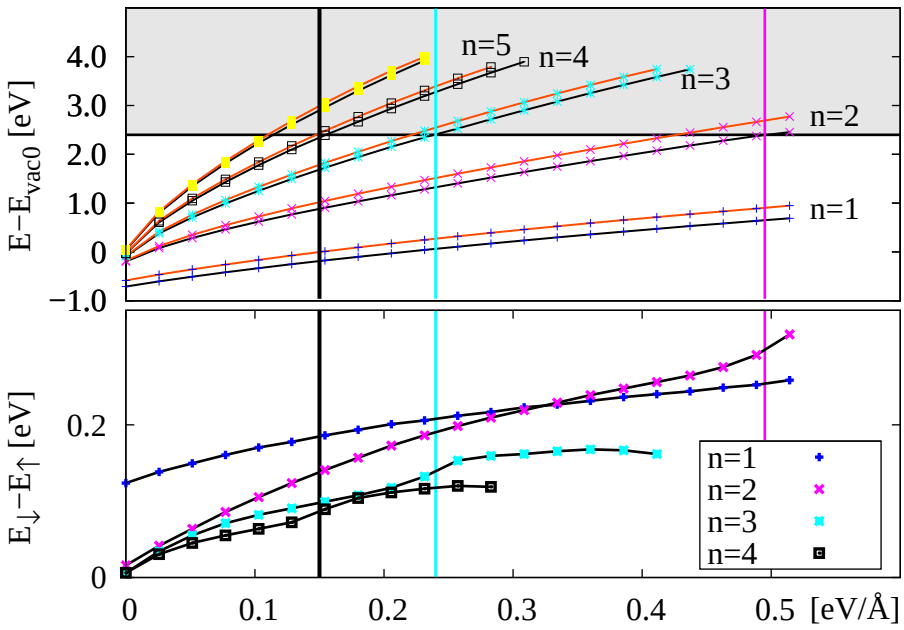

Figure 4.23: In the upper panel the field states of Fe(110) (unrelaxed GGA) at $\mathbf{k}_{\parallel} = \overline{\Gamma}$ are shown. The difference between the majority and the minority state is plotted in the lower panel. The slope of this magnetic exchange splitting is changing. These positions are mapped onto the field states plot by the vertical lines with colors corresponding to the number of the Rydberg state. It can be seen that they all cross there field state curve at the same energy of around 2.4 eV. This is indicated by the black horizontal line. The projected band of the majority spin starts at around 2.4 eV. It explains the features seen in the magnetic exchange splitting plot.

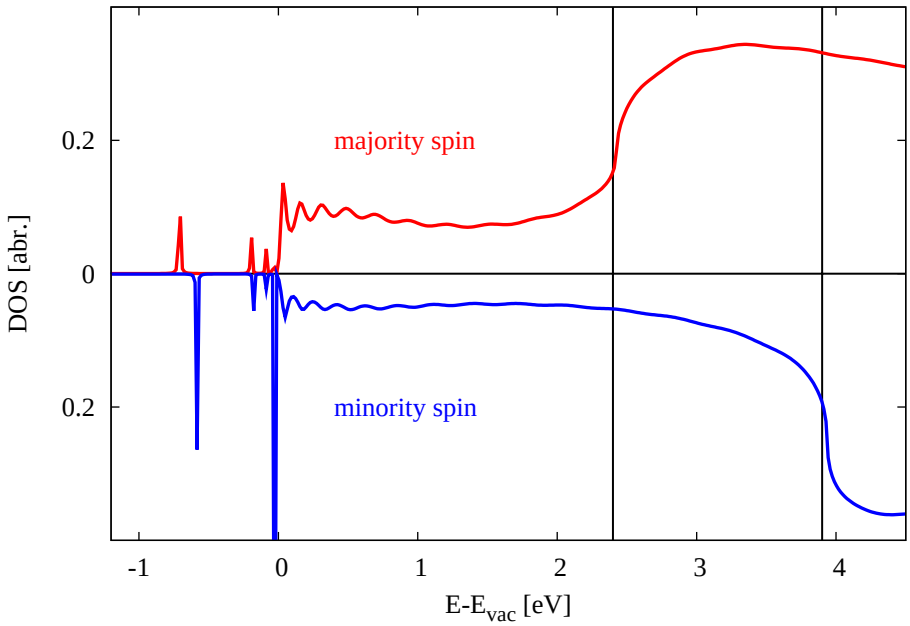

Figure 4.24: LDOS of Fe(110) at $\mathbf{k}_{\parallel} = \overline{\Gamma}$ (unrelaxed GGA). The projected band of the majority spin starts at around 2.4 eV. It explains the features seen in the magnetic exchange splitting plot.

A Appendix

A.1 Numerov Algorithm

The Numerov algorithm can be used for solving a second order differential equation without first derivative but with linearity of the function numerically. An important differential equation fulfilling the requirements is the Schrödinger equation. We will concentrate on the one dimensional case in the following.

$$\left(\frac{d^2\psi(x)}{dx^2} + k^2(x)\right)\psi(x) \;=\; 0 \tag{A.1}$$

The Taylor series for $\psi(x+\Delta_x)$ is

$$\psi(x+\Delta_x) \;=\; \psi(x) + \Delta_x\psi'(x) + \frac{\Delta_x^2}{2}\psi^{(2)}(x) + \frac{\Delta_x^3}{6}\psi^{(3)}(x) + ... \tag{A.2}$$

Adding the series of $\psi(x-\Delta_x)$ and solve for the second derivative we get:

$$\psi^{(2)}(x) \;=\; \frac{\psi(x+\Delta_x)+\psi(x-\Delta_x)-2\psi(x)}{\Delta_x^2} - \frac{\Delta_x^2}{12}\psi^{(4)}(x) + O(\Delta_x^4) \tag{A.3}$$

So far the approach was quite straightforward, but in a next step we act on the Schrödinger equation with $1 + (\Delta_x^2/12)d^2/dx^2$ and get

$$\psi^{(2)}(x) + k^2(x)\psi(x) + \frac{\Delta_x^2}{12}\psi^{(4)}(x) + \frac{\Delta_x^2}{12}\left(k^2(x)\psi(x)\right) \;=\; 0. \tag{A.4}$$

Now substituting (A.4) into (A.3) leads to

$$\psi(x+\Delta_x) + \psi(x-\Delta_x) - 2\psi(x) + h^2k^2(x)\psi(x) + \frac{\Delta_x^4}{12}\frac{d^2}{dx^2}\left(k^2(x)\psi(x)\right) + O(\Delta_x^6) = 0. \tag{A.5}$$

We can express $\frac{d^2}{dx^2}\left(k^2(x)\psi(x)\right)$ by a finite difference formula:

$$\frac{d^2}{dx^2}\left(k^2(x)\psi(x)\right) \;\approx\; \frac{k^2(x+\Delta_x)\psi(x+\Delta_x) + k^2(x-\Delta_x)\psi(x-\Delta_x) - 2k^2(x)\psi(x)}{\Delta_x^2} \tag{A.6}$$

Thus the Numerov algorithm for one step is obtained after rearranging from (A.4) to:

$$\psi(x+\Delta_x) = \frac{2\left(1-\frac{5}{12}\Delta_x^2k^2(x)\right)\psi(x) - \left(1+\frac{1}{12}\Delta_x^2k^2(x-\Delta_x)\right)\psi(x-\Delta_x)}{1+\frac{1}{12}\Delta_x^2k^2(x+\Delta_x)} + O(\Delta_x^6) \tag{A.7}$$

Acknowledgment

First of all I would like to thank Prof. Dr. Stefan Blügel for giving me the possibility to make my master thesis in his group at the IFF in the research center Jülich and to present my results at the DPG meeting in Regensburg. He was always helpful and I felt welcome in his group all the time. In special I want to thank my supervisor Dr. Daniel Wortmann who never gave up explaining me his embedding code and the mysteries of solid state physics.
I would like to thank Dr. Gustav Bihlmayer helping me whenever I struggled with `Fleur` and Dr. Robert Jones for the information regarding the 'triple J' model and the history of image potential states. Dr. Andre Kubetzka for the invitation to give a talk at the university Hamburg, the time he spent showing and explaining me almost all the STMs setups they have and the motivation I got from getting to know the experimental details of STS measurements of image potential states. Dr. Yuriy Mokrousov for his constant interest in my work and the resulting motivation. Dipl. Phys. Michael Fleck and M. S. Ming-Hao Liu for the good working atmosphere in our office.
Furthermore I would like to thank Dipl. Phys. Andreas Gierlich for the time he spend reading through my thesis and making a lot of useful comments regarding both my English and the content of the thesis. Useful comments making this thesis more read- and understandable came also from Dipl. Phys. Ali Al-Zubi.
I am indebted to Ute Winkler who always knew how to scope with the bureaucratic problems which by law of nature always arise unforeseeable.
Also I would like to mention other members of the group who I was pleased to get to know during my stay: Arno Schindlmayr, Eva Pavarini, Erik Koch, Christoph Friedrich, Markus Heide, Marjana Lezaic, Laurent Chaput, Frank Freimuth, Phivos Mavropoulos, Paul Baumeister, Markus Betzinger, Andreas Dolfen, Swantje Heers, Manfred Niesert, Simon Woodford and Ersoy Sasioglu.
At the end I would like to give proper recognition to all the people who were always lenient toward me when I was complaining about stepfunctions or ferromagnetic LDA calculations once to often.

Of course without the support and understanding from my family and friends this work would not have been possible.

Bibliography

[1] D. L. Abraham and H. Hopster.
Spin-polarized electron-energy-loss spectroscopy on Ni.
Phys. Rev. Lett., 62(10):1157–1160, Mar 1989.

[2] G. C. Aers and J. E. Inglesfield.
Electric field and Ag(001) surface electronic structure.
Surf. Sci., 217(1-2):367–383, July 1989.

[3] M. Aldén, S. Mirbt, H. L. Skriver, N. M. Rosengaard, and B. Johansson.
Surface magnetism in iron, cobalt, and nickel.
Phys. Rev. B, 46(10):6303–6312, Sep 1992.

[4] W. Altmann, V. Dose, and A. Goldmann.
Momentum-resolved bremsstrahlung isochromat spectroscopy of silver surfaces.
Z. Phys. B, 65(2):171–80, 1986.

[5] O. K. Andersen.
Linear methods in band theory.
Phys. Rev. B, 12(8):3060–3083, Oct 1975.

[6] M. Asato, A. Settels, T. Hoshino, T. Asada, S. Blügel, R. Zeller, and P. H. Dederichs.
Full-potential KKR calculations for metals and semiconductors.
Phys. Rev. B, 60(8):5202–5210, Aug 1999.

[7] A. Baratoff.
Theory of scanning tunneling microscopy - methods and approximations.
Physica B, 127(143), 1984.

[8] J. Bardeen.
Tunnelling from a many-particle point of view.
Phys. Rev. Lett., 6(2):57–59, Jan 1961.

[9] U von Barth and L Hedin.
A local exchange-correlation potential for the spin polarized case. i.
J. Phys. C, 5(13):1629–1642, 1972.

[10] G. Binnig, K. H. Frank, H. Fuchs, N. Garcia, B. Reihl, H. Rohrer, F. Salvan, and A. R. Williams.
Tunneling spectroscopy and inverse photoemission: Image and field states.
Phys. Rev. Lett., 55(9):991–994, Aug 1985.

[11] G. Binnig and H. Rohrer.
Scanning tunneling microscopy-from birth to adolescence.
Rev. Mod. Phys., 59(3):615–625, Jul 1987.

[12] G. Binnig, H. Rohrer, Ch. Gerber, and E. Weibel.
Surface studies by scanning tunneling microscopy.
Phys. Rev. Lett., 49(1):57–61, Jul 1982.

[13] G. Binnig, H. Rohrer, Ch. Gerber, and E. Weibel.
Tunneling through a controllable vacuum gap.
Applied Physics Letters, 40(2):178–180, Jan 1982.

[14] P. Błoński and A. Kiejna.
Calculation of surface properties of bcc iron.
Vacuum, 74(2):179–183, May 2004.

[15] P. Błoński and A. Kiejna.
Structural electronic, and magnetic properties of bcc iron surfaces.
Surf. Sci., 601(1):123–133, Jan. 2007.

[16] S. Blügel, G. Gompper, and E. Koch.
Computational condensed matter physics. Lecture manuscripts of the 37th spring school of the institute of solid state research.
Forschungszentrum Jülich, March 2006.

[17] M. Bode.
Spin-polarized scanning tunnelling microscopy.
Reports on Progress in Physics, 66(4):523–582, 2003.

[18] K.P. Bohnen, Th. Rodach, and K.-M. Ho.
The Structure of Surfaces III.
Springer, New York, 1991.

[19] G. Borstel and G. Thorner.
Inverse photoemission from solids: Theoretical aspects and applications.
Surf. Sci. Rep., 8(1):1–41, 1987.

[20] K. Burke, J. Werschnik, and E. K. U. Gross.
Time-dependent density functional theory: Past, present, and future.
J. Chem. Phys., 123:062206, Aug. 2005.

[21] G. Butti, S. Caravati, G. P. Brivio, M. I. Trioni, and H. Ishida.
Image potential states and electronic structure of Na/Cu(111).
Phys. Rev. B, 72:125402, 2005.

[22] R. Car and M. Parrinello.
Unified approach for molecular dynamics and density-functional theory.
Phys. Rev. Lett., 55(22):2471–2474, Nov 1985.

[23] M. Chelvayohan and C. H. B. Mee.
Work function measurements on (110), (100) and (111) surfaces of silver.
J. Phys. C, 15(10):2305–2312, 1982.

[24] E. V. Chulkova, V. M. Silkina, and P. M. Echenique.
Image potential states on lithium, copper and silver surfaces.
Surf. Sci., 391(1-3):L1217–L1223, 1997.

[25] Sean Clarke, Gustav Bihlmayer, and Stefan Blügel.

Chemical effects in rare gas adsorption: FLAPW calculations for Ag(001)c(2x2)-Xe.
Phys. Rev. B, 63(8):085416, Feb 2001.

[26] S. Crampin.
Lifetimes of stark-shifted image states.
Phys. Rev. Lett., 95(4):046801, 2005.

[27] A. Dolfen.
Massively parallel exact diagonalization of strongly correlated systems.
Master's thesis, Forschungszentrum Jülich, 2006.

[28] M. Donath, C. Math, M. Pickel, A.B. Schmidt, and M. Weinelt.
Realization of a spin-polarized two dimensional electron gas via image-potential-induced surface states.
Surf. Sci. in press, 2007.

[29] A. W. Dweydari and C. H. B. Mee.
Work function measurements on (100) and (110) surfaces of silver.
Physica Status Solidi (a), 27(1):223 – 230, 1975.

[30] P. M. Echenique and J. B. Pendry.
The existence and detection of Rydberg states at surfaces.
J. Phys. C, 11(10):2065–2075, 1978.

[31] E. N. Economou.
Green's functions in quantum physics.
Springer-Verlag, 1983.

[32] Michael Eder, Kiyoyuki Terakura, and Jürgen Hafner.
Initial stages of oxidation of (100) and (110) surfaces of iron caused by water.
Phys. Rev. B, 64(11):115426, Aug 2001.

[33] A. G. Eguiluz, M. Heinrichsmeier, A. Fleszar, and W. Hanke.
First-principles evaluation of the surface barrier for a Kohn-Sham electron at a metal surface.
Phys. Rev. Lett., 68(9):1359–1362, Mar 1992.

[34] Th. Fauster and W. Steinmann.
Photonic Probes of Surfaces, chapter 8. Two-photon photoemission spectroscopy of image states, pages 347–411.
Elsevier, Amsterdam, 1995.

[35] R. Fischer, N. Fischer, S. Schuppler, Th. Fauster, and F. J. Himpsel.
Image states on Co(0001) and Fe(110) probed by two-photon photoemission.
Phys. Rev. B, 46(15):9691–9693, Oct 1992.

[36] J. C. Fuggle and J. E. Inglesfield.
Unoccupied electronic states.
Topics in Applied Physics, Springer-Verlag, 69, 1992.

[37] N. Garcia, B. Reihl, K. H. Frank, and A. R. Williams.
Image states: Binding energies, effective masses, and surface corrugation.
Phys. Rev. Lett., 54(6):591–594, Feb 1985.

[38] I. Giaever.
Electron tunneling and superconductivity.
Rev. Mod. Phys., 46(2):245–250, Apr 1974.

[39] K. Giesen, F. Hage, F. J. Himpsel, H. J. Riess, and W. Steinmann.
Binding energy of image-potential states: Dependence on crystal structure and material.
Phys. Rev. B, 35(3):971–974, Jan 1987.

[40] A. Goldmann, V. Dose, and G. Borstel.
Empty electronic states at the (100), (110), and (111) surfaces of nickel, copper, and silver.
Phys. Rev. B, 32(4):1971–1980, Aug 1985.

[41] E.T. Goodwin.
Electronic states at the surfaces of crystals. I. the approximation of nearly free electrons.
Proc. Cambridge Phil. Soc., 35:205–220, 1939.

[42] V. Heine.
On the general theory of surface states and scattering of electrons in solids.
Proc. Phys. Soc., 81:300–310, 1963.

[43] V. Heine.
Some theory about surface states.
Surf. Sci., 2:1–7, 1964.

[44] S. Heinze.
First-Principles Theory of Scanning Tunneling Microscopy Applied to Transition-Metal Surfaces.
PhD thesis, Universität Hamburg, 2000.

[45] S. Heinze, M. Bode, A. Kubetzka, O. Pietzsch, X. Nie, S. Blugel, and R. Wiesendanger.
Real-space imaging of two-dimensional antiferromagnetism on the atomic scale.
Science, 288(5472):1805–1808, 2000.

[46] F. J. Himpsel.
Image states at ferromagnetic surfaces: Fe(110), (100), (111) and Co(0001).
Phys. Rev. B, 43(16):13394–13400, Jun 1991.

[47] P. Hohenberg and W. Kohn.
Inhomogeneous electron gas.
Phys. Rev., 136(3B):B864–B871, Nov 1964.

[48] J. E. Inglesfield and G. A. Benesh.
Surface electronic structure: Embedded self-consistent calculations.
Phys. Rev. B, 37:6682–6700, 1988.

[49] J. E. Inglesfield and E. W. Plummer.
The physics of potoemission.
studies in surface science and catalysis, angle-resolved potoemission, Chapter 2, editor S.D. Kevan elsevier, 74, 1992.

[50] J.E. Inglesfield.
A method of embedding.
J. Phys. C, 14:3795, 1981.

[51] H. Ishida.
Surface-embedded green function calculation using non-local pseudopotentials.
Surf. Sci., 388(1-3):71–83, October 1997.

[52] H. Ishida.
Surface-embedded Green-function method: A formulation using a linearized-augmented-plane-wave basis set.
Phys. Rev. B, 63(16):165409, Apr 2001.

[53] H. Ishida and A. Liebsch.
Static and quasistatic response of Ag surfaces to a uniform electric field.
Phys. Rev. B, 66:155413, 2002.

[54] Andrew J. Jason.
Field-induced resonance states at a surface.
Phys. Rev., 156(2):266–285, Apr 1967.

[55] R. O. Jones, P. J. Jennings, and O. Jepsen.
Surface barrier in metals: A new model with application to W(001).
Phys. Rev. B, 29(12):6474–6480, Jun 1984.

[56] J. Kohanoff and N. Gidopoulos.
Density functional theory: basics, new trends and applications, ed. s. wilson.
Handbook of Molecular Physics and Quantum Chemistry (Wiley, Chichester, 2003), Volume 2, Part 5, Chapter 26:532–568, 2003.

[57] W. Kohn.
Analytic properties of bloch waves and wannier functions.
Phys. Rev., 115(4):809–821, Aug 1959.

[58] W. Kohn.
Density functional theory: Fundamentals and applications, reprinted from highlights of condensed- matter theory.
Soc. Italiana di Fisica, LXXXIX, 1985.

[59] W. Kohn.
Nobel lecture: Electronic structure of matter-wave functions and density functionals.
Rev. Mod. Phys., 71(5):1253–1266, Oct 1999.

[60] W. Kohn and L. J. Sham.
Self-consistent equations including exchange and correlation effects.
Phys. Rev., 140(4A):A1133–A1138, Nov 1965.

[61] R. de L. Kronig and W. G. Penney.
Quantum mechanics of electrons in crystal lattices.
Proceedings of the Royal Society of London. Series A, 130(814):499–513, Feb. 1931.

[62] A. Kubetzka, M. Bode, and R. Wiesendanger.
Appl. Phys. Lett., to be published, 2007.

[63] P. Kurz.
Non-Collinear Magnetism at Surfaces and in Ultrathin Films.
PhD thesis, Forschungszentrum Jülich, 2000.

[64] N. D. Lang and W. Kohn.
Theory of metal surfaces: Induced surface charge and image potential.
Phys. Rev. B, 7:3541 – 3550, 1973.

[65] M. Levy.
Universal variational functionals of electron densities, first-order density matrices, and natural spin-orbitals and solution of the v-representability problem.
PNAS, 76(12):6062–6065, 1979.

[66] E Louis, F Flores, and P M Echenique.
Theoretical aspects of scanning tunneling microscopy.
Phys. Scr., 37(3):359–369, 1988.

[67] I. Merrick, J. E. Inglesfield, and G. A. Attard.
Local work function and induced screening effects at stepped Pd surfaces.
Phys. Rev. B, 71:085407, 2005.

[68] M. Methfessel, D. Hennig, and M. Scheffler.
Trends of the surface relaxations, surface energies, and work functions of the 4d transition metals.
Phys. Rev. B, 46(8):4816–4829, Aug 1992.

[69] G.E. Moore.
Cramming more components onto integrated circuits.
Electronics, 38:114, 1965.

[70] M. Nekovee.
Image Potential States and Dielectric Response at Metal Surfaces.
PhD thesis, University of Nijmegen, 1995.

[71] M. Nekovee, S. Crampin, and J. E. Inglesfield.
Magnetic splitting of image states at Fe(110).
Phys. Rev. Lett., 70(20):3099–3102, May 1993.

[72] M. Nekovee and J. E. Inglesfield.
Image-induced surface states and resonances at Fe(110).
Surf. Rev. and Lett., 1(4):415–420, 1994.

[73] M. Nekovee and J.E. Inglesfield.
Theory of image states at magnetic surfaces.
Prog. in Surf. Sci., 50:149–158(10), September 1995.

[74] T. Ohwaki, H. Ishida, and A. Liebsch.
First-principles calculation of field emission from metal surfaces.
Phys. Rev. B, 68(15):155422, Oct 2003.

[75] J. I. Pascual, C. Corriol, G. Ceballos, I. Aldazabal, H.-P. Rust, K. Horn, J. M. Pitarke, P. M. Echenique, and A. Arnau.
Role of the electric field in surface electron dynamics above the vacuum level.
Phys. Rev. B, 75(16):165326, 2007.

[76] F. Passek and M. Donath.
Spin-split image-potential-induced surface state on Ni(111).
Phys. Rev. Lett., 69(7):1101–1104, Aug 1992.

[77] F. Passek, M. Donath, K. Ertl, and V. Dose.
Longer living majority than minority image state at Fe(110).
Phys. Rev. Lett., 75(14):2746–2749, Oct 1995.

[78] W. B Pearson.
A handbook of lattice spacings and structures of metals and alloys.
London : Pergamon Pr., 1958.

[79] R. Pentcheva.
Ab initio calculations investigating the connection between magnetism and structure of ultrathin films.
Master's thesis, Forschungszentrum Jülich, 1997.

[80] J. P. Perdew, K. Burke, and M. Ernzerhof.
Generalized gradient approximation made simple.
Phys. Rev. Lett., 77(18):3865–3868, Oct 1996.

[81] John P. Perdew and Yue Wang.
Accurate and simple analytic representation of the electron-gas correlation energy.
Phys. Rev. B, 45(23):13244–13249, Jun 1992.

[82] M. Pickel, A.B. Schmidt, M. Donath, and M. Weinelt.
A two-photon photoemission study of spin-dependent electron dynamics.
Surf. Sci., 600(18):4176–4179, September 2006.

[83] G. Pirug, G. Broden, and H. P. Bonzel.
Coadsorption of potassium and oxygen on Fe(110).
Surf. Sci., 94(2-3):323–338, Apr 1980.

[84] M. Pivetta, F. Patthey, M. Stengel, A. Baldereschi, and W. D. Schneider.
Local work function moir[e-acute] pattern on ultrathin ionic films: NaCl on Ag(100).
Phys. Rev. B, 72(11):115404, 2005.

[85] H.-C. Ploigt and W.D. Schneider.
to be published, 2007.

[86] J. A. Pople.
Nobel lecture: Quantum chemical models.
Rev. Mod. Phys., 71(5):1267–1274, Oct 1999.

[87] B. Reihl, K. H. Frank, and R. R. Schlittler.
Image-potential and intrinsic surface states on Ag(100).
Phys. Rev. B, 30(12):7328–7331, Dec 1984.

[88] B. Reihl and J. M. Nicholls.
Image-potential surface states on Ag(100): A reinvestigation.
Z. Phys. B, 67:221–224, 1987.

[89] F. Reinert and S. Hüfner.
Photoemission spectroscopyfrom early days to recent applications.

New J. Phys., 7(97), 2005.

[90] F. Reinert, G. Nicolay, S. Schmidt, D. Ehm, and S. Hüfner.
Direct measurements of the l-gap surface states on the (111) face of noble metals by photoelectron spectroscopy.
Phys. Rev. B, 63(11):115415, Mar 2001.

[91] G. Rickayzen.
Green's functions and condensed matter.
Academic Press Inc.,U.S., Oct 1980.

[92] J. Rundgren and G. Malmstrom.
Transmission and reflection of low-energy electrons at the surface barrier of a metal.
J. Phys. C, 10(23):4671–4687, 1977.

[93] H. Scheidt, M. Glöbl, V. Dose, and J. Kirschner.
Exchange-split empty energy bands of Fe(110).
Phys. Rev. Lett., 51(18):1688–1691, Oct 1983.

[94] S. Schuppler, N. Fischer, Th. Fauster, and W. Steinmann.
Bichromatic two-photon photoemission spectroscopy of image potential states on Ag(100).
Appl. Phys. A, 51(4):322, October 1990.

[95] W. Shockley.
On the surface states associated with a periodic potential.
Phys. Rev., 56(4):317–323, Aug 1939.

[96] D. J. Singh and L. Nordstrom.
Planewaves, pseudopotentials, and the LAPW method.
Springer; 2 edition, Nov. 2005.

[97] H. L. Skriver and N. M. Rosengaard.
Self-consistent Green's-function technique for surfaces and interfaces.
Phys. Rev. B, 43(12):9538–9549, Apr 1991.

[98] H. L. Skriver and N. M. Rosengaard.
Surface energy and work function of elemental metals.
Phys. Rev. B, 46(11):7157–7168, Sep 1992.

[99] J. C. Slater.
Wave functions in a periodic potential.
Phys. Rev., 51(10):846–851, May 1937.

[100] J. C. Slonczewski.
Conductance and exchange coupling of two ferromagnets separated by a tunneling barrier.
Phys. Rev. B, 39(10):6995–7002, Apr 1989.

[101] J. R. Smith, F. J. Arlinghaus, and J. G. Gay.
Electronic structure of silver (100).
Phys. Rev. B, 22(10):4757–4763, Nov 1980.

[102] N. V. Smith.
Inverse photoemission.
Rep. Prog. Phys., 51(9):1227–1294, 1988.

[103] M. J. S. Spencer, A. Hung, I. K. Snook, and I. Yarovsky.
Density functional theory study of the relaxation and energy of iron surfaces.
Surf. Sci., 513(2):389–398, July 2002.

[104] K. Starke, K. Ertl, and V. Dose.
Exchange splitting of sp-like surface states on Ni(001).
Phys. Rev. B, 45(11):6154–6162, Mar 1992.

[105] A. Stibor, G. Kresse, A. Eichler, and J. Hafner.
Density functional study of the adsorption of CO on Fe(110).
Surf. Sci., 507-510:99–102, Jun 2002.

[106] Ig. Tamm.
A possible kind of electron binding on crystal surfaces.
Phys. Zs. d. Sowjetunion, 76(1):733–746, 1932.

[107] J. Tersoff and D. R. Hamann.
Theory and application for the scanning tunneling microscope.
Phys. Rev. Lett., 50(25):1998–2001, Jun 1983.

[108] U. Thomann, Ch. Reuß, Th. Fauster, F. Passek, and M. Donath.
Image-potential states on bcc (110) surfaces of iron and tungsten.
Phys. Rev. B, 61(23):16163–16167, Jun 2000.

[109] W. A. Thompson and S. F. Hanrahan.
Thermal drive apparatus for direct vacuum tunneling experiments.
Review of Scientific Instruments, 47(10):1303–1304, Oct 1976.

[110] K Urban, C.M. Schneider, Brückel T., S. Blügel, K. Tillmann, W. Schweika, Lentzen M, and L. Baumgarten.
Probing the nanoworld, lecture manuscripts of the 38th spring school of the institute of solid state research.
Forschungszentrum Jülich, March 2007.

[111] O. Vallee and M. Soares.
Airy Functions and Applications to Physics.
Imperial College Press, 2004.

[112] M. Weinert.
Solution of Poisson's equation: Beyond Ewald-type methods.
J.Math.Phys., 22(11):2433–2439.

[113] M. Weinert, S. L. Hulbert, and P. D. Johnson.
Image planes and surface states.
Phys. Rev. Lett., 55:2055 – 2058, 1985.

[114] E. Wimmer, H. Krakauer, M. Weinert, and A. J. Freeman.
Full-potential self-consistent linearized-augmented-plane-wave method for calculating the electronic structure of molecules and surfaces: O_2 molecule.
Phys. Rev. B, 24(2):864–875, Jul 1981.

[115] M. Wolf, E. Knoesel, and T. Hertel.
Ultrafast dynamics of electrons in image-potential states on clean and Xe-covered Cu(111).
Phys. Rev. B, 54(8):R5295–R5298, Aug 1996.

[116] D. Wortmann.
An Embedding Green Function Approach for Electron Transport through Interfaces.
PhD thesis, Forschungszentrum Jülich, 2003.

[117] D. Wortmann, H. Ishida, and S. Blügel.
Ab initio Green-function formulation of the transfer matrix: Application to complex band structures.
Phys. Rev. B, 65(16):165103, Mar 2002.

[118] D. Wortmann, H. Ishida, and S. Blügel.
Embedded green-function approach to the ballistic electron transport through an interface.
Phys. Rev. B, 66(7):075113, Aug 2002.

[119] www.flapw.de.

[120] D. Yoder-Short.
On a small error in srm640, srm640a and srm640b lattice parameters.
Journal of Applied Crystallography, 26(2):272–276, Apr 1993.